UNIVERSITÉ FERHAT ABBAS - SETIF1

FACULTÉ DE TECHNOLOGIE

THÈSE

Présentée au Département de génie des procédés

En vue de l'obtention du diplôme de

DOCTORAT

Domaine : Sciences et Technologie

Filière : Génie des procédés   **Option : Génie Chimique**

Par

ZEMOURI Abd Errahmane

THÈME

Synthèse verte et caractérisation physico-chimique de nanomatériaux magnétiques. Applications en traitement environnemental pour l'adsorption de polluants organiques en milieu aqueux

Soutenu le 06 / 03 / 2025 devant le Jury:

BENANIBA Mohamed Tahar	**Professeur**	**Univ. Ferhat Abbas Sétif 1**	**Président**
BENTOUHAMI Embarek	**Professeur**	**Univ. Ferhat Abbas Sétif 1**	**Directeur de thèse**
BOUTAHALA Mokhtar	**Professeur**	**Univ. Ferhat Abbas Sétif 1**	**Examinateur**
LEMLIKCHI Wahiba	**Professeur**	**Université d'Alger 1**	**Examinatrice**
BOUDIAF Moussa	**M.C.A**	**Université d'El Oued**	**Examinateur**
ZAGHOUANE-BOUDIAF Hassina	**Professeur**	**Univ. Ferhat Abbas Sétif 1**	**Membre invitée**

Année universitaire : 2024/2025

جامعة سطيف 1 - فرحات عباس

Setif 1 University - Ferhat ABBAS

FERHAT ABBAS UNIVERSITY- SETIF1

FACULTY OF TECHNOLOGY

THESIS

Presented at Department of Process Engineering

In pursuit of the:

DOCTORAT

Domain : Science and Technology

Field: Process Engineering   **Special filed: Chemical Engineering**

Presented by

ZEMOURI Abd Errahmane

TOPIC

Green synthesis and physicochemical characterization of magnetic nanomaterials. Environmental treatment applications for adsorption of organic pollutants in aqueous media

Presented publicly on 06 / 03 / 2025 to the jury committee of:

BENANIBA Mohamed Tahar	**Professor**	**Univ. Ferhat Abbas Sétif 1**	**President**
BENTOUHAMI Embarek	**Professor**	**Univ. Ferhat Abbas Sétif 1**	**Supervisor**
BOUTAHALA Mokhtar	**Professor**	**Univ. Ferhat Abbas Sétif 1**	**Examiner**
LEMLIKCHI Wahiba	**Professor**	**University of Algiers 1**	**Examiner**
BOUDIAF Moussa	**M.C.A**	**University of El Oued**	**Examiner**
ZAGHOUANE-BOUDIAF Hassina	**Professor**	**Univ. Ferhat Abbas Sétif 1**	**Invited member**

Academic Year : 2024/2025

Dedications

I dedicate this work

To my dearest mother and my dearest father

To my brothers and sisters

To my dearest wife

May they find here a token of my gratitude, which, however great it may be, will never fully match their devolution.

Acknowledgments

SUMMARY

SUMMARY

SUMMARY

Chapter II: Materials And Methods

SUMMARY

SUMMARY

LIST OF FIGURES

List of figures

LIST OF TABLES

List of tables

GENERAL INTRODUCTION

General Introduction

Water is a vital resource for life on Earth. Approximately 78 % of the planet's surface is covered by water, mainly in the form of saltwater oceans, while only 2.5 % consists of usable freshwater. This limited availability makes it an indispensable element for all living organisms. However, increasing pollution due to industrialization and waste disposal threatens this precious resource. Industrial effluents contain various contaminants, including heavy metal ions, organic and inorganic compounds, aromatic substances, and dyes, posing significant risks to the environment and biodiversity.

Numerous industries contribute to environmental pollution by producing waste, particularly in agriculture, textiles, and paint manufacturing. The use of pesticides, fertilizers, synthetic dyes, pigments, and heavy metals significantly impacts water quality and disrupts ecosystems, leading to serious environmental and health risks. Among the various pollutants, dyes represent a major concern. These chemical compounds, widely used in coloring plastics, textiles, and certain food products, can cause severe contamination when industrial wastewater is improperly treated before being released, endangering both ecosystems and human well-being.

There are two main types of pollution sources: point sources and diffuse sources. Point sources originate from identifiable locations, such as factories, wastewater treatment plants, and septic systems, which discharge pollutants directly into water bodies. In contrast, diffuse sources are more challenging to pinpoint as they stem from widespread activities, including agricultural runoff carrying fertilizers and chemicals, waste from livestock, and discharges from construction sites and mines. Additionally, landfills can contribute to water contamination if pollutants seep into groundwater. This study focuses on a specific form of water pollution: wastewater released from textile dyeing industries.

Wastewater from the textile industry poses a serious environmental and health concern, as it degrades aquatic ecosystems and threatens drinking water quality. Proper treatment is essential before its release into natural water bodies to minimize its harmful impact.

Given the diversity and heterogeneity of their composition, treating textile wastewater requires the design of a comprehensive treatment process that ensures the removal of various

pollutants in successive stages. The preliminary step involves the removal of insoluble contaminants, followed by pollution reduction techniques that are typically implemented in the second stage. Due to the varied and complex nature of textile wastewater, an efficient treatment process must be designed to eliminate pollutants in successive stages. The initial phase focuses on removing insoluble contaminants, followed by pollution reduction techniques applied in the subsequent step.

Wastewater treatment methods differ depending on the nature of the contaminants (metal ions, organic compounds, nanoparticles, or micrometer-sized particles), the treatment approach (continuous or batch), and the final form of waste produced (solid sludge, highly concentrated solutions, or pollutant-laden particles). These techniques are also selected based on pollutant concentration, solubility, and process cost.

Typical wastewater treatment methods include physico-chemical processes (such as coagulation-flocculation), chemical treatments (like oxidation), biological approaches (where microorganisms break down pollutants), and adsorption. Among these, adsorption stands out for its simplicity and high efficiency. Its economic viability could be further improved by substituting conventional activated carbon with alternative, cost-effective adsorbents offering comparable or enhanced performance.

The advancements in water treatment, including the development of innovative materials, enhanced laboratory techniques, and technological progress in various processes, have promoted the use of bioresources and the exploration of eco-friendly solutions such as bio-adsorbents and bio-polymers. In this context, biomass emerges as a sustainable alternative to reduce the overuse of clays in wastewater purification.

This thesis was conducted at the Laboratory of Chemical Process Engineering (LGPC) and the Laboratory of Molecular and Nanostructured Chemical Engineering (LCIMN). Its aim is to develop composite materials capable of adsorbing organic pollutants (dyes and others) that can be utilized in adsorption processes where the separation of adsorbate and adsorbent is more manageable. This work also aligns with ongoing efforts to develop methods and explore new, effective, and cost-efficient materials for wastewater treatment, building on previous research conducted at LGPC.

The use of bentonite in adsorption processes can present separation challenges due to its colloidal dispersion in water. So far, techniques such as centrifugation and spontaneous precipitation have been employed to address this issue. However, recent research suggests modifying bentonite with magnetic nanoparticles, such as iron oxide (Fe_3O_4), and encapsulating it in alginate to facilitate its recovery using a magnetic field.

This thesis is divided into four parts. In Chapter I, we present the context of this work along with a literature review. We outline the materials and methods traditionally used for pollution treatment.

Chapter II focuses on the preparation of the various materials used in this study. It details the experimental techniques implemented, the sample preparation protocols, and the mathematical models applied for the quantitative analysis of the obtained results. Additionally, it incorporates computational investigations to further understand the interactions between the adsorbents and pollutants, providing theoretical insights that complement the experimental findings.

In Chapter III, we describe the chemical and physical characterization, along with the study of discontinuous adsorption on magnetic bentonite and magnetic bentonite beads using methylene blue as a model pollutant.

Chapter IV focuses on the chemical and physical characterization and the study of discontinuous adsorption on organophilic magnetic bentonite and organophilic magnetic bentonite beads, again using methylene blue as a model pollutant.

Finally, we present the conclusions of the study and the future prospects offered by the results obtained, particularly regarding the potential for using the adsorbent beads on a larger scale.

Thesis objective

The development of new composite biomaterials is a key aspect of this research. The adsorbent matrices are designed either in powder form (such as magnetic bentonite or organophilic magnetic bentonite) or encapsulated in calcium alginate, a natural polymer that enables the formation of composite beads (magnetic bentonite beads and organophilic magnetic bentonite beads). By utilizing natural, renewable, and abundant resources, this work aims to create a material with a lower environmental footprint. In this study, bentonite-based adsorbents were first synthesized, then magnetized and encapsulated in alginate.

All the materials analyzed demonstrated remarkable efficiency in eliminating organic pollutants. However, their application is limited by the difficulty of separating small particles from the effluent after adsorption. The encapsulation of powdered adsorbents in alginate beads addresses this issue, as it prevents their dispersion in the effluent and facilitates their extraction. Throughout this study, we focused on mastering the preparation of all adsorbents and their encapsulation in calcium alginate.

We also analyzed their physical and chemical properties and assessed their efficiency in adsorbing organic molecules. Specifically, we compared the adsorption capacities of our composite materials with those of other adsorbents developed from biomass by researchers. This study paves the way for potential applications in industrial wastewater treatment, providing a sustainable alternative to conventional methods.

CHAPTER I
Bibliographical Study

CHAPTER I
BIBLIOGRAPHICAL STUDY

I.1. Problem

The imminent danger of water resource depletion is highly tangible and noticeable in many areas. While limited access to drinking water has historically affected developing nations, developed nations are now also experiencing its consequences. This is primarily due to factors such as population growth, global warming, the addition of new water uses, expansion of agriculture and industry, and disregard for fundamental regulations [1].

Furthermore, water accessibility continues to decrease due to pollution, leading to a deterioration in the quality of water reserves and current high water usage. Unaddressed industrial waste presents a crucial environmental problem due to its toxicity, inability to degrade naturally, and resistance to traditional treatment methods [2,3].

The problem of water depollution has increased in importance, mainly due to the rising rigidity of drinking water constraints. Several sectors produce chemically inert contaminants that are challenging to break down using traditional treatment techniques. Consequently, there is a need for novel and more effective methods for controlling these discharges.

To address this problem, the subject is suggested to integrate and combine innovative techniques for environmental control. In this context, adsorption is increasingly recognized as a very efficient and promising technique for advanced wastewater treatment [4]. Adsorption techniques are currently acknowledged as cost-effective and efficient solutions due to their inexpensiveness, efficacy, and accessibility [5,6]. The process involves the interactions between pollutant molecules and adsorbent surfaces, resulting in an effective and essential method for removing pollutants [7].

I.2. Water pollution

Pollution is the harmful degradation of the environment caused by the addition of elements that either are not found in nature or exist in minimal quantities in the environment as a whole. It perturbs the ecosystem and has severe implications for human health [8].

Water pollution is a deterioration in water quality that makes its use dangerous for public health and irrigation and disrupts aquatic life. It affects surface water (rivers, lakes) and groundwater. It remains a major challenge, especially in developing countries that still need the technical and financial resources to incorporate new purification processes and where

water resources are less abundant [9].

Drinking water quality standards are becoming increasingly strict, and regulations are keeping pace with developments in analytical techniques to halt the spread of this pollution and reduce its consequences. The World Health Organization (WHO) regularly publishes guidelines on the quality of drinking water [10].

I.2.1. Sources of water pollution

Water pollution comes from various sources, including natural and human activities (domestic, agricultural, industrial, etc.).

I.2.1.1. Natural pollution: Hazardous materials can occasionally end up in water due to natural occurrences rather than human effort. Particularly high quantities of heavy metals are produced when water decreases or dissolves mineral formations. The amount of air contaminants that precipitation brings to the earth also surpasses WHO guidelines. Volcanic eruptions and submarine hydrocarbon spills can also cause water pollution [11].

I.2.1.2. Domestic pollution: It covers household wastewater and water discharged by collective facilities (hospitals, shops, etc.).

I.2.1.3. Agricultural pollution: It mainly concerns water-containing products from land applications (fertilizers, pesticides, etc.) [12].

I.2.1.4. Industrial pollution: Several compounds have been identified as pollutants resulting from industrial activity [13].

- Dyes (textile industries...),
- Pharmaceutical products (pharmaceutical industries, hospitals, etc.),
- Hydrocarbons (oil industries, transport, etc.),
- Heavy metals (tanneries, surface treatments, electroplating, metallurgy...),
- Acids, bases, and various chemical products (chemical industries, tanneries...),
- Organic materials and fats (slaughterhouses, food processing industries, etc.),
- Radioactive materials (nuclear power plants, radioactive waste treatment, etc.).

I.2.2. Main types of water contamination

Water pollution is caused by several toxic substances (contaminants) that are chemical or biological and can be pathogenic for humans.

I.2.2.1. Chemical contamination: Chemical risk is linked to geological elements or contaminants resulting from human activities. Excessive fertilizer use contributes excess nitrogen and phosphorus to watercourses and groundwater. Pesticides are a major environmental problem [14].Heavy metals (lead, cadmium, mercury, manganese, etc.) are not biodegradable. They form a family of pollutants that are very dangerous for the animal kingdom. Plants absorb it, and during the food chain, they collect and concentrate [15].

I.2.2.2. Microbiological contamination: Water can contain pathogenic microorganisms such as bacteria and viruses. The primary sources of microbial contamination in aquatic resources are the discharges from water treatment plants and hospitals [16]. As a result, epidemics can develop, limiting the daily use of water [17]. The virulence of certain epidemics has shown that traditional disinfection, particularly chlorination, eliminates most pathogenic bacteria but sometimes has no effect on other resistant microbiological agents and generates dangerous by-products (chlorine gas, etc.) [18].

I.3. Different types of pollutants

I.3.1. Heavy metals

The inorganic elements known as natural heavy metals possess a density that exceeds 5 g/cm3. The chemicals above can be identified in minute quantities across many environmental compartments. Once they exceed a predetermined critical threshold, they exhibit notable toxicity. Some metals (trace elements: Cu, Zn, Fe...) are necessary for the cellular metabolism of living organisms at very low concentrations. Above certain concentrations, however, they become toxic [19]. In contrast, certain elements, namely mercury, lead, chromium, arsenic, and cadmium, are widely acknowledged for their exceptionally high toxicity levels and lack of involvement in cellular metabolism, even when present in exceedingly low quantities. The generally uncontrolled discharge of heavy metals into the aquatic environment poses enormous environmental problems. The toxicity of these metals depends on their chemical form, degree of oxidation, concentration and rate of accumulation in the organism at each stage of the food chain [20].

The Table I.1 below sets out the concentration limits for heavy metals permitting indusrial liquid effluent discharges under Algerian regulations.

Table I.1: Limit values for heavy metals [21].

Element	Cd	Cu	Hg	Pd	Cr	Ni	Zn
Limit value (ppm)	0,2	0,5	0,01	0,5	0,5	0,5	3

I.3.2. Pesticides

Pesticides are used to control animals and plants that pose a threat to human health, wildlife, and the environment [22]. Chemically speaking, several groups of pesticides can be distinguished, characterized by their different persistence [23]. Following their use in agriculture at excessive concentrations, pesticides are dispersed into the environment, mainly into natural waters. These compounds, which are persistent and toxic to living organisms, are then ingested and accumulated, contaminating the entire food chain [24]. They can cause cancer or malformations in newborn babies. They are poorly biodegradable and active at very low doses. Their use and rate of discharge into water are strictly regulated [25,26].

I.3.3. Pharmaceutical pollutants

Pharmaceutical substances in the aquatic environment originate from various sources:

- Hospital effluents,
- Pharmaceutical industry effluents,
- Veterinary treatments used for farm animals,
- Contaminated urban water.

The most common form of contamination of surface waters (rivers, lakes, etc.) comes from pharmaceutical substances discharged by hospitals and collected in urban wastewater treatment plants. Some poorly biodegradable substances escape biological treatment and are discharged into rivers [27].

I.3.4. Dyes

Dyes are organic compounds, either natural or synthetic, that have the ability to permanently color the substrate they are applied to under specific conditions. The dye industry represents a significant economic market, as dyes are used in a variety of fields:

- Textile, fur and leather industry - Plastics industry,
- Building industry: paints and ceramics - Printing: inks and paper,

- Pharmaceutical industry - Cosmetics industry,
- Food industry - Oil industry.

The classification principles encountered for dyes are essentially based on their chemical structures and the techniques used for applying them to different substrates (textiles, paper, plastics, etc.):

I.3.4.1. Chemical classification

The classification of dyes based on their chemical structure is determined by the nature of the chromophore group.

I.3.4.1.1 Azo dyes: In Figure I.1, the structural composition of the azo molecule is depicted. Azo dyes are distinguished by an azo bond (-N=N-) linking two benzene rings within the molecule. Due to its notable resistance to light, acids, bases, and air, this dye has extensive application within the textile sector [28]. The presence of these compounds in industrial effluents is dangerous, as they are toxic, carcinogenic, stable, highly resistant to biodegradation and recalcitrant to the usual treatments [29].
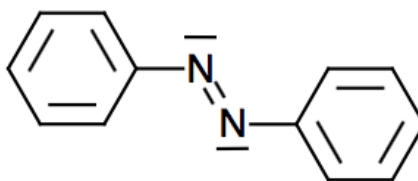
Figure I.1. Structure of the azo molecule.

I.3.4.1.2 Triphenylmethane dyes: Figure I.2 illustrates the structural composition of the triphenylmethane dye. Triphenylmethane is a derivative of methane, consisting of three phenyl rings attached to a central carbon atom. This hydrocarbon serves as a fundamental structure in many dyes.
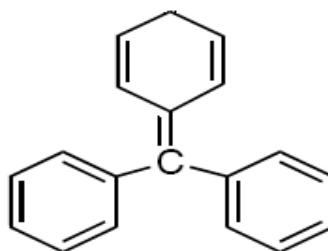
Figure I.2. Structure of triphenylmethane dye.

9

I.3.4.1.3 Indigo dyes: The structure of indigo is shown in Figure I.3. Indigo dyes take their name from indigo. This compound is recognized as one of the oldest known dyes, along with purple, a dibromo-6,6-indigo derivative. Several derivatives of this dye have been synthesized by attaching substituents to the indigo molecule. The selenated, sulfurated and oxygenated homologs of indigo blue exhibit notable hypochromatic effects, with colors spanning from orange to turquoise. Indigo dyes are characterized by remarkable resistance to washing treatments, while lightfastness is average. They are used in textiles, pharmaceuticals, confectionery and medical diagnostics.
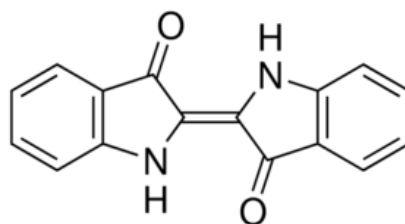
Figure I.3. Structure of indigo2-(1,3-dihydro-3-oxo-2H-indole-2-ylidene)-1,2-dihydro-3H-indole-3-one (IUPAC name).

I.3.4.1.4 Xanthene dyes: Figure I.4 shows the molecular structure of a xanthene dye. Xanthenes are organic compounds with a tricyclic structure. They are composed of a pyran ring flanked by two benzene rings. They are used in food, cosmetics, textiles, and printing dyes [30].
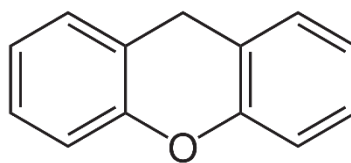
Figure I.4. Molecular structure of a xanthene dye.

I.3.4.1.5 Anthraquinone dyes: The anthraquinones shown in Figure I.5 are derived from anthracene. The fundamental molecule in this group of dyes is anthraquinone, which has the chromophoric carbonyl group ($>C=O$) on a quinone ring. It occurs naturally in certain plants (borage, senna, aloe, rhubarb). These products are utiliezd to color polyester, acetate and cellulose triacetate fibres.
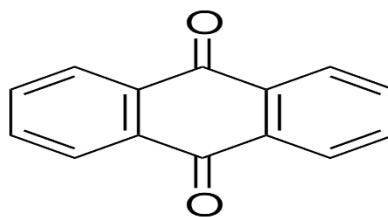
Figure I.5. Anthraquinone molecule (9,10-dihydro-9,10-dioxoanthracein, anthracene derivative).

I.3.4.1.6 Phthalocyanine dyes: A complex structure with a central metal atom characterizes phthalocyanines. They are obtained by reacting dicyanobenzene in the presence of a metal halide. They are mainly used in manufacturing inks, paint pigment, and dyeing textile fibres. For example, Figure I.6 shows the structure of copper phthalocyanine.
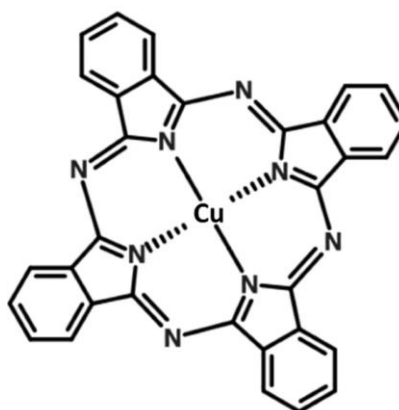
Figure I.6. Phthalocyanine structure: copper phthalocyanine.

I.3.4.1.7 Nitrated and nitrosated dyes: The Figure I.7 shows the structure of a nitro and nitrosated dye molecule. Nitro and nitrosated dyes are characterized by a nitro group (-NO2) in the ortho position of an electron donor and possess a simple structure. These nitro compounds form the basis of anionic disperse dyes or pigments, limited to yellow and brown shades. These dyes are less widespread and of little industrial application.
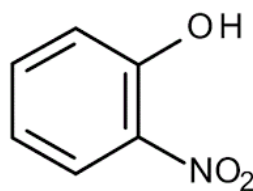
Figure I.7. Structure of a nitro and nitrosated dye molecule.

I.3.4.2. Tinctorial classification

Chemical classification interests dye manufacturers, but dyers prefer to classify dyes by field of application. This provides information on the dye's solubility in the dye bath, its affinity for the different fibers, and the type of fixation used.

I.3.4.2.1 Acid or anionic dyes: Due to their sulfonate or carboxylate groups, these compounds are soluble in aqueous media and have one to four sulfonate groups. The dye-fibre affinity results from ionic bonds between the dye's sulfonate anions and the textile fibre's ammonium groups. They are used for dyeing polyamide, wool, silk, and acrylic fibres. The Figure I.8 shows an example of acid dyes (C.I. Acid red 27).
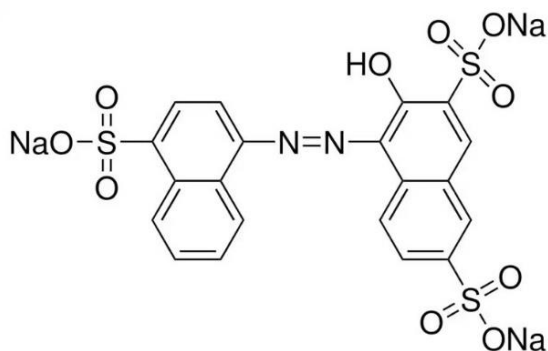
Figure I.8. Acid dye (C.I. Acid red 27).

I.3.4.2.2 Basic or cationic dyes: Basic or cationic dyes are salts derived from organic amines. They are soluble in water and form strong bonds between their cationic sites and the anionic sites of the fibres. Many basic dyes have a hazardous impact on the environment. This type of dye can be applied to cotton, polyamide, and modified polyester. Figure I.9 shows an example of cationic dyes (Methylene blue).
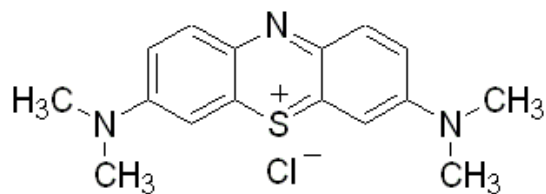
Figure I.9. Basic dye (methylene blue).

I.3.4.2.3 Developed or insoluble azo dyes: The Figure I.10 shows the structure of insoluble azo dyes. This type of dye is insoluble. It develops directly on the fiber through a coupling reaction between a diazotized base and a coupling agent. This class of dyes makes it possible to obtain very solid dyes on cellulose fibers.
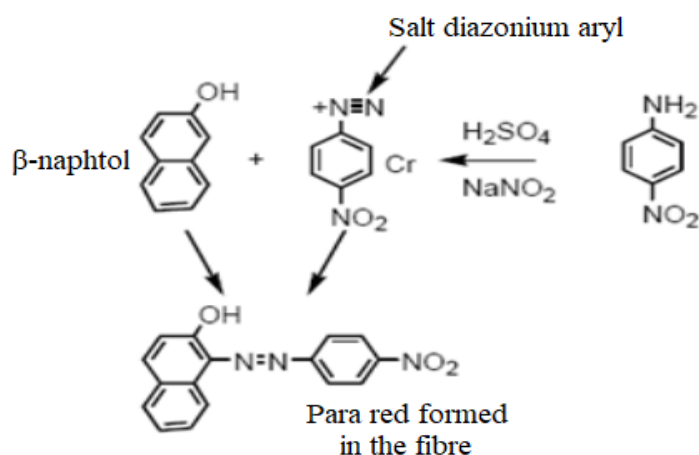
Figure I.10. Insoluble azo dye.

I.3.4.2.4 Vat dyes: This colorant is devoid of solubility in water. The activity occurs in two distinct phases. Following the alkaline reduction of the dye to generate a leuco derivative, a soluble form, and the dye is then re-oxidized in situ to its original insoluble form, enabling it to be associated with the fiber. Vat dyes are well-suited for coloring cellulose fibers, mainly cotton and animal fibers. Figure I.11 shows the structure of vat dye (Indigo).
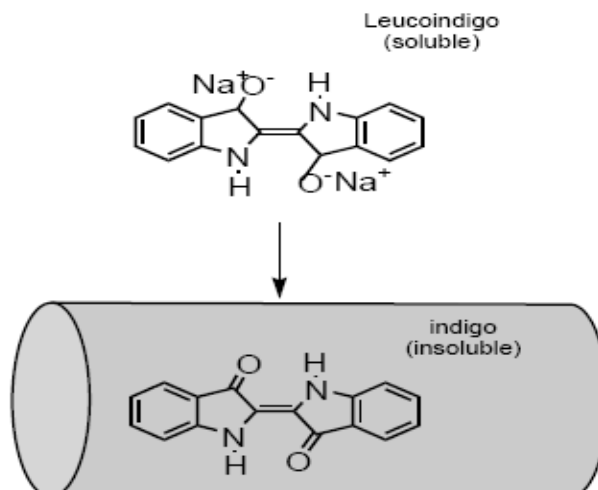
Figure I.11. Vat dye (Indigo).

I.3.4.2.5 Reactive dyes: The particles are nominated according to their reactive chemical characteristics, specifically those of the triazine or vinyl sulfone type, guaranteeing a robust covalent attachment to the fibers. When dissolved, these substances include chromophore groups generally derived using the azo, anthraquinone, and phthalocyanine groups. Their specific uses involve coloring cotton, wool, and polyamides. A representative example of this family is shown in Figure I.12.
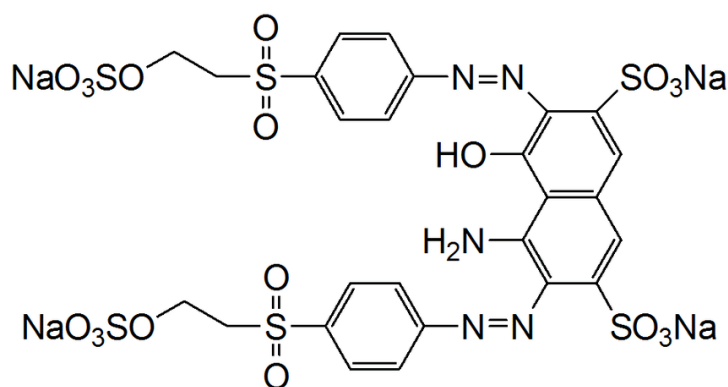
Figure I.12. Reactive dye (Reactive Black 5).

I.3.4.2.6 Direct dyes: Figure I.13 shows the structure of a direct dye molecule. These colors are anionic and soluble in aqueous solutions. They adhere to fibers via feeble bonding, which accounts for their inadequate resistance to moist testing such as

water, washing, and sweat. These dyes are the most cost-effective for dyeing cellulose fibers like cotton.
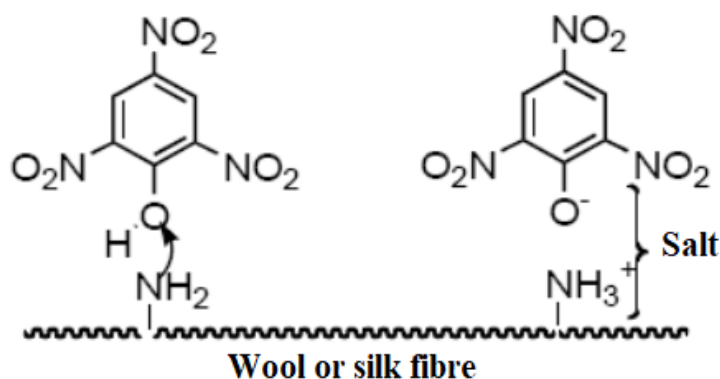
Figure I.13. Structure of a direct dye molecule.

I.3.4.2.7 Mordant dyes: Mordant dyes are distinguished by the existence of functional groups that can undergo reactions with metal salts bound to the fibre following pre-treatment. The consequence is the creation of a highly compact and durable complex. Industrial dyeing predominantly utilizes dichromate-based salts; hence, their designation as chromium dyes. Figure I.14 shows the chemical structure of Mordant Violet 40 dye.
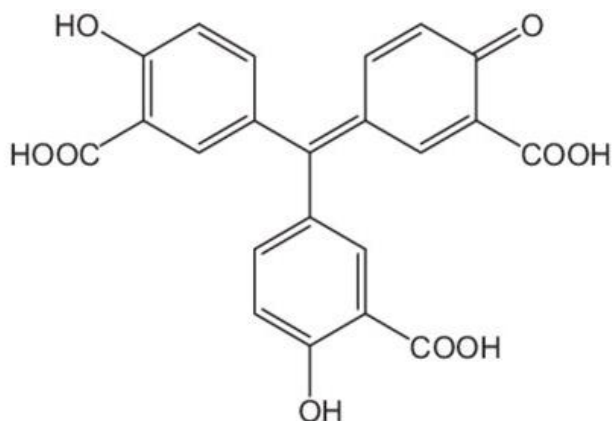
Figure I.14. Chemical structure of Mordant Violet 40 dye.

I.4. Textile industry effluents

Interestingly, the textile business consumes more than 60% of the global dye production, necessitating large quantities of water for their dissolution. After their activities, they discharge large quantities of wastewater into aquatic environments without any restrictions or controls, generating severe water pollution.

I.4.1. Toxicity of aquatic environments due to textile industry discharges

The contamination of water resources by pollutants of various origins is a topical issue. In particular, effluents from the textile industry are a severe source of toxicity in aquatic environments. These settings are distinguished by vibrant hues, elevated pH levels, substantial suspended solids (SS), and elevated chemical oxygen demand (COD) [2]. Textile dyes are not biodegradable under aerobic conditions due to the complexity of their chemical structures, formed mainly of aromatic rings; this gives them a highly toxic and recalcitrant character [31]. Consequently, these organisms can endure for an extended period in these habitats, leading to significant disturbance to the inherent processes of plant and animal life, contamination of water sources utilized for agricultural irrigation (affecting the hygienic attributes of agricultural products, etc.). and severe harm to public health [32].

I.4.2. Environmental impacts and risks

Environmental damage from the textile business mainly stems from the release of recalcitrant dyes and dyeing auxiliaries, including salts, surfactants, and organic acids, into water bodies. This is a significant contributor to pollution and eutrophication and poses a possible bioaccumulation risk that impacts humans via the food chain [33].

I.4.3. Legislation on textile waste

Legislation requires textile effluents to be purified before discharge. This involves installing a balancing tank for partial reciprocal neutralization of the effluents. The effluent must then be treated in a pH-corrected treatment plant to eliminate the pollutant load in compliance with discharge standards [34]. The table below sets out the limit values of the parameters to be controlled for textile industry discharges by Algerian regulations.

Table I.2: Limit values for textile effluent discharge parameters [21].

Parameter	Limit values
Temperature (°C)	30
pH	6,5 – 8,5
BOD$_5$ (mg/L)	150
COD (mg/L)	250
Settleable matter (mg/L)	0,4
Undissolved matter (mg/L)	30
Oxidability (mg/L)	100
Permanganate (mg/L)	20

I.5. Classic water treatment techniques

Industrial effluent can be treated using various processes: physical, membrane, thermal, biological, or chemical. The choice of one or other of these processes depends on certain parameters, such as the flow rate, composition, and concentration of the effluent, the type of reuse, and the size of the installation.

I.5.1. Physical treatments

Particulate separation from treated water is achieved by physical processes, including settling, sedimentation, flocculation, filtration, flotation, extraction, and adsorption [35]. These techniques are based on simple, easily applicable principles that can be scaled up. However, they represent a simple displacement of pollution from one medium to another but can be coupled with a pollutant destruction process [36].

I.5.2. Membrane treatments

These treatments are separation procedures that employ a membrane as the effective separating agent. An *osmotic barrier* is a physical obstruction that separates two compartments, allowing unwanted substances such as pollution, pathogens, and color molecules to be prevented and selectively flow through the filtered water. Operating requires driving power to elevate the pressure of the aqueous phase, which needs to be filtered. Several types of membranes are employed for wastewater treatment:

- The pore widths of porous membranes for microfiltration range from 100 to 10,000 nm; for ultrafiltration, they range from 1 to 100 nm; and for nanofiltration, they range from 0.1 to 1 nm.

- Dense membranes, such as ion exchange membranes and reverse osmosis membranes, notably for seawater desalting and ultra-pure water production [36].

I.5.3. Heat treatments

Thermal treatments use high temperatures to break down organic molecules and mineralize them into CO2 and H2O. The thermal treatment most commonly used industrially is incineration. Therefore, these processes require large quantities of energy and should be limited to treating effluents rich in organic matter. The combustion of the latter offsets the energy required to vaporize the water. In addition, this type of treatment may require the installation of a device to treat the fumes emitted [37].

I.5.4. Biological treatments

The presence of organic pollutants in water is a real danger, and their degradation by micro-organisms is the biological treatment ecosystems use to purify natural environments. These biological processes occur in two modes: aerobic treatment involves the presence of oxygen, while anaerobic treatment occurs in its absence. [38].

I.5.4.1. Aerobic treatment: Bacterial bed reactors, consisting of an activated sludge unit where bacteria break down pollutants in an aerated environment, are used for this purpose. After purification, sedimentation in a settling tank separates the sludge from the wastewater. Some sludge is recycled, while the surplus is discharged by pressing or centrifuging. This technique has long been a treatment method for many organic pollutants and has demonstrated its effectiveness for a category of textile discharges [38].

I.5.4.2. Anaerobic treatment: Anaerobic digestion of organic matter leads to mineralization without oxygen, producing CO_2, CH_4, and H_2O. The method successfully addresses effluents, including significant organic waste, and requires a high chemical oxygen demand [39]. Effluent treatment facilities also use it to produce significant quantities of biogas, primarily methane [40].The efficacy of these biological mechanisms in reducing pollution is sometimes constrained, thereby necessitating the integration of other approaches to decrease the amount of pollutants.

I.5.5. Hybrid processes

Every treatment technique has advantages and disadvantages. A single technique is unlikely to clean up an effluent containing pollutants from various sources. Combining several existing techniques enables the advantages of each to be fully exploited. Several methods have been developed to eliminate textile dyes, including ozonation combined with biological treatment [41], adsorption combined with photocatalysis for phenol removal [42], and applying photocatalysis with membrane processes for humic acids, dyes, and 4-nitrophenol removal [43].

I.6. Pollution control method chosen for this study

Pollutant removal methods vary according to the target substances (metal ions, organic substances), particle size, effluent removal mode (continuous or batch) and the final nature of the solutions and target substances (solid sludge, highly concentrated solutions, particles saturated with pollutants).

Dye removal has been extensively studied using a various methods: biological (aerobic and anaerobic treatment) [44], physical including coagulation [45], ultrafiltration [46], photocatalysis [47], oxidation-reduction [48], biodegradation [49], electrochemical treatments [50] and others. Unfortunately, all these methods have a high cost, which has encouraged the use of adsorption, which appears to be cheaper, easier and more effective [4,7].

I.7. Adsorption

Adsorption is a method through which a substance accumulates in an interface of two states, frequently consisting of gas and solid or liquid and solid. It originates in the forces of attraction between molecules, of varying nature and intensity, responsible for the cohesion of condensed phases, whether liquid or solid. A molecule that is more strongly attracted to the other molecules of two phases will find an energetically favorable position on the surface of the phase that attracts it most; which is known as the adsorbent, and the molecules that adhere to this surface are referred to as the adsorbate. Absorption occurs if the energetic or kinetic conditions permit the molecule to enter the absorbing phase [51]. This phenomenon results from the presence of unbalanced forces at the surface of the solid, leading to two types of adsorption: chemisorption and physisorption.

I.7.1. Chemical adsorption (chemisorption)

In this type, one or more covalent or ionic chemical bonds are formed between the adsorbate and the adsorbent. Chemisorption is irreversible and leads to a modification of the adsorbed molecules. Except for molecules directly attached to the solid, these molecules cannot be collected on multiple monolayers [52]. The adsorption heat is relatively high, measured between 20 and 200 Kcal/mol. The proximity of the surface to the adsorbed molecule is far smaller than physisorption. Chemisorption is found in most reactions as an intermediate step in the catalytic reaction, and identifying and understanding the behavior of chemisorbed species is directly involved in understanding heterogeneous catalysis. Chemisorption is linked to local defects in the atomic structure of the solid, and the number of chemisorption sites is much smaller than that of physisorption [53].

I.7.2. Physical adsorption (physisorption)

It occurs at low temperatures, with the molecules adsorbing on several layers, with heats of adsorption often below 20 Kcal/mol. Interactions between solute molecules and the solid surface are mediated by electrostatic forces resulting from interactions between the electronic clouds of particles and surface atoms. These long-range forces are of the Van der Walls type. Physisorption is rapid, reversible and does not modify the adsorbed molecules.

Physisorption is of particular interest because it enables measurement of the adsorbing solid's specific surface area and the average pore diameter and distribution [53,54].

I.8. Adsorbents

The adsorbents may be either inorganic or organic substances. They may have either natural or synthetic origins. Adsorbents may encapsulate minerals and/or functional groups (carbonyl, carboxyl, hydroxyl) on their surface. The adsorption properties of adsorbents are determined by the interactions between gases or liquids and the surface functional groups [55]. Therefore, adsorbents are immensely abundant. We shall focus on the materials that have been synthesized or prepared in this thesis work to avoid dispersing our views and discussing solely our interests.

I.8.1. Clays

The inexpensive cost and quantity of natural clays make them a widely used choice for adsorbent materials. Clay is a phrase that encompasses a rock formation, the raw material it produces, and a particle size range consisting of mineral particles with grain sizes smaller than

two micrometers (< 2 μm). The development of this feature is associated with the modification and hydrothermal conversion of ash derived from volcanic tuffs abundant in glass. The clay rocks created have a chemical composition that closely resembles the average composition of the Earth's surface. The composition comprises a minimum of 50% hydrated alumina silicates and a small selection of related minerals, including iron oxides, hydroxides, carbonates, quartz, and others. Clay-humus complexes are frequently found in association with organic materials. The Oranie region in western Algeria is home to the most substantial quantities of clay minerals with economic importance. The Maghnia (Hammam Boughrara) quarry is projected to have reserves of one million tonnes, while the Mostaganem (M'zila) quarry is predicted to have reserves of two million tones.

I.8.1.1. Clay structure

A fundamental crystal lattice is formed by two crucial elements, silicon, and aluminum, surrounded by oxygen and hydroxyls. Aluminum is positioned at the center of an octahedron, while silicon is at the center of a tetrahedron. When multiple tetrahedra or octahedra are connected, they create a matching stratum (refer to Figure I.15):

I.8.1.1.1 Tetrahedral layers: These are primarily siliceous SiO_4. The thickness of the tetrahedron is 3 angstroms, with oxygen occupying the vertices and Si or Al occupying the core [56].

I.8.1.1.2 Octahedral layers: This is primarily aluminous $Al(OH)_6$. Octahedra have a thickness of 4 angstroms, and their apices are filled by oxygen or hydroxyl atoms, while their centers are filled by either an aluminum atom or magnesium [56].

- The structure is termed dioctahedral when Al^{3+} or another trivalent metal ion occupies two of three cavities in the octahedral layer.
- The trioctahedral structure [56] is formed when divalent metal ions fill all octahedral cavities.

I.8.1.1.3 Interfoliar space: These structures can be either empty or filled with anhydrous or hydrated cations. Tetrahedral layers (Si^{4+}, Al^{+2}, Fe^{3+}) and octahedral layers (Al^{3+}, Mg^{2+}, Fe^{2+}, or Mg^{2+}, Li^+) can exhibit isomorphic substitutions. These swaps lead to a deficiency of positive charges, imparting a negative charge to the layers. The negative charge is offset by compensatory cations outside the thin sheet.
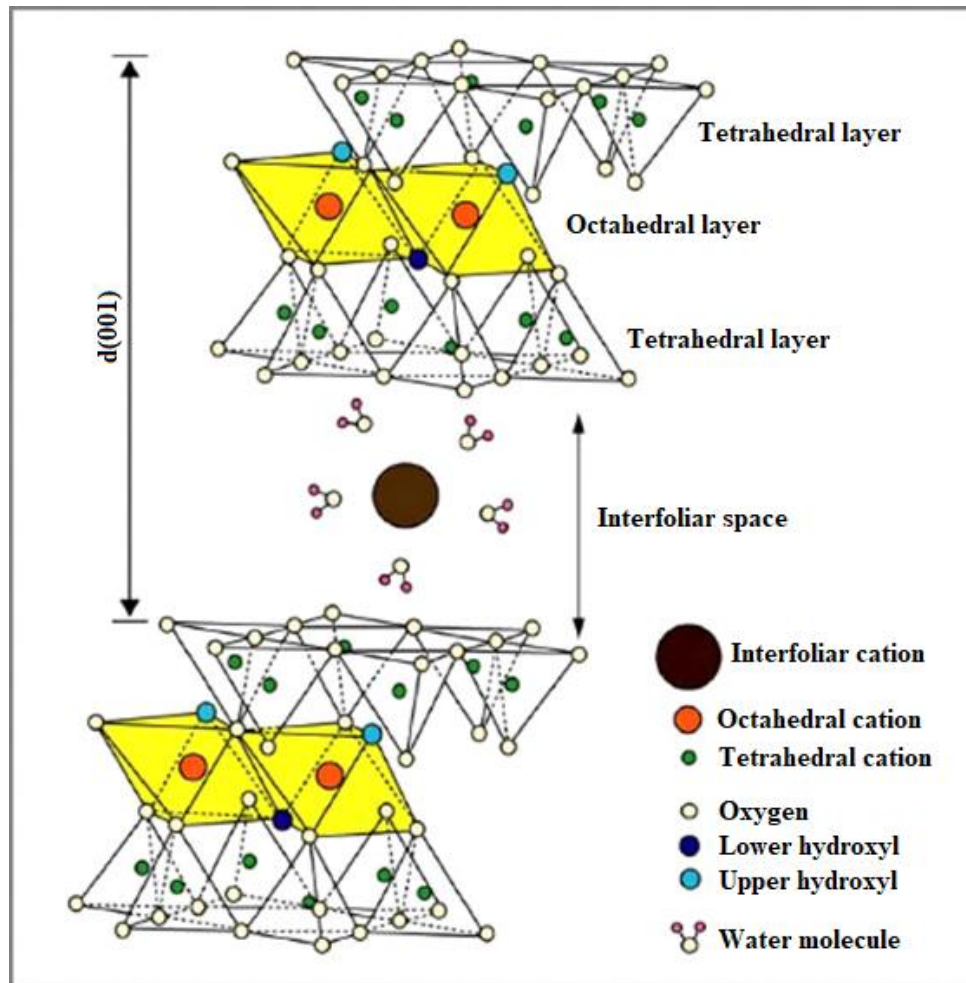
Figure I.15. Schematic representation of bentonite structure [57].

I.8.1.2. Clay properties

Clay minerals are primary components of the Earth's crust. Their function is essential in several environmental domains, ranging from geology and pedology to water purification. Their traits arise from the inherent attributes of clays (such as chemical composition, structure, and morphology) and the physico-chemical processes in which they are present. The most crucial morphological features that define their influence on interface phenomena are their size, shape, and specific surface area [58]. Their formation relies on granulometry, mineralogical structure, and filler distribution. The granulometry of clays imparts characteristics akin to those of colloidal materials. When clays are structured into sheets and inter-foliar spaces of different sizes, they exhibit the following general features and properties:

- Clays exhibit the characteristic of adsorbing specific anions and cations and preserving them in a condition conducive to their exchange with other ions in a surrounding solution. The cation exchange capacity (CEC) is a crucial property pertaining to cations present in the interfoliar space and surface and contact cations. Monovalent and divalent cations (Li^+, Na^+, K^+, Ca^{2+}, or Mg^{2+}) substitution capacity refers to the amount of cations that other cations may replace to offset the negative charge of 100 grams of clay.

- Although small, clays possess a significant specific surface area, which is the combined total of their external and internal surface areas. This characteristic is a crucial factor in accurately characterizing clays. Undoubtedly, the number of distinct surfaces increases as the soil becomes finer.

- In general, all clays can absorb water between the layers of their structure, resulting in fluctuations in their volumes and thus causing swelling. Swelling minerals exhibit a fundamental inter-foliar region measuring 10 Å. This distance changes based on the level of hydration. The thickness required for incorporating a layer of water around the inter-foliar cation is approximately 12.5 Å, whereas it is roughly 15 Å for two layers. These hydration processes result in a significant volume increase of up to 95%. Additionally, clay minerals, such as fibrous clays, have absorbed water but do not exhibit swelling characteristics.

I.8.1.3. Organophilic clays

The adsorption characteristics of clay minerals can be emproved by modifying them, increasing their usefulness as natural materials. These physicochemical or thermally-based alterations mainly involve ionic exchange with organic or inorganic cations, grafting of organic molecules, acid activation, calcination, and other similar processes. When cationic surface-active molecules are grafted onto clays, the original hydrophilic nature of the clay is converted into a hydrophobic and organophilic state, and the basal distance of the clay mineral also increases. The surfactant structure's characteristics determine the organophilic clay's basal distance and grow proportionally with its size. Molecular surfactants are surface-active compounds that consist of a hydrophilic polar head and an apolar aliphatic chain. The exchange reaction involves the substitution of the cation by the polar head of the surfactant, resulting in the surfactant settling in the inter-foliar region and rendering the clay

organophilic. The characteristics of the polar head exhibit variability. The composition may consist of ammonium or phosphonium cations ref [59].

I.8.2. Alginate

Brown algae and bacteria synthesize polysaccharide alginate. Stanford independently identified, isolated, and obtained a patent for alginic acid in 1881. As a structural element of marine brown algae, the polysaccharide is known to make up to 40% of the solid content and is primarily synthesized in the intercellular mucilage. Alginate extraction from seaweed depends on the solubility of the polymer alginic acid in water. Polymer: Alginic acid is aqueous and insoluble but is soluble in monovalent cation salts like sodium (Na^+) or potassium (K^+). Consequently, pH variations allow for its purification and separation from other constituents [60]. Figure I.16 shows an example of sodium alginate production from algae.
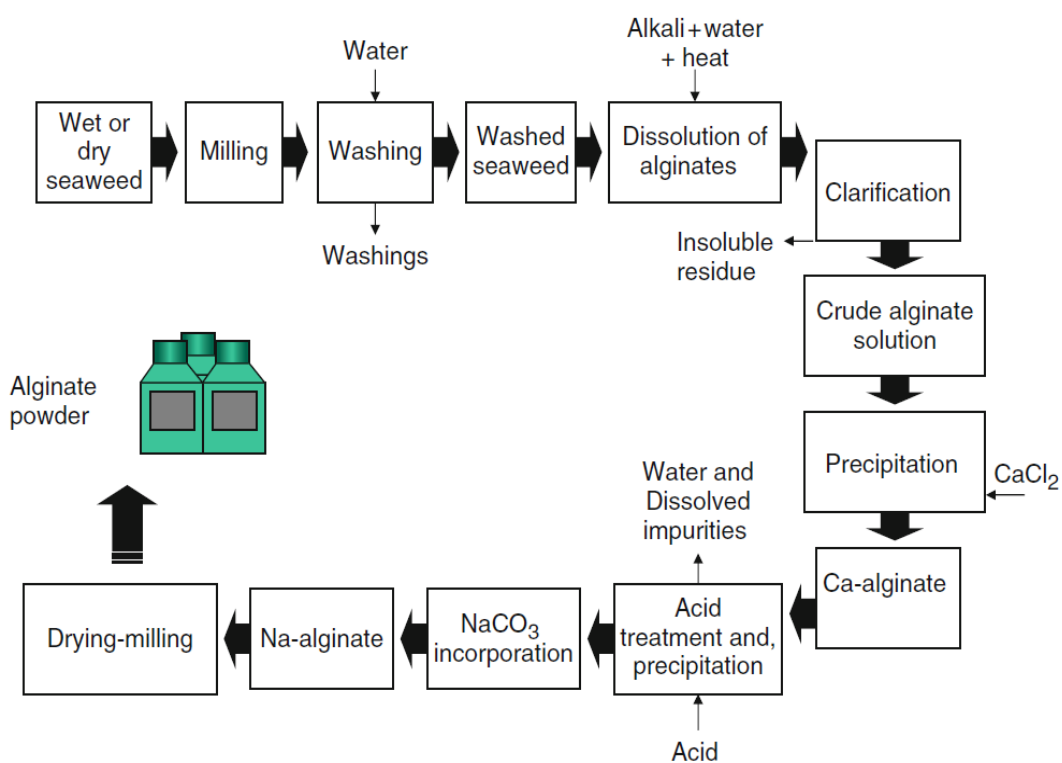
Figure I.16. Production of sodium (calcium) alginate from seaweed.

I.8.2.1 Alginate structure

Among the exopolysaccharides are alginates. ß-D-mannuronic acid (M) and α-L-guluronic acid (G) are monomers of linear binary copolymers, alginates, which are connected by β-(1-4) and α-(1-4) glycosidic linkages. The M and G units are organized into blocks, creating recurring sequences that lend the alginate chains their characteristics.

In Figure I.17, these blocks are shown to create homopolymeric regions consisting of M motifs (referred to as M blocks), G motifs (referred to as G blocks), or regions of alternating structure (referred to as MG blocks). Substances can be separated via partial hydrolysis followed by fractionation.
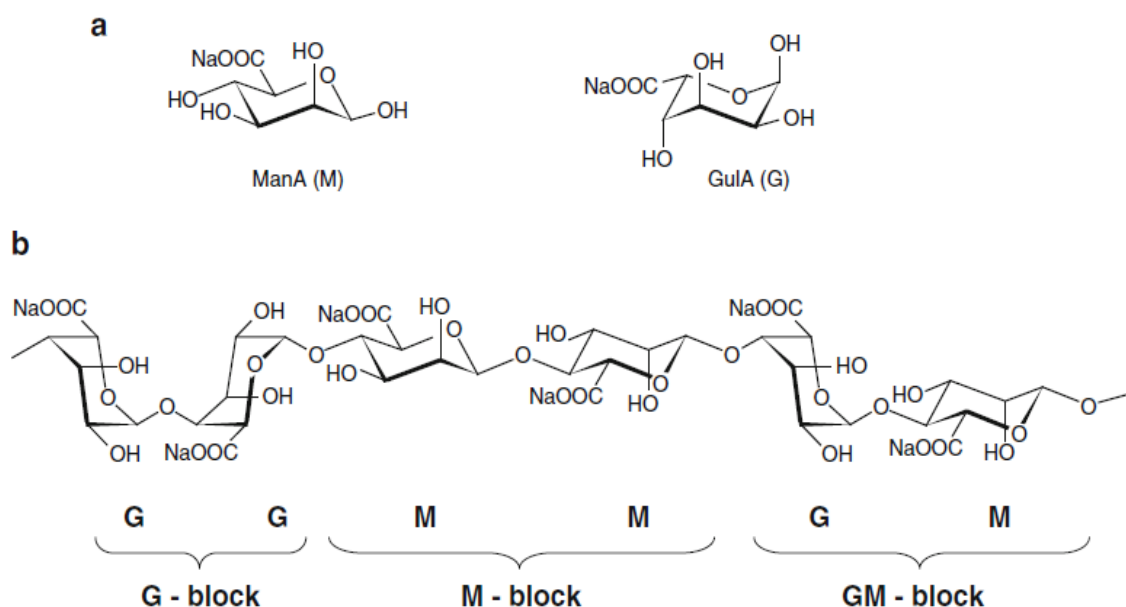
Figure I.17. Representation of the chemical structure of alginate. (a) The ß-Dmannuronic acid conformation acid (M) and the conformation of α-L-guluronic acid (G). (b) the composition of alginate blocks with G-block, M-block and MG-block [61].

I.8.2.2 Physico-chemical properties of sodium alginate

I.8.2.2.1 Solubility of sodium alginate: The solubility of alginate in water is limited by three critical factors: the pH of the solution influences alginate solubilization. Phase separation or hydrogel formation can occur if the pH of the alginate-containing solution is equal to or less than the pKa of mannuronic acid (pKa = 3.38) or guluronic acid (pKa = 3.65). Alginates' sensitivity to solution pH is influenced by numerous factors, including molar mass, chemical makeup, and block sequence. Alginates with

increasing alternating sections (MG blocks) will undergo precipitation at lower pH levels than alginates with more uniform blocks (poly-M and poly-G).

- The solubility of alginate in aqueous media is controlled by the ionic strength of the solvent, which has a significant impact known as the "salting-out" effect.

- The solubility of alginate is notably affected by the concentration of gelling cations in the solvent [62].

I.8.2.2.2 Gelation of alginate: The physical characteristics of alginate were primarily identified during the 1960 and 1970. A distinguishing feature of alginate, unlike other gelling polysaccharides, is its capacity to form gels with divalent cations. Furthermore, the sol-gel transition of the material is unaffected by changes in temperature.

The gel formation process is facilitated by the contacts among G-blocks, which conjoin to create robust cross-links when divalent cations are present. MG blocks, along with G blocks, also contribute to the formation of weak junctions. In consequence, alginates with a high G concentration form more robust gels. The sequence of decreasing affinity for divalent ions by alginates is as follows: Pb > Cu > Cd > Ba > Sr > Ca > Co, Ni, Zn > Mn. The basis for this interaction is the "egg-box" model [63], where each divalent ion can interact with two neighboring G residues or those from two opposing chains. Undoubtedly, Ca^{+2} is the predominant cation employed in alginate gel production (Figure I.18).
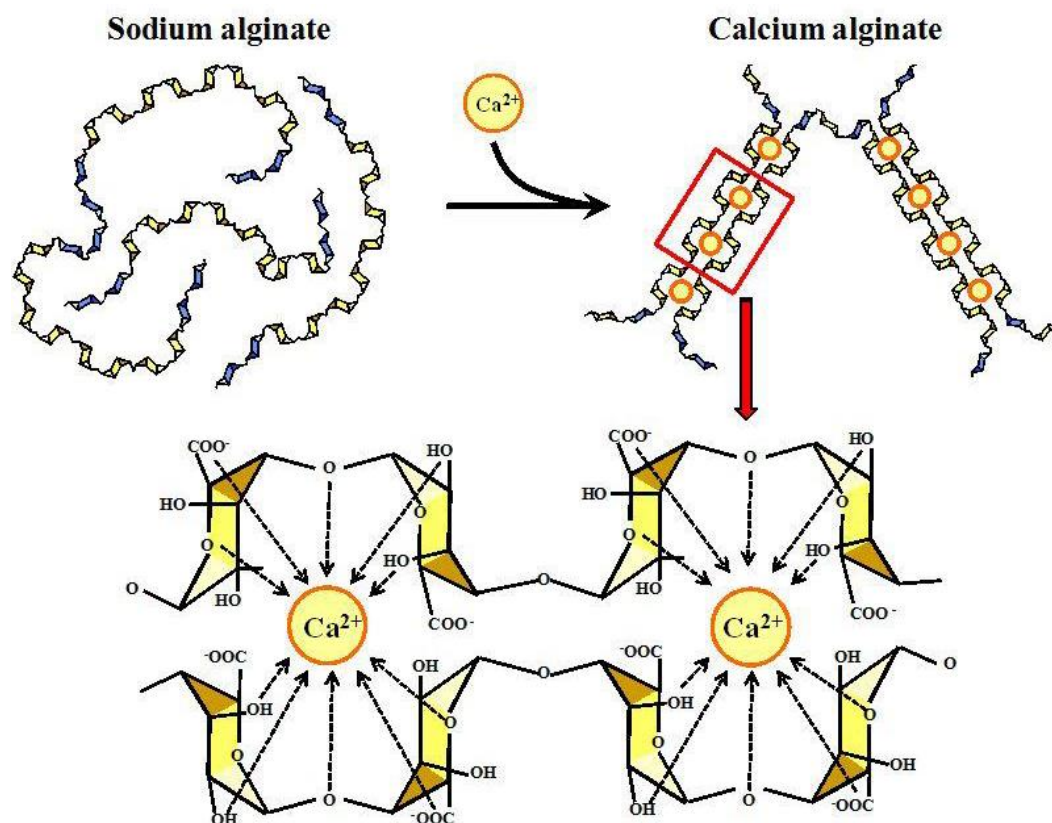
Figure I.18. Ionotropic gelation of alginate. Egg-box model [64].

An internal gelling technique and a diffusion technique are the two fundamental approaches for gelling alginate.

An internal gelling technique involves the controlled release of calcium ions from a calcium source that is initially present inside the alginate (a mixture of $CaCO_3$ in the alginate solution, which releases Ca^{2+} ions by chemical reaction).

Within the external diffusion procedure, calcium ions are transported into the alginate solution from an unbounded reservoir (a little amount of alginate is submerged in a bath that contains a calcium salt). Due to its very fast gelation kinetics, this technique is commonly employed to immobilize biological active components in a gel bead. In general, the viscosity of a substance rises quickly with both the concentration and length of the molecules, and falls quickly with rising temperature [65].

I.9. Composite materials

Adsorption materials derived from clay have been extensively investigated for their application in wastewater treatment. Despite their effective adsorption of organic and inorganic contaminants, the particle size of these materials (ranging from nanometres to micrometers) is a constraint on their application in pollution control systems. Furthermore, these finely fragmented substances show challenges in their separation during an adsorption procedure. Therefore, shaping these materials to achieve larger aggregates and consistent particle size is a crucial and almost essential stage in their industrial application. An economical and eco-friendly method for immobilizing a substance in a hydrogel matrix while preserving its adsorption characteristics is encapsulating a material in a polymer matrix (alginate). Gel beads of consistent size provide benefits in terms of their enriched concentration of active constituents and their convenient application in both continuous and discontinuous systems. Composite materials can be retrieved via straightforward separation and regenerated following use and saturation. These composite materials significantly decrease operational expenses.

I.10. Magnetism in water treatment

Regardless of their high adsorption capability, the challenge of retrieving these adsorbents charged with pollutants persists. The objective of this study is to synthesize magnetic adsorbents, which we refer to as "mag sorbents." Undoubtedly, the integrated magnetic and adsorbing characteristics within a single material present a fascinating challenge that can address the issues associated with retrieving pollutant adsorbents.

The use of magnetic materials in water treatment could overcome some limitations of existing techniques. Specifically, membrane separation is a very efficient technique, but its vulnerability lies in the occurrence of blockage. Conversely, increasingly effective membrane-based techniques are being developed. Nanofiltration, for instance, in the case of drinking water treatment plants, is a very efficient technique. However, it is also prohibitively expensive. The residue produced after physicochemical and biological treatment also presents challenges in terms of preservation. Regarding adsorbents, activated carbon is presently the most efficient, but it is expensive and challenging to retrieve, resulting in material wastage.

Incorporating magnetism into water treatment procedures has the potential to expedite the separation of waste from effluent, a current unsolved issue [66].The fundamental concept of magnetic separation in pollution control is the introduction of magnetic particles into the

medium, which adsorb different contaminants (whether organic or inorganic) and are then lifted by applying a magnetic field gradient.

Magnetic separation has a long history, with the earliest endeavors in this domain dating back to 1905. This technique was employed in ore processing to eliminate magnetic impurities by attracting them with an external magnetic field gradient using electromagnets [67] Advancing this approach has resulted in incorporating iron oxide particles into water with high concentrations of heavy metals. These particles function as solid centers around which the oxides of the cations that need to be separated undergo condensation. The magnetic particles and their impurities are subsequently retrieved using magnets [68]. This approach is straightforward and efficient but limited to metal cations that can form precipitates within iron oxide.

Increasingly, academic scholars are focusing on developing magnetic adsorbents with exceptional performance. Maghemite γ-Fe_2O_3 and magnetite Fe_3O_4, readily synthesized by alkaline coprecipitation, are particularly well-known magnetic iron oxides. They are capable of use independently.

The interaction between nanoparticles and biopolymers is a topic of extensive study. It is possible to incorporate nanoparticles into the biopolymer matrix. Materials such alginate [69] and chitosan [70,71] integrated with magnetic nanoparticles have been synthesized for the purpose of dye elimination. Metallurgical removal using magnetic alginate beads [72,73]. Biopolymers can be biopolymerized onto magnetic particle surfaces. To absorb metals and/or organic contaminants, magnetic nanoparticles have been modified by grafting chitosan, alginate, and cellulose onto them [74].

Therefore, research on green adsorbents is currently flourishing in academia. The research on magnetic adsorbents is limited but has recently experienced remarkable growth. Nevertheless, the magnetic materials employed suffer from inadequate control. The specialized knowledge of the Chemical Process Engineering Laboratory in this domain has proven valuable to us in achieving proficiency in synthesizing magnetic adsorbents.

I.11. Previous work on the removal of organic pollutants by adsorption

In **2009**, **Hong et al**., studied the impact of temperature on the adsorption of methylene blue by bentonite. The adsorption data analysis revealed that the Redlich-Peterson model was the best fit. Adsorption was endothermic and spontaneous, as indicated by thermodynamic parameters.

In **2011**, **Hao et al**., examined the impact of adsorbent dose, initial dye concentration, pH and magnetic field on methylene blue adsorption. Optimal conditions included a pH of 7 to 8 and an adsorbent dose of 1 g/L. The magnetic field inhanced the adsorption coefficient of the Freundlich model by 49% and increased the rate constant of the pseudo-second order by 143%, thereby enhancing the adsorption capacity of the organic bentonite.

In **2013**, **Auta et al**., explored the use of a composite of modified clay ball (MBC) and chitosan (MBC-CH) for methylene blue (MB) adsorption in a fixed bed column. The results showed that MBC-CH has a high adsorption capacity (142 mg/g) compared with MBC (70 mg/g). Adsorption is influenced by the initial dye concentration, the height of the adsorbent layer and the influent flow rate. MBC-CH retains a good adsorption capacity even after several regeneration cycles, making it effective and durable for decontaminating water by adsorption of cationic dyes.

In **2013**, **Hashem et al**., studied the adsorption of methylene blue using an Fe_3O_4/bentonite nanocomposite. Their research showed that the adsorption capacity improved with longer contact time and initial pH, but decreased with adsorbent mass. The adsorbent followed the Langmuir model well, reaching a maximal adsorption capacity of 1600 mg/g, making it a promising candidate for the removal of methylene blue in wastewater treatment.

In **2014**, **Lou et al**., studied the adsorption of methylene blue onto a bentonite magnetized with Fe_3O_4 nanoparticles. The method used is rapid and economical. The results show that adsorption follows a pseudo-second-order model, reaching equilibrium in 20 minutes. The adsorbent has a high adsorption capacity and can be easily regenerated by gamma irradiation, making it promising for the treatment of colored wastewater.

In **2015**, **Benhouria et al**., evaluated the effectiveness of three types of adsorbent materials for removing methylene blue from aqueous solutions: alginate-bentonite beads, alginate-activated carbon beads, and alginate-bentonite-activated carbon (ABA) beads. The results showed that the ABA beads had a maximal adsorption capacity of 756.97 mg/g at 30°C. Adsorption followed the pseudo-second-order kinetic model, indicating a chemisorption

process, and the equilibrium data were well fitted to the Freundlich model. ABA beads showed promise for the removal of cationic dyes.

In **2016**, **Belhouchat et al**., prepared a composite of activated organic bentonite (AOBent) and sodium alginate (SA) by intercalating the alginate into the bentonite and cross-linking the alginate with hydrochloric acid. This innovative, cost-effective material was tested for removing cationic and anionic dyes (methylene blue and methyl orange). The results showed that this composite is promising for removing these dyes, with easy use in environmentally-friendly treatment processes.

In **2016**, **Gomri et al**., studied the adsorption of the dye Acid Blue 80 (AB80) from aqueous solutions utilizing chemically changed bentonites. Bentonite in its raw state was transformed into sodium bentonite (NaB) and subsequently activated by acid treatment with sulphuric acid to produce a sample (ANaB) with altered adsorption characteristics. A study was conducted to evaluate the impact of carbon chain length on AB80 adsorption by substituting the NaB and ANaB samples with alkyl trimethylammonium bromides. The results showed that chemical modifications and carbon chain length significantly influence the adsorption efficiency of the dye.

In **2016**, **Djebri et al**., prepared composite beads of alginate and activated organoclay to remove m ethylene blue. The beads achieved a maximal adsorption capacity of 799.43 mg/g and show good performance in an endothermic and spontaneous process. They remain effective after several regeneration cycles, making them economical for wastewater treatment.

In **2016**, **Zhang et al**., prepared magnetic bentonite composites modified with γ-Fe_2O_3 nanoparticles. These composites, representing ferromagnetic characteristics, demonstrated a very high adsorption capacity for methylene blue, reaching a removal rate of 99.99%. The adsorption was studied and confirmed to be mainly electrostatic in nature.

In **2017**, **Nasrullah et al**., developed carbon-activated alginate beads for the removal of methylene blue. These beads exhibited a maximum adsorption capacity of 230 mg/g. Adsorption followed a pseudo-second-order pattern and fitted the Freundlich model well, indicating that these beads are both effective and economical for treating cationic dyes.

In **2018**, **Garmia et al**., explored the use of organo-bentonite/alginate composites in bead form for the removal of 2,4-dichlorophenol (2,4DCP) from aqueous solutions. Bentonite underwent modification using cationic surfactants, followed by encapsulation with calcium alginate to form composite adsorbent beads. This study demonstrated that the adsorption of

2,4DCP exhibited pseudo-second-order kinetics. The Langmuir isotherm model, suggesting the presence of homogenous monolayer adsorption, best matched the data. The composite beads showed a significant adsorption capacity, ranging from 142 to 391 mg/g, depending on the model.

In **2018**, **Aichour et al**., prepared low-cost biodegradable adsorbents from lemon peels activated with phosphoric acid (ALP) and encapsulated in alginate to form beads (ALP/A). These materials were characterized by FTIR, SEM and pHpzc. They were tested for the removal of methylene blue (MB) in aqueous solutions. The results showed a very high maximum adsorption capacity of 841.1 mg/g at 24°C. Removal efficiency was maintained at 80.5% and 70% after six adsorption-desorption cycles, using HCl solution or water respectively as desorption agents.

In **2018**, **Boukhalfa et al**., synthesized magnetic alginate beads, with and without functionalized carbon nanotubes, for methylene blue adsorption. The functionalized beads showed improved adsorption capacity and high stability over a wide pH range. They fitted the Freundlich model well and showed good reusability, making them suitable for large-scale use.

In **2019**, **Alvarez-Torrellas et al**., studied the adsorption of methylene blue (MB) on novel adsorbent beads composed of alginate (A), maghemite nanoparticles (γ-Fe_2O_3) and functionalized multiwall carbon nanotubes (f-CNTs). The time required to reach adsorption equilibrium was estimated at 48 hours. The results revealed that adsorption is spontaneous and endothermic. The A/γ-Fe_2O_3/f-CNT composites showed stable performance after at least six cycles of use and be easily separated from water thanks to their magnetic property.

In **2019**, **Aichour et al**., studied the adsorption of methylene blue (MB) dye on unmodified citrus peels (UCP) and citrus peels encapsulated with calcium alginate (UCP/A). The results showed that the encapsulated peels had a significantly higher adsorption capacity for removing the dye from wastewater. The encapsulated citrus peels showed a significantly higher adsorption capacity compared with non-encapsulated peels.

In **2019**, **Ravi et al**., developed an alginate bead system encapsulating bentonite for efficient removal of methylene blue. The synthesized beads exhibited high adsorption capacity and were characterized by various techniques. Adsorption was spontaneous and exothermic, combining surface adsorption and intra-particle diffusion. The system maintained a high removal efficiency after several cycles of use, offering a recyclable and effective solution for treating contaminants.

In **2020**, **Baouch et al**., studied the structural evolution of bentonites modified with different bromide fillers for dye adsorption. They evaluated the adsorption efficiency of methylene blue, red Bezathren and blue Telon on these modified clays using batch experiments. Equilibrium data were analyzed using Langmuir and Freundlich isotherm models, with the Langmuir isotherm model proving to be the most suitable. The maximum adsorption capacities calculated according to Langmuir increased with the addition of surfactant, and the adsorption process was judged endothermic in all cases.

In **2020**, **Aichour et al**., developed a hybrid composite based on activated bentonite and alginate for the adsorption of textile dyes such as methylene blue and crystal violet. The composite showed a high adsorption capacity and homogeneous adsorption. It also demonstrated good regeneration capacity, making it a promising candidate for wastewater treatment.

In **2021**, **Shikuku et al**., studied Kaolinite clay modified with magnetic magnetite nanoparticles (Fe_3O_4@MC) to improve its methylene blue (MB) adsorption capacity from synthetic wastewater. The modification was carried out by co-precipitation with ferrous and ferric ions. The results showed that MB adsorption on unmodified clay was best described by the Fowler-Guggenheim isotherm, while adsorption on Fe_3O_4@MC was better represented by the Freundlich model. The rise in BET specific surface area led to an improvement in the maximum adsorption capacity, both theoretically and experimentally.

In **2021**, **Is et al**., synthesized magnetic nanocomposites based on montmorillonite and iron oxide using a hydrothermal method. These nanocomposites showed good copper adsorption capacity and easy separation due to their magnetic properties. The adsorption followed a pseudo-second-order kinetic model and was well described by the Langmuir model. The nanocomposites also demonstrated chemical stability after several cycles of use.

In **2022**, **Daas et al**., studied the adsorption of methylene blue (MB) onto organophilic clay modified with a neutral amine and a silica source, creating materials called PCHs. The adsorbents prepared showed a high affinity for MB, with maximal adsorption capacities of 274 and 361 mg/g. Langmuir and Freundlich models were used to analyze the experimental data, and the adsorption mechanism was attributed to hydrophobic-hydrophobic interactions. These results are significant for the selection of the most effective materials for water treatment.

In **2022**, **Sun et al**., studied the removal of methylene blue (MB) from water using a composite of sodium alginate and bentonite (Ben). The bentonite was encapsulated in cobalt alginate (CA) displacement reaction with cobalt chloride, and the composite was prepared as CA/Ben aerogel by freeze-drying. The CA/Ben aerogel showed an adsorption capacity of 258.92 mg/g for MB. This material is recyclable, environmentally friendly and easy to prepare, making it promising for large-scale application in water treatment to remove dyes.

In **2023**, **Belbel et al**., examined the adsorption of methylene blue (MB) using bentonite modified with two surfactants: hexadecyl(trimethyl)azanium bromide (CTAB) and 1-butyl-3-methylimidazolium chloride (BMIMCI). The maximum adsorption capacities were 47.186 mg/g for CTAB-modified bentonite and 42.28 mg/g for BMIMCI-modified bentonite, according to the Langmuir model. The study showed that modified Algerian bentonite could effectively remove methylene blue from aqueous solutions.

In **2023**, **Ibrahim et al**., studied the removal of methylene blue from aqueous solutions using Iraqi bentonite clay and the UV-Vis technique. Their research showed that this bentonite enables effective removal of the dye, achieving an adsorption efficiency of up to 99.39% at 25°C. This study proposes the use of bentonite clay as a practical, economical and effective technology for treating wastewater.

In **2023**, **Abutaleb et al**., studied the decontamination of water contaminated by methylene blue using a nanocomposite based on Fe_3O_4, multiwall carbon nanotubes (MWCNTs) and bentonite. This nanocomposite, characterized by a high specific surface area of 204.01 m2/g, showed an adsorption capacity of 48.2 mg/g according to the Redlich-Peterson model. The kinetic data corresponded to the pseudo-first-order and pseudo-second-order models. Adsorption was determined to be non-spontaneous and endothermic, indicating that this nanocomposite is promising for water treatment.

In **2024**, **Chaabna et al**., developed a new magnetic composite material for the removal of methylene blue (MB) from water. This composite, prepared chemically from bentonite and iron salts, showed a high adsorption capacity of 82.2 mg/g and a MB removal efficiency of 100%. The results indicate that magnetic bentonite is an effective and practical solution for decontaminating water by adsorption.

In **2024**, **Hamad et al**., synthesized and characterized activated bentonite clay (ABC) adsorbents for the efficient removal of methylene blue (MB) from aqueous solutions. Activated with 16 M sodium hydroxide, these adsorbents showed an impressive adsorption

capacity of 22,131 mg/g. This research represents a major advance in water treatment, proposing an innovative method for the elimination of MB and contributing to the development of sustainable solutions for water treatment.

In **2024**, **Azriel et al**., examined the use of natural bentonite to remove dyes from textile wastewater. The results showed a maximum dye removal efficiency of 91.25% with an initial concentration of 10%, an adsorbent weight of 20 g, and a contact time of 60 minutes. They noted that a longer contact time increased removal efficiency and adsorption capacity, while a higher quantity of adsorbent reduced the concentration of dyes in the wastewater. This treatment considerably improved water quality, meeting environmental standards and regulations.

In **2024**, **Mohd Nizam et al**., studied the use of a bentonite-based magnetic composite for removing dyes from textile effluents. The results showed that the composite had a saturation magnetization of 9.2 emu/g and a high crystalline structure. In adsorption tests, the composite removed 100% of methylene blue (MB) from aqueous solutions with maximum capacity, confirming the composite's effectiveness and ecological potential for removing dyes from water.

References

[1]   T. Handayani, Emriadi, Deswati, P. Ramadhani, R. Zein, Modelling studies of methylene blue dye removal using activated corn husk waste: Isotherm, kinetic and thermodynamic evaluation, South African J. Chem. Eng. 47 (2024) 15–27. https://doi.org/10.1016/j.sajce.2023.10.003.

[2]   X. Yu, J. Zuo, X. Tang, R. Li, Z. Li, F. Zhang, Toxicity evaluation of pharmaceutical wastewaters using the alga Scenedesmus obliquus and the bacterium Vibrio fischeri, J. Hazard. Mater. 266 (2014) 68–74. https://doi.org/10.1016/j.jhazmat.2013.12.012.

[3]   G.E. Amaku, N.P. Akani, Physicochemical properties of the effluents of Forcados Terminal in Warri, Delta State, J. Environ. Chem. Ecotoxicol. 8 (2016) 9–13. https://doi.org/10.5897/jece2015.0368.

[4]   M.J. M-Ridha, S.I. Hussein, Z.T. Alismaeel, M.A. Atiya, G.M. Aziz, Biodegradation of reactive dyes by some bacteria using response surface methodology as an optimization technique, Alexandria Eng. J. 59 (2020) 3551–3563. https://doi.org/10.1016/j.aej.2020.06.001.

[5]   R. Shokoohi, D. Nematollahi, M.R. Samarghandi, G. Azarian, Z. Latifi, Optimization of three-dimensional electrochemical process for degradation of methylene blue from aqueous environments using central composite design, Environ. Technol. Innov. 18 (2020) 100711. https://doi.org/10.1016/j.eti.2020.100711.

[6]   N. Belhouchat, H. Zaghouane-boudiaf, C. Viseras, Applied Clay Science Removal of anionic and cationic dyes from aqueous solution with activated organo-bentonite / sodium alginate encapsulated beads, Appl. Clay Sci. (2016). https://doi.org/10.1016/j.clay.2016.08.031.

[7]   X. Zou, H. Zhang, T. Chen, H. Li, C. Meng, Y. Xia, J. Guo, Preparation and characterization of polyacrylamide / sodium alginate microspheres and its adsorption of MB dye, Colloids Surfaces A Physicochem. Eng. Asp. 567 (2019) 184–192. https://doi.org/10.1016/j.colsurfa.2018.12.019.

[8]   D. Tassalit, A.N. Laoufi, F. Bentahar, Photocatalytic deterioration of tylosin in an aqueous suspension using UV/TiO 2, Sci. Adv. Mater. 3 (2011) 944–948. https://doi.org/10.1166/sam.2011.1243.

[9]   N. HADJ SALAH, Etude de la dégradation photocatalytique de polluants organiques en présence de dioxyde de titane, en suspension aqueusz et en lit fixe, (2012) 169.

[10]   T. Edition, WHO guidelines for drinking water quality, Vol. 1. Recommendations,

Environ. Pollut. Ser. A, Ecol. Biol. 37 (1985) 282. https://doi.org/10.1016/0143-1471(85)90051-0.

[11] J.B. Kowalska, R. Mazurek, M. Gąsiorek, T. Zaleski, Pollution indices as useful tools for the comprehensive evaluation of the degree of soil contamination–A review, Environ. Geochem. Health 40 (2018) 2395–2420. https://doi.org/10.1007/s10653-018-0106-z.

[12] S.P. Lamah, O. Traore, N. Dore, Impacts environnementaux de l'utilisation irrationnelle des pesticides dans les villages riverains du site du patrimoine mondial de l'UNESCO, Réserve de Biosphère des Monts Nimba-République de Guinée, 23 (2023) 69–80.

[13] H. Freeman, T. Harten, J. Springer, P. Randall, M.A. Curran, K. Stone, Industrial pollution prevention: A critical review, J. Air Waste Manag. Assoc. 42 (1992) 618–656. https://doi.org/10.1080/10473289.1992.10467016.

[14] D.J. Lapworth, D.C.W. Nkhuwa, J. Okotto-Okotto, S. Pedley, M.E. Stuart, M.N. Tijani, J. Wright, Qualité des eaux souterraines urbaines en Afrique sub-saharienne: état actuel et implications pour la sécurité de l'approvisionnement en eau et la santé publique, Hydrogeol. J. 25 (2017) 1093–1116. https://doi.org/10.1007/s10040-016-1516-6.

[15] B. Barrett, J.W. Charles, J.L. Temte, Climate change, human health, and epidemiological transition, Prev. Med. (Baltim). 70 (2015) 69–75. https://doi.org/10.1016/j.ypmed.2014.11.013.

[16] A.V. Jung, P. Le Cann, B. Roig, O. Thomas, E. Baurès, M.F. Thomas, Microbial contamination detection in water resources: Interest of current optical methods, trends and needs in the context of climate change, Int. J. Environ. Res. Public Health 11 (2014) 4292–4310. https://doi.org/10.3390/ijerph110404292.

[17] G. Mougeot, Infections à protozoaires et environnement, Rev. Fr. Des Lab. 2001 (2001) 25–31. https://doi.org/10.1016/S0338-9898(01)80386-3.

[18] M. Koivusalo, T. Vartiainen, Drinking water chlorination by-products and cancer, Rev. Environ. Health 12 (1997) 81–90. https://doi.org/10.1515/REVEH.1997.12.2.81.

[19] M. Jaishankar, T. Tseten, N. Anbalagan, B.B. Mathew, K.N. Beeregowda, Toxicity, mechanism and health effects of some heavy metals, Interdiscip. Toxicol. 7 (2014) 60–72. https://doi.org/10.2478/intox-2014-0009.

[20] P.B. Tchounwou, C.G. Yedjou, A.K. Patlolla, D.J. Sutton, Molecular, clinical and environmental toxicicology Volume 3: Environmental Toxicology, 2012.

https://doi.org/10.1007/978-3-7643-8340-4.

[21] D.E.L. Industriels, Chapitre 05: Les normes de rejets industriels (réglementations algérienne et européenne) I-Réglementation algérienne: la réglementation en vigueur est mise en place par l'application des articles émis dans le journal officiel ci-dessous:, (2006).

[22] A. Ahmad, M. Ahmad, Deciphering the toxic effects of organochlorine pesticide, dicofol on human RBCs and lymphocytes, Pestic. Biochem. Physiol. 143 (2017) 127–134. https://doi.org/10.1016/j.pestbp.2017.08.007.

[23] M. Tudi, H.D. Ruan, L. Wang, J. Lyu, R. Sadler, D. Connell, C. Chu, D.T. Phung, Agriculture development, pesticide application and its impact on the environment, Int. J. Environ. Res. Public Health 18 (2021) 1–24. https://doi.org/10.3390/ijerph18031112.

[24] H.D. Burrows, M. Canle L, J.A. Santaballa, S. Steenken, Reaction pathways and mechanisms of photodegradation of pesticides, J. Photochem. Photobiol. B Biol. 67 (2002) 71–108. https://doi.org/10.1016/S1011-1344(02)00277-4.

[25] C. Infante-Rivard, S. Weichenthal, Pesticides and childhood cancer: An update of Zahm and Ward's 1998 review, J. Toxicol. Environ. Heal. - Part B Crit. Rev. 10 (2006) 81–99. https://doi.org/10.1080/10937400601034589.

[26] I.K. Konstantinou, T.A. Albanis, Photocatalytic transformation of pesticides in aqueous titanium dioxide suspensions using artificial and solar light: Intermediates and degradation pathways, Appl. Catal. B Environ. 42 (2003) 319–335. https://doi.org/10.1016/S0926-3373(02)00266-7.

[27] M. Clara, N. Kreuzinger, B. Strenn, O. Gans, H. Kroiss, The solids retention time - A suitable design parameter to evaluate the capacity of wastewater treatment plants to remove micropollutants, Water Res. 39 (2005) 97–106. https://doi.org/10.1016/j.watres.2004.08.036.

[28] H.Y. Shu, M.C. Chang, Decolorization effects of six azo dyes by O3, UV/O3 and UV/H2O2 processes, Dye. Pigment. 65 (2005) 25–31. https://doi.org/10.1016/j.dyepig.2004.06.014.

[29] U. Pagga, D. Brown, The degradation of dyestuffs: Part II Behaviour of dyestuffs in aerobic biodegradation tests, Chemosphere 15 (1986) 479–491. https://doi.org/10.1016/0045-6535(86)90542-4.

[30] E.R. Nestmann, G.R. Douglas, T.I. Matula, C.E. Grant, D.J. Kowbel, Mutagenic Activity of Rhodamine Dyes and Their Impurities as Detected by Mutation Induction in Salmonella and DNA Damage in Chinese Hamster Ovary Cells, Cancer Res. 39

(1979) 4412–4417.

[31] B. Boutra, M. Trari, N. Nassrallah, B. Bellal, Adsorption and Photodegradation of Solophenyl Red 3BL on Nanosized ZnFe2O4 Under Solar Light, Theor. Exp. Chem. 52 (2016) 303–309. https://doi.org/10.1007/s11237-016-9482-6.

[32] D.A. Yaseen, M. Scholz, Textile dye wastewater characteristics and constituents of synthetic effluents: a critical review, Springer Berlin Heidelberg, 2019. https://doi.org/10.1007/s13762-018-2130-z.

[33] G. Samchetshabam, Hussan Ajmal, Choudhury. T. G., Impact of textile dyes waste on aquatic environments and its treatment. Environ. Ecol, 35(3C), pp.2349-2353., Environ. Ecol. 35 (2017) 2349-2353.

[34] T. Randrianantoandro, R. Rakotobe, H. Razafimandimby, Etude des répercussions de la pollution industrielle sur la riziculture dans la plaine de Laniera à Antananarivo , Madagascar Résumé, Afrique Sci. 10 (2014) 45–60.

[35] R. Gandhimathi, N.J. Durai, P.V. Nidheesh, S.T. Ramesh, S. Kanmani, Use of combined coagulation-adsorption process as pretreatment of landfill leachate, Iran. J. Environ. Heal. Sci. Eng. 10 (2013) 1–7. https://doi.org/10.1186/1735-2746-10-24.

[36] Z.A. Hussain, F.H. Fakhri, H.F. Alesary, L.M. Ahmed, ZnO Based Material as Photocatalyst for Treating the Textile Anthraquinone Derivative Dye (Dispersive Blue 26 Dye): Removal and Photocatalytic Treatment, J. Phys. Conf. Ser. 1664 (2020). https://doi.org/10.1088/1742-6596/1664/1/012064.

[37] A. De Boom, M. Degrez, Etat de l'art des traitements des résidus d'épuration des fumées d'incinération d'ordures ménagères (REFIOM), Environnement, Ingénierie & Développement N°47-... (2007) 4–11. https://doi.org/10.4267/dechets-sciences-techniques.1624.

[38] L. Bertin, M.C. Colao, M. Ruzzi, L. Marchetti, F. Fava, Performances and microbial features of an aerobic packed-bed biofilm reactor developed to post-treat an olive mill effluent from an anaerobic GAC reactor, Microb. Cell Fact. 5 (2006) 1–11. https://doi.org/10.1186/1475-2859-5-16.

[39] L. Kolář, M. Maršálek, J. Frelich, S. Kužel, P. Smetana, J. Zedníková, M. Švecová, Changes in methane release from organic matter passing through the digestive tract of horses, Czech J. Anim. Sci. 54 (2009) 112–120. https://doi.org/10.17221/1677-cjas.

[40] R.M. Jingura, R. Matengaifa, Optimization of biogas production by anaerobic digestion for sustainable energy development in Zimbabwe, Renew. Sustain. Energy Rev. 13 (2009) 1116–1120. https://doi.org/10.1016/j.rser.2007.06.015.

[41] P. Parthasarathy, S.K. Narayanan, Effect of Hydrothermal Carbonization Reaction Parameters on, Environ. Prog. Sustain. Energy 33 (2014) 676–680. https://doi.org/10.1002/ep.

[42] C. Andriantsiferana, E.F. Mohamed, H. Delmas, Sequential adsorption - Photocatalytic oxidation process for wastewater treatment using a composite material TiO2/activated carbon, Environ. Eng. Res. 20 (2015) 181–189. https://doi.org/10.4491/eer.2014.070.

[43] R. Molinari, M. Borgese, E. Drioli, L. Palmisano, M. Schiavello, Hybrid processes coupling photocatalysis and membranes for degradation of organic pollutants in water, Catal. Today 75 (2002) 77–85. https://doi.org/10.1016/S0920-5861(02)00047-0.

[44] S. Popli, U.D. Patel, Destruction of azo dyes by anaerobic–aerobic sequential biological treatment: a review, Int. J. Environ. Sci. Technol. 12 (2015) 405–420. https://doi.org/10.1007/s13762-014-0499-x.

[45] S. Kuppusamy, K. Venkateswarlu, P. Thavamani, Y.B. Lee, R. Naidu, M. Megharaj, Quercus robur acorn peel as a novel coagulating adsorbent for cationic dye removal from aquatic ecosystems, Ecol. Eng. 101 (2017) 3–8. https://doi.org/10.1016/j.ecoleng.2017.01.014.

[46] A. Oun, N. Tahri, S. Mahouche-Chergui, B. Carbonnier, S. Majumdar, S. Sarkar, G.C. Sahoo, R. Ben Amar, Tubular ultrafiltration ceramic membrane based on titania nanoparticles immobilized on macroporous clay-alumina support: Elaboration, characterization and application to dye removal, Sep. Purif. Technol. 188 (2017) 126–133. https://doi.org/10.1016/j.seppur.2017.07.005.

[47] R.J. Davis, J.L. Gainer, G. O'Neal, I. Wu, Photocatalytic decolorization of wastewater dyes, Water Environ. Res. 66 (1994) 50–53. https://doi.org/10.2175/wer.66.1.8.

[48] A. Belghit, S. Merouani, O. Hamdaoui, A. Alghyamah, M. Bouhelassa, Influence of processing conditions on the synergism between UV irradiation and chlorine toward the degradation of refractory organic pollutants in UV/chlorine advanced oxidation system, Sci. Total Environ. 736 (2020) 139623. https://doi.org/10.1016/j.scitotenv.2020.139623.

[49] X. Hao, H. Liu, G. Zhang, H. Zou, Y. Zhang, M. Zhou, Y. Gu, Applied Clay Science Magnetic fi eld assisted adsorption of methyl blue onto organo-bentonite, Appl. Clay Sci. 55 (2012) 177–180. https://doi.org/10.1016/j.clay.2011.11.019.

[50] E. Chatzisymeon, N.P. Xekoukoulotakis, A. Coz, N. Kalogerakis, D. Mantzavinos, Electrochemical treatment of textile dyes and dyehouse effluents, J. Hazard. Mater. 137 (2006) 998–1007. https://doi.org/10.1016/j.jhazmat.2006.03.032.

[51] J. Zhang, D. Cai, G. Zhang, C. Cai, C. Zhang, G. Qiu, K. Zheng, Z. Wu, Adsorption of methylene blue from aqueous solution onto multiporous palygorskite modified by ion beam bombardment: Effect of contact time, temperature, pH and ionic strength, Appl. Clay Sci. 83–84 (2013) 137–143. https://doi.org/10.1016/j.clay.2013.08.033.

[52] M. Xia, Z. Chen, Y. Li, C. Li, N.M. Ahmad, W.A. Cheema, S. Zhu, Removal of Hg(ii) in aqueous solutions through physical and chemical adsorption principles, RSC Adv. 9 (2019) 20941–20953. https://doi.org/10.1039/c9ra01924c.

[53] C.H. Weng, Y.T. Lin, T.W. Tzeng, Removal of methylene blue from aqueous solution by adsorption onto pineapple leaf powder, J. Hazard. Mater. 170 (2009) 417–424. https://doi.org/10.1016/j.jhazmat.2009.04.080.

[54] A. Öztürk, E. Malkoc, Adsorptive potential of cationic Basic Yellow 2 (BY2) dye onto natural untreated clay (NUC) from aqueous phase: Mass transfer analysis, kinetic and equilibrium profile, Appl. Surf. Sci. 299 (2014) 105–115. https://doi.org/10.1016/j.apsusc.2014.01.193.

[55] A. V. Kiselev, Adsorption properties of hydrophobic surfaces, J. Colloid Interface Sci. 28 (1968) 430–442. https://doi.org/10.1016/0021-9797(68)90074-X.

[56] M. Belghazdis, E.-K. Hachem, Clay and Clay Minerals: A Detailed Review, Int. J. Recent Technol. Appl. Sci. 4 (2022) 54–75. https://doi.org/10.36079/lamintang.ijortas-0402.367.

[57] L. Bouna, Fonctionnalisation des minéraux argileux d'origine marocaine par TiO2 en vue de l'élimination par photocatalyse de micropolluants organiques des milieux aqueux, Thèse de l'Université de Toulouse (France) (2012) 1–298.

[58] A.A. Azeez, K.Y. Rhee, S.J. Park, D. Hui, Epoxy clay nanocomposites - Processing, properties and applications: A review, Compos. Part B Eng. 45 (2013) 308–320. https://doi.org/10.1016/j.compositesb.2012.04.012.

[59] G. Lagaly, <Solidsi22-43.Pdf>, 22 (1986) 43–51.

[60] V. Rocher, Synthèse et caractérisation de billes d'alginate magnétiques pour l'élimination de polluants organiques dans les effluents par séparation magnétique, Thése Dr. (2008) 270.

[61] B.H.A. Rehm, Alginates: Biology and Applications: Biology and Applications, 2015.

[62] S.N. Pawar, K.J. Edgar, Alginate derivatization: A review of chemistry, properties and applications, Biomaterials 33 (2012) 3279–3305. https://doi.org/10.1016/j.biomaterials.2012.01.007.

[63] G.T. Grant, E.R. Morris, D.A. Rees, P.J.C. Smith, D. Thom, Biological interactions

between polysaccharides and divalent cations: The egg-box model, FEBS Lett. 32 (1973) 195–198. https://doi.org/10.1016/0014-5793(73)80770-7.

[64] K. Kashima, M. Imai, Impact factors to regulate mass transfer characteristics of stable alginate membrane performed superior sensitivity on various organic chemicals, Procedia Eng. 42 (2012) 964–977. https://doi.org/10.1016/j.proeng.2012.07.490.

[65] G. Fatima, Etude des interfaces solide-liquide : Application à l'adsorption des micropolluants, Thése Dr. En Génie Chim. Univ. SETIF-1 (2017) 1–183.

[66] R.D. Ambashta, M. Sillanpää, Water purification using magnetic assistance: A review, J. Hazard. Mater. 180 (2010) 38–49. https://doi.org/10.1016/j.jhazmat.2010.04.105.

[67] G. Moffat, R.A. Williams, C. Webb, R. Stirling, Selective separations in environmental and industrial processes using magnetic carrier technology, Miner. Eng. 7 (1994) 1039–1056. https://doi.org/10.1016/0892-6875(94)90032-9.

[68] C. de Latour, Magnetic Separation in Water Pollution Control, IEEE Trans. Magn. 9 (1973) 314–316. https://doi.org/10.1109/TMAG.1973.1067685.

[69] V. Rocher, A. Bee, J.M. Siaugue, V. Cabuil, Dye removal from aqueous solution by magnetic alginate beads crosslinked with epichlorohydrin, J. Hazard. Mater. 178 (2010) 434–439. https://doi.org/10.1016/j.jhazmat.2010.01.100.

[70] Z. Yang, H. Peng, W. Wang, T. Liu, Crystallization behavior of poly(ε-caprolactone)/layered double hydroxide nanocomposites, J. Appl. Polym. Sci. 116 (2010) 2658–2667. https://doi.org/10.1002/app.

[71] L. Obeid, A. Bée, D. Talbot, S. Ben Jaafar, V. Dupuis, S. Abramson, V. Cabuil, M. Welschbillig, Chitosan/maghemite composite: A magsorbent for the adsorption of methyl orange, J. Colloid Interface Sci. 410 (2013) 52–58. https://doi.org/10.1016/j.jcis.2013.07.057.

[72] A. Bée, D. Talbot, S. Abramson, V. Dupuis, Magnetic alginate beads for Pb(II) ions removal from wastewater, J. Colloid Interface Sci. 362 (2011) 486–492. https://doi.org/10.1016/j.jcis.2011.06.036.

[73] A.F. Ngomsik, A. Bee, J.M. Siaugue, V. Cabuil, G. Cote, Nickel adsorption by magnetic alginate microcapsules containing an extractant, Water Res. 40 (2006) 1848–1856. https://doi.org/10.1016/j.watres.2006.02.036.

[74] M.M. Lakouraj, F. Mojerlou, E.N. Zare, Nanogel and superparamagnetic nanocomposite based on sodium alginate for sorption of heavy metal ions, Carbohydr. Polym. 106 (2014) 34–41. https://doi.org/10.1016/j.carbpol.2014.01.092.

CHAPTER II
Materials and Methods

CHAPTER II
MATERIALS AND METHODS

II.1. Introduction

This chapter provides an overview of the reagents used in the study, the different synthesis procedures for the materials under investigation, the analytical methods employed to identify and comprehend the adsorbent materials, the experimental procedures used for the methylene blue adsorption experiments on the adsorbents in a batch system, and the modeling of the various systems examined.

II.2. Reagents and precursor material

As indicated in Table II.1, the reagents employed in this work are of analytical quality and were utilized without initial purification. Solutions were formulated using distilled water.

Table II.1: Chemical reagents used in this study.

Reagents	Chemical formula	Supplier	purity
Sodium hydroxide	$NaOH$	Sigma Aldrich	>99 %
Hydrochloric acid	HCl	Sigma Aldrich	37 %
Sodium alginate	$C_6H_7NaO_6$	Sigma Aldrich	>99 %
Methylene blue	$C_{16}H_{18}ClN_3S$	Sigma Aldrich	98 %
Calcium chloride dihydrate	$CaCl_2 \cdot 2\,H_2O$	Honeywell	>99 %
Iron (II) heptahydrate	$FeSO_4\text{-}7\,H_2O$	Biochem chemopharma	>99 %
Iron (III) hexahydrate	$FeCl_3\text{-}6\,H_2O$	Biochem chemopharma	>99 %
Hexadecyltrimethylammonium bromide	$C_{19}H_{42}BrN$	Sigma Life Science	≥98%

The clay used in this study is an Algerian bentonite from the Maghnia deposit in western Algeria. Its chemical composition is given in Table II.2.

Table II.2: Chemical analysis of the natural bentonite used (% by weight) [1].

Chemical composition	SiO$_2$	Al$_2$O$_3$	MgO	MnO	K$_2$O	CaO	Fe$_2$O$_3$	Na$_2$O	TiO$_2$	loss of ignition
%	56,8	18,5	3,7	0,03	1,4	0,5	2,9	1,6	0,1	13,6

II.3. The adsorbate used in this study

We were interested in a cationic dye, methylene blue, in this work. The choice was made on two bases: the strong presence of molecules in wastewater and the ease of their dosage in water.

II.3.1. Methylene blue

Methylene blue (MB) is the most commonly used cationic dye in different fields such as chemistry, medicine, dentistry and the dye industry for dyeing cotton, wood and paper [2].
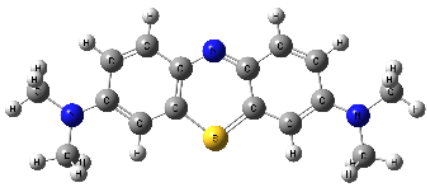
It is used as a model organic contaminant due to its molecular structure stable [3]. The use of this compound includes:

- A vital dye, it colours specific histological structures.
- It accelerates the reduction of methemoglobins.
- An antiseptic, an antirheumatic [4].
- An optical limiter combined with a polymer protects the eyes against intense lasers.

Toxicological data reveal that the use of methylene blue has no danger linked to using this product as medicine [5], as long as the dose does not exceed 7 mg/kg.

Methylene blue is not highly dangerous but still hurts living organisms through its long-term presence in water. It can cause chest pain, dyspnea, anxiety, tremors, hypertension, and even discolouration of the skin if the dose is too high (MB physical-chemical properties are shown in Table II.3.

Table II.3: Physical and chemical properties of methylene blue.

Properties	
Chemical name	Chloride tetramethyl thionine Blue Basic 9
Family	Basic colouring
Chemical structure	
Molecular weight (g/mol)	319.85
Chemical formula	$C_{16}H_{18}ClN_3S$
Solubility in water	40 g/L at T = 25°C
Melting point (°C)	180
pKa	3.8
λ max (nm)	664

II.4. Synthesis of bentonite-based magnetic materials

II.4.1. Purification of bentonite

Before synthesizing magnetic clay materials, it was necessary to purify the bentonite. To achieve this, 20 g of bentonite clay was thoroughly rinsed in 1000 ml of distilled water, subjected to centrifugation at 6000 rpm for 15 min, and then dried in an oven at 60 °C for 24 h and crushed into a uniform powder known as **Bent**.

II.4.2. Synthesis of organophilic bentonite

One form of organophilic treatment is the exchange of cations. In cationic clays, cations in the inter-foliar space have been replaced by cations with a long alkyl chain. Its carbon framework enhances the organophilic clay's attraction to organic compounds. Furthermore, since these cations are far more significant than the alkali ions initially present, they occupy more space and separate the sheets. The interfoliar space that can be accessed is more critical, and the electrostatic coupling between sheets diminishes [6].

The exchange capacity was saturated to 100 % of the CEC by alkyl ammoniums. Initial cations, particularly (H^+), were exchanged by surfactant cations.

For the exchange, we used Hexadecyltrimethylammonium bromide (HDTMAB) as alkyl ammonium: $C_{19}H_{42}NBr$ (denoted: C_{16}).

The assumed cation exchange capacity (CEC) for synthesizing organophilic bentonite is 120 meq/100 g. The protocol for intercalation is as follows: 8.34 mL of hydrochloric acid (HCl 1N) is added to an Erlenmeyer flask. This acid solution is heated to 80 °C with moderate stirring to prevent foaming. When the temperature stabilizes, 4.37 g of C16 is introduced for ionization. After 3 hours of stirring at 80°C, the alkyl ammonium salt dissolves and ionizes. Then, 10 g of bentonite is added. After 3 hours of cation exchange, the samples were washed several times with distilled water until all bromide ions were removed (confirmed by a negative silver nitrate test). The samples are then dried at 80°C in an oven for 24 hours, ground, and stored until use. The synthesized organophilic bentonite is referred to as **Bent-organo.**

II.4.3. Synthesis of magnetic bentonite and magnetic organophilic bentonite

This part of the project aims to develop a magnetic composite material capable of adsorbing pollutant organic molecules for magnetic separation. It is part of a drive to develop innovative effluent decontamination methods. The system consists of magnetic nanoparticles and purified bentonite (organophilic bentonite).

Magnetic bentonite (**MBent**) and magnetic organophilic bentonite (**MBent-organo**) were synthesized by the reverse coprecipitation method described in the literature [7–9]. Which requires the mixing until total dissolution of 30 mL $FeCl_3$-$6H_2O$ (8.106 g) and $FeSO_4$-7 H_2O (4.167 g); this mixture was added dropwise in a sodium hydroxide solution (40 mL, 3. 2 g) at 65 °C and kept under stirring for 30 min at pH =11 after washing with distilled water. Next, it was dispersed in 300 mL of water. Then, a quantity of 6 g of **Bent** (**Bent-organo**) was introduced into the solution containing the magnetic nanoparticles with a stirring speed of 450 rpm for 6 h; the results were separated by centrifugation and, after that, rinsed with water until a pH of 6 was achieved. The generated particles were desiccated in a 60°C oven, then ground and stored until used and absorbed.

II.5. Synthesis of composite beads

Based on the extrusion method, we successfully synthesized magnetic bentonite alginate beads (**MBent-A beads**) and magnetic organophilic bentonite alginate beads (**MBent-organo-A beads**). The process began by dissolving 2 g of sodium alginate in 100 mL of distilled water under continuous mechanical agitation for 3 hours, resulting in a homogeneous mixture. Subsequently, 2 g of **MBent** (**MBent-organo**) was incorporated into the mixture and agitated for 24 hours. The encapsulated material was then introduced dropwise into a 100 mL

solution of 4% $CaCl_2 \cdot 2H_2O$, which served as a cross-linking agent, leading to the instantaneous formation of beads, as noted in reference [10]. The bead mixture was left under agitation overnight and washed with distilled water to neutralize the pH to 7. Post-washing, the beads were dried at room temperature, resulting in the observed size reduction. This methodology proved effective for bead synthesis, with the drying step inducing irreversible structural changes that inhibit the beads from re-swelling to their pre-dried size upon rehydration. Figure II.1 shows a schematic illustration of Magnetic Alginate Beads Synthesis pathway.
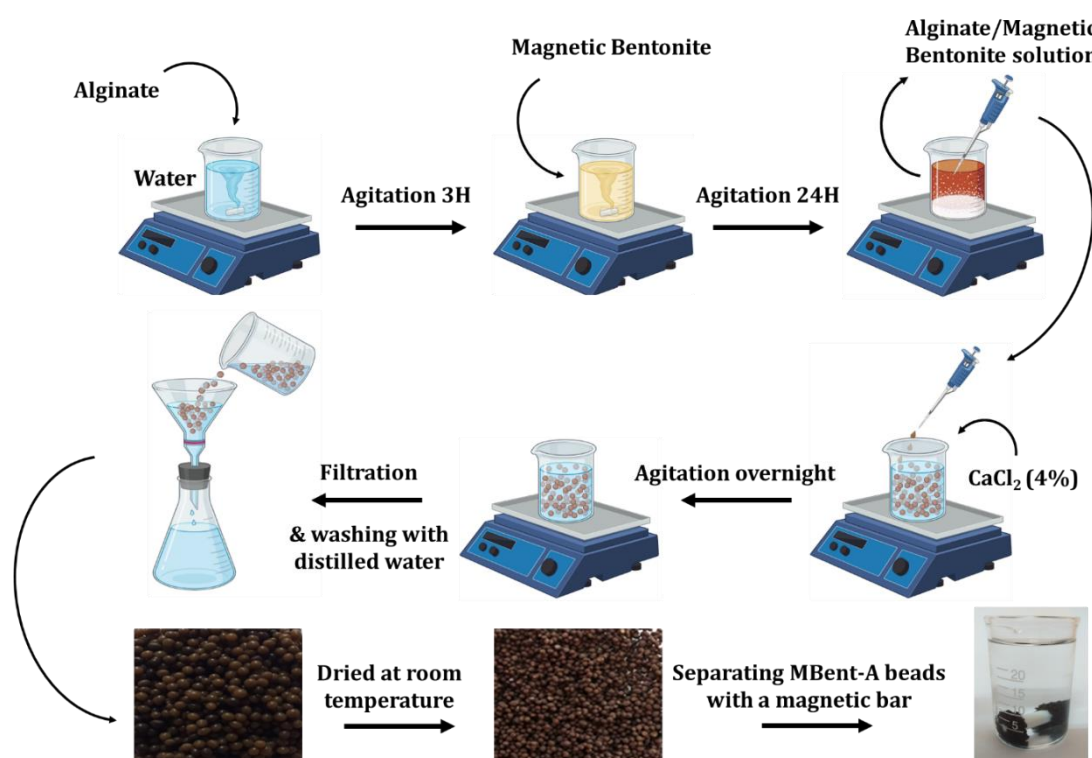
Figure II.1. Schematic illustration of Magnetic Alginate Beads Synthesis pathway.

II.6. Characterization techniques

Several characterization techniques, described in more detail below, were used in this work.

II.6.1. Fourier-transform infrared spectroscopy (FTIR)

Fourier transform infrared (FTIR) spectroscopy is a method of analysis dependent on the absorption of infrared radiation by the sample under analysis. Detecting the characteristic vibrations of chemical bonds between two atoms enables the analysis of chemical functions.

Each chemical function has a specific vibrational wavelength value, which depends on the nature of the chemical elements, their intramolecular arrangement, and their intermolecular interaction.

Suppose the energy of the incident beam (i.e., its wavelength) is close to the vibrational energy of the molecule. In that case, the latter will absorb the radiation, and we can then measure the decrease in intensity, reflected or transmitted. The infrared range extends from 4,000 to 400 cm^{-1} and corresponds to the energy range of molecule vibrations.

Not all vibrations give rise to absorption, as this also depends on the molecule's geometry, particularly its symmetry. For a given geometry, group theory can be used to determine which vibration modes are active in the infrared.

Functional groups of studied and synthesized materials were examined by FTIR apparatus type spectrophotometer Shimadzu-8400 Japan, considering the KBr disc method in the 400–4000 cm^{-1} (Ferhat Abbas Setif 1 University, Algeria).

II.6.2. X-ray diffraction (**XRD**)

X-ray diffraction (XRD) is a structural analysis technique used to identify the structure and purity of crystallized materials. Finely ground solid samples are mounted on suitable sample holders and then subjected to a monochromatic X-ray beam CuKα (λ = 0,1545 nm) to be diffracted by the reticular planes of the crystalline phase.

The crystalline structure was analyzed using a Bruker D8 Advance diffractometer. The XRD patterns were acquired for 2Θ angles ranging from 4 to 70∘, with 0.03∘ steps (University of Strasbourg, France).

II.6.3. Scanning electron microscopy (SEM)/energy-dispersive X-ray spectroscopy (EDS)

Scanning electron microscopy (SEM) is an innovative image analysis method that delivers high-resolution images of the surface of a sample by examining the interaction between electrons and the material. This method enables in-depth analysis of the adsorbent's surface characteristics, including its morphology, texture, and pore structure [11,12], and provides information on its chemical composition. The morphology and chemical composition of adsorbents can also be studied using energy-dispersive X-ray spectroscopy (EDS). Understanding these surface characteristics is crucial to elucidating the adsorption process and examining the interactions between adsorbent and adsorbate.

In this investigation, scanning electron microscopy (SEM) examinations were carried out using an EDS spectrometer/SEM scanning electron microscope JEOL-JSM-7001 (Ferhat Abbas Setif 1 University, Algeria).

II.6.4. Point of zero charge (pHpzc)

The pHpzc, also known as the zero point of charge pH, is the specific pH value at which the total charge on the surface of the adsorbent molecules equals zero. This coefficient is essential for comprehending adsorption processes, especially in electrostatic forces [13].

A simple and efficient technique may be employed to calculate the pHpzc: A volume of 20 mL of purified water is introduced into Erlenmeyer flasks that hold 20 mg of the adsorbent targeted for characterization. Adjustments are made to the pH of each suspension by adding NaOH or HCl solutions (0.1 M) within the range of 2 to 12. The suspensions are then subjected to agitation at ambient temperature for 24 hours for powder adsorbents and 48 hours for bead-type adsorbents. A final pH is then determined [14].

The data is graphed using the equation $\Delta pH = pH\_final - pH\_initial$ vs $pH\_initial$. The point at which the curve intersects with the axis traveling through zero describes the isoelectric point. pH_{PZC} is a good indicator of functional groups' chemical and electronic properties [15].

II.7. Dosage of solutions

II.7.1. Dosage Methods

The various concentrations of the solutions used and the equilibrium concentrations were determined by analysis using a UV-visible spectrophotometer (Shimadzu Spectrophotometer UV/Vis 1800) at maximum wavelength. (λmax) for methylene blue of 664 nm at natural pH. This allows direct measurement of the optical densities of each solution, giving access to the different concentrations using Beer-Lambert's law, which shows a proportional relationship between absorbance and the concentration of the solution to be analyzed.

- **Beer-Lambert's law**

The proportion of light incident through a transparent medium is independent of the intensity of the light. Lambert's law is expressed by Eq. (1):

$$T = \frac{I}{I_0} \tag{1}$$

Where:

- I_0, intensity of incident light;
- I, intensity of transmitted light (I always less than I_0);
- T, transmittance, often expressed in %.

Moreover, according to Beer, light adsorption is directly proportional to the concentration of the medium. Combining these two laws gives the relationship between absorbance A (or optical density) and transmittance T Eq. (2).

$$A = \log\frac{I}{I_0} = -\log T = \varepsilon l c \tag{2}$$

Where:

- A is the absorbance (unitless);

- ε is the molar extinction adsorption coefficient (dm^3/Mole. Cm);

- l is the length of the cell or light path (cm);

- c is the molar concentration of adsorbing species (mol/dm^3).

II.7.2. Preparing the calibration solution

To plot the methylene blue calibration curve, we have prepared a concentrated stock solution (10 mg/L) from which we prepare a series of known concentrations of 1 to 9 mg/L (by successive dilutions) at solution pH. These will be analyzed by UV-visible spectroscopy, which gives the variation in OD as a function of concentration C_0 (mg/L) of the aqueous methylene blue solutions. We plot the variation in optical density as a function of concentration on the calibration curve. We obtain a straight line with a correlation coefficient greater than 0.999. This line, which obeys Beer-Lambert's law, will be used to determine the unknown concentrations of the solutions after adsorption. The calibration curve is shown in Figure II.2.
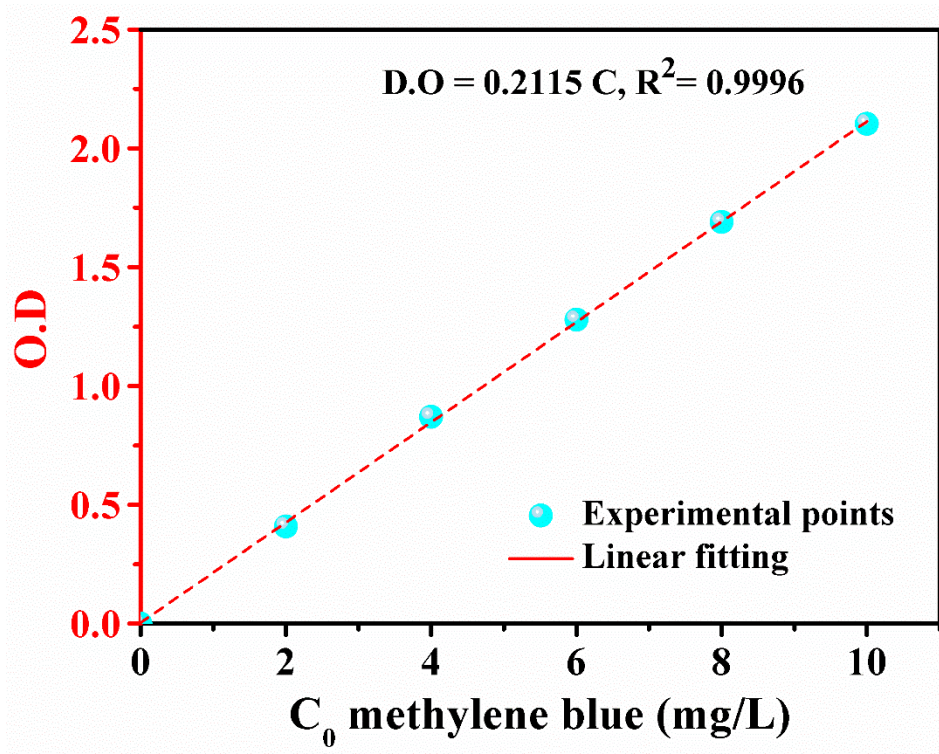
Figure II.2. Methylene Blue calibration curves at solution pH.

II.8. Adsorption study

Several parameters were found affecting the adsorption process, such as medium pH value, the dosage of adsorbent, adsorbate concentration, temperature, and even structural properties of the adsorbent [16]. Hence, all required experiments were performed to investigate our material adsorption behavior.

Based on Eqs. (3−5), evaluations of the absorbed quantity of MB dye Q_t (mg/g) at time t (min), equilibrium Q_e (mg/g), and percentage removal (R %) were measured.

$$Q_t = \frac{(C_0 - C_t)\,V}{m} \tag{3}$$

$$Q_e = \frac{(C_0 - C_e)\,V}{m} \tag{4}$$

$$R\,(\%) = \frac{C_0 - C_e}{C_0} * 100 \tag{5}$$

Where:

- m is the weight of the adsorbent (g);

- *V* is the volume of the solution (mL);

- C_0, C_t, and C_e are the initial, any-time, and equilibrium concentrations (mg/L).

II.8.1. Effect of solution pH on adsorption

The adsorption capacity of an absorbent material is typically dependent on the pH value of the solution because of its essential effect on the degree of ionization and dissociation of the absorbate as well as surface charge characteristics [17]. Investigating the pH effect can help improve our understanding of the adsorption mechanism in this situation. Therefore, a fixed sample dosage of 20 mg, a constant initial concentration of MB of 200 mg/L, and a temperature of 25 °C were used to study the effect of initial pH on MB adsorption on powder and bead adsorbents from 2 to 12. The pH was adjusted with 0.1 M HCl or 0.1 M NaOH solutions.

II.8.2. Effect of adsorbent dose

The absorbent dosage effect was evaluated from 10 to 150 mg/L in solutions with pH 6.4. In these experiments, the masses of adsorbents with 20 mL of 200 mg/L of methylene blue were mixed at T = 25 °C and stirring speed = 250 rpm. After shaking, the adsorbed amount was measured (mg/g).

II.8.3. The effect of temperature and thermodynamic parameters

Increasing temperature is known to increase the diffusion rate of adsorbate molecules through the outer boundary layer and into the pores of the adsorbent particles due to the decrease in solution viscosity [18]. A change in temperature causes a change in the adsorbent's adsorption capacity by changing the adsorbate particles' energies [19].

The influence of temperature a was carried out at different temperatures:
15, 25, 30 and 40 °C for **MBent** and **MBent-A beads** adsorbents, and at 20, 30 and 40°C for **MBent-organo** and **MBent-organo-A beads** adsorbents separately in solutions with pH 6.4. In these experiments, 20 mg of **M-Bent (or MBent-A beads, MBent-organo and MBent-organo-A beads)** with 20 mL of 200 mg/L of methylene blue were mixed. After shaking, the adsorbed amount was measured (mg/g).

The study of the effect of temperature provides access to the calculation of the thermodynamic parameters of the adsorption process, namely the standard free Gibbs energy

(ΔG°, kJ mol^{-1}), the standard enthalpy (ΔH°, kJ mol^{-1}), and the standard entropy (ΔS°, kJ mol^{-1} K^{-1}) were calculated using the thermodynamic equations Eqs. (6−8):

$$\Delta G^{\circ} = \Delta H^{\circ} - T\Delta S^{\circ} \tag{6}$$

$$\Delta G^{\circ} = -RT \, lnK_C \tag{7}$$

$$Log \left(\frac{1000 \times Q_e}{C_e} \right) = \frac{-\Delta H^{\circ}}{2.303 \times RT} + \frac{\Delta S^{\circ}}{2.303 \times RT} \tag{8}$$

Where:

- Q_e is the amount of MB adsorbed per unit mass of samples (mg/g);
- Ce is the equilibrium concentration (mg/L);
- R is the universal gas constant (8.314 J/mol K);
- T is the temperature in Kelvin.

ΔG°: This represents the Gibbs free energy. Its negative value means that the reaction is thermodynamically possible.

ΔH°: Represents the standard enthalpy expressing the interaction energy between the molecules and the adsorbing surface. A negative value of ΔH° implies that the adsorption process is exothermic, and a positive value indicates that the adsorption process is endothermic.

ΔS°: Represents entropy. It measures order or disorder at the solid-liquid interface and expresses the solute's affinity for the adsorbent.

Plotting the curve Log (1000×qe Ce) = f (1/T) is used to determine ΔH° (slope of the line) and ΔS° (y-intercept).

II.8.4. Adsorption kinetics

The adsorption kinetics follow the decrease in the adsorbate concentration in the solution as a function of the contact time. The study of kinetics adsorption was carried out to determine the adsorbate's fixed quantities since the adsorbent-adsorbate was brought into contact until equilibrium. Therefore, the adsorption kinetics is defined by the evolution of the quantity adsorbed as a function of the contact time between the adsorbent and adsorbate. The kinetic study of the adsorption process is of considerable practical interest. It provides

information on the adsorption mechanism and the mode of transfer of solutes from the liquid phase (adsorbate) to the solid phase (adsorbent).

- The Kinetic studies were performed under conditions of T = 25 °C, pH = 6.4 with contact times 0-360 min for the **MBent** and **MBent-organo** adsorbents using a volume V = 20 mL of MB solution and adsorbent mass W =20 mg for each time in the initial concentration's domain 20 to 250 mg/L for the **MBent** and 50 to 150 mg/L **for MBent-organo**.

- The Kinetic studies were performed under conditions of T = 25 °C, pH = 6.4 with contact times 0 to 48 h for the **MBent-A beads** and **MBent-organo-A beads** adsorbents using a volume V = 20 mL of MB solution and adsorbent mass W =20 mg for each time in the initial concentration's domain 20 to 250 mg/L for the **MBent-A beads** and 50 to 150 mg/L for **MBent-organo-A beads**.

II.8.5. Kinetic modeling

Several models can be applied to explain the mechanisms that enter into the fixation of adsorbates on the adsorbents and evaluate the kinetic parameters of adsorption. Among the best-known and most used models to describe the mechanism of adsorption in the liquid phase, we retain three models: the pseudo-first-order model, the pseudo-second-order model, and the intraparticle diffusion model. Pseudo first-order and pseudo second-order kinetics models were applied to determine the adsorption rate and adsorption mechanism, which were expressed in Eq. (9) and Eq. (10) [20,21]. Intraparticle diffusion model was applied to study adsorption mechanism from the perspective of dye molecular diffusion, the model was shown as Eq. (11) [22]:

$$Q_t = Q_e(1 - exp^{-k_1*t}) \tag{9}$$

$$Q_t = \frac{Q_e^2 k_2 t}{1 + Q_e k_e t} \tag{10}$$

$$Q_t = K_{id} * t^{0.5} + C \tag{11}$$

Where:

- Q_e and Q_t are the amounts of methylene blue adsorbed (mg/g) at equilibrium and at time t (min);
- $k_1 (min^{-1})$ rate constant of the first-order kinetic model;
- $k_2 (g/ mg min)$ rate constant of the second-order kinetic model;

- K_{id} (mg/g min$^{1/2}$) is the intraparticle diffusion rate constant;
- C is the intercept.

II.8.6. Adsorption isotherms

The adsorption isotherm illustrates, at a fixed temperature, the amount of solution adsorbed by an adsorbent as an indicator of the liquid is a state of equilibrium concentration in the solution. The evaluation of the isotherms of adsorption is essential for elucidating the interactions between solution and adsorbent, and determining the capacity for adsorption of an adsorbent is crucial for the development of the adsorption system.

- The isotherms studies were performed under conditions of pH = 6.4, T = 15 °C, contact times 24 h for **MBent** and 48 h for **MBent-A beads** adsorbents using a volume V = 20 mL of MB solution and adsorbent mass W = 20 mg for each initial concentration's domain 60 to 500 mg/L for the **MBent** and 50 to 1500 mg/L for **MBent-A beads**. Then, the temperature was adjusted to 25°C, 30 °C and 40 °C, and repeated the above operation.

- The isotherms studies were performed under conditions of pH = 6.4, T = 20 °C, contact times 24 h for **MBent-organo** and 48 h for **MBent-organo-A beads** adsorbents using a volume V = 20 mL of MB solution and adsorbent mass W = 20 mg for each initial concentration's domain 60 to 500 mg/L for the **MBent-organo** and 50 to 1500 mg/L for **MBent-organo-A beads**. Then, the temperature was adjusted to 30 °C and 40 °C, and repeated the above operation.

II.8.7. Isotherm modeling

Langmuir and Freundlich models are the common adsorption isotherm models to characterize the interaction between adsorbents and adsorbates. For the Langmuir model, it assumed that the adsorption was monolayer and the adsorption energy was constant. For the Freundlich model, it assumed that the adsorption occurred on a heterogeneous system with various adsorption affinity [23]. The Langmuir model was expressed as Eq. (12) [24] and its basic characteristics could be expressed by a dimensionless constant RL which was called the

separation factor defined by the Eq. (13) [25], To determine whether the dye adsorption on the adsorbent is favorable or not, one can utilize the separation factor (RL) of the Langmuir model (unfavorable if RL > 1, linear if RL = 1, favorable if 0 < RL < 1, or irreversible if RL = 0). Furthermore, the Freundlich model was shown by Eq. (14) [26]:

$$Q_e = \frac{Q_m * K_L * C_e}{1 + K_L * C_e} \tag{12}$$

$$R_L = \frac{1}{1 + K_L * C_0} \tag{13}$$

$$Q_e = K_f \times C_e^{\frac{1}{n}} \tag{14}$$

Where:

- Q_e (mg/g) liquid concentration of MB adsorbed at equilibrium;
- Q_m (mg/g) Langmuir maximum adsorption capacity;
- K_L (L/mg) the Langmuir constant;
- C_e (mg/L) equilibrium concentration of MB;
- R_L The Langmuir model's separation factor;
- C_0 initial concentration of MB;
- K_f ((mg/g) (L/mg)$^{1/n}$) the Freundlich constant;
- n the adsorption intensity.

II.8.8. Statistical physics model

The Langmuir model, which we demonstrated in the previous section, supposes that each site can attach to a single molecule while ignoring lateral interactions between molecules that have been adsorbed. The statistical physics model predicts that each site can take in n molecules [27], as shown by Eqs. (15 and 16):

$$Q_e = \frac{n \times D_m}{1 + \left(\frac{C_{1/2}}{C_e}\right)^n} \tag{15}$$

$$N_{sat} = n \times D_m \tag{16}$$

Where:

- Q_e (mg/g) liquid concentration of MB adsorbed at equilibrium;
- n number of MB molecules adsorbed on the adsorbents surface per functional group;
- D_m (mg/g) the density of adsorbents functional groups engaged in dye adsorption;
- $C_{1/2}$ (mg/L) represents the equivalent half-saturation concentration;
- C_e (mg/L) equilibrium concentration of MB;
- N_{sat} (mg/g) is the MB adsorbed at saturation.

II.8.9. Error analysis

To choose the model that best fits experimental data, error functions R^2 (correlation coefficient) have been calculated using the non-linear regression method utilizing Eq. (17) The Origin software (version 2008) [28].

$$R^2 = 1 - \frac{\sum_{n=1}^{n}\left(Q_{e,te.exp.n} - Q_{e,t.cal.n}\right)^2}{\sum_{n=1}^{n}\left(Q_{e,t.exp.n} - \overline{Q_{e,t.exp.n}}\right)^2} \qquad (17)$$

Where:

- Q_t, exp /Q_t,cal represent the experimental /calculated adsorption capacity at a given time;
- Q_e, exp /Q_e.cal represent the experimental /calculated adsorption capacity at equilibrium;
- n indicates the number of observations.

II.8.10. Regeneration and reusability studies

Achieving efficient regeneration is one of the objectives of researchers, as well as minimizing processing costs for subsequent industrial applications [29]. The ability to regenerate and reuse adsorbents has significant implications in various industries. The regeneration method depends on the adsorbent type and the adsorbates' nature [29].

In this context, the possibility of reusing **MBent-A beads** and **MBent-organo-A beads** after being used for dye pollutant removal has been investigated in this work. 50 mg of adsorbent beads was added in a solution containing 50 mL volume MB with a concentration of 100 mg/L at pH (6.4). Under 48 h agitation time till the equilibrium state, distilled water was used to clean the beads many times and was kept to dry at room temperature. Afterward, in an acidic solution pH=2, the dried beads were introduced for desorption of MB for 48 h

[30]. This method was repeated five cycles of adsorption-desorption. On the other hand, regeneration efficiency was estimated based on Eq. (18) [31].

$$R\,(\%) = \frac{m_{des}}{m_{ads}} \times 100 \tag{18}$$

Where:

- m_{des} (mg) and m_{ads} (mg) are the amounts of methylene blue adsorbed and desorbed, respectively.

II.9. Computational investigations

The Material Studio software facilitated molecular dynamics (MD) simulations to assess the interaction energy between MB dye and the adsorbent model, comprising three distinct systems: Fe_3O_4 nanoparticle, Bentonite surface, and Alginate molecule. In the initial construction of the simulation box, MB molecules were strategically placed along side the three components to explore inherent interactions, with a primary focus on MB and the constituents of the adsorbent surface [32–35]—optimization of the initial box geometry aimed to relax the entire molecular system. Subsequently, the box underwent NVT dynamics for approximately 2000 picoseconds (using a 1 femtosecond time step) at a temperature of 298 Kelvin, employing the COMPASS force field. Following the NVT dynamics, a second MD simulation was carried out using the NPT thermodynamic ensemble for 20,000 picoseconds (with a 1 femtosecond time step) at 298 Kelvin. This phase involved another round of geometric optimization, and the energies of the resulting conformations were computed. The conformation with the lowest energy was selected as the model for subsequent analysis.

To delve deeper into the properties of the adsorption system and their interactions, the chosen model underwent further optimization using the DFT M06-2X functional [36] and the TZVP basis set [37–40], facilitated by the Turbomole software [41–46]. The investigation also incorporated an intricate analysis of non-covalent interactions (NCI) within a three-dimensional framework using approaches such as Reduced Density Gradient (RDG) and the Quantum Theory of Atoms in Molecules (QTAIM) [47–50].

The RDG analysis relies on electron densities (ρ) and reduced density gradients (RDGs), mathematically described by the Eq. (19):

$$s = \frac{1}{2(3\pi^2)^{1/3}} \frac{|\nabla\rho|}{\rho^{4/3}} \tag{19}$$

Here, ρ represents the electron density, and $\nabla\rho$ represents its initial derivative. This approach effectively identifies van der Waals and weak non-covalent interactions, including hydrogen bonds and steric repulsions, which become significant at specific distances and can significantly influence the system [51–53].

The computational tool Multiwfn was employed to conduct NCI analyses based on the RDG and identify weak interactions within the system [54]. RDG plots and QTAIM maps were retrieved and visualized using the Visual Molecular Dynamics (VMD) interface [55]. Additionally, color scatter plots of the components were generated using gnuplot [56]. These sophisticated computational techniques facilitated a comprehensive analysis of weak interactions within the investigated system.

References

[1] N. Daas, H. Zaghouane-Boudiaf, Synthesis and characterization of porous bentonite adsorbent and its application to remove methylene blue dye from aqueous solutions, Desalin. Water Treat. 249 (2022) 271–280. https://doi.org/10.5004/dwt.2022.28144.

[2] X. Zou, H. Zhang, T. Chen, H. Li, C. Meng, Y. Xia, J. Guo, Preparation and characterization of polyacrylamide / sodium alginate microspheres and its adsorption of MB dye, Colloids Surfaces A Physicochem. Eng. Asp. 567 (2019) 184–192. https://doi.org/10.1016/j.colsurfa.2018.12.019.

[3] J. Zhang, D. Cai, G. Zhang, C. Cai, C. Zhang, G. Qiu, K. Zheng, Z. Wu, Adsorption of methylene blue from aqueous solution onto multiporous palygorskite modified by ion beam bombardment: Effect of contact time, temperature, pH and ionic strength, Appl. Clay Sci. 83–84 (2013) 137–143. https://doi.org/10.1016/j.clay.2013.08.033.

[4] C.H. Weng, Y.T. Lin, T.W. Tzeng, Removal of methylene blue from aqueous solution by adsorption onto pineapple leaf powder, J. Hazard. Mater. 170 (2009) 417–424. https://doi.org/10.1016/j.jhazmat.2009.04.080.

[5] A. Öztürk, E. Malkoc, Adsorptive potential of cationic Basic Yellow 2 (BY2) dye onto natural untreated clay (NUC) from aqueous phase: Mass transfer analysis, kinetic and equilibrium profile, Appl. Surf. Sci. 299 (2014) 105–115. https://doi.org/10.1016/j.apsusc.2014.01.193.

[6] N. Belhouchat, H. Zaghouane-boudiaf, C. Viseras, Applied Clay Science Removal of anionic and cationic dyes from aqueous solution with activated organo-bentonite / sodium alginate encapsulated beads, Appl. Clay Sci. (2016). https://doi.org/10.1016/j.clay.2016.08.031.

[7] C. Vimlesh, P. Jaesung, C. Young, L. Jung Woo, H. In-Chul, S.K. Kwang, Water-Dispersible Magnetite-Reduced Graphene Oxide Composites for Arsenic Removal, ACS Nano 4 (2010) 3979–3986.

[8] B. Chen, Z. Chen, S. Lv, A novel magnetic biochar efficiently sorbs organic pollutants and phosphate, Bioresour. Technol. 102 (2011) 716–723. https://doi.org/10.1016/j.biortech.2010.08.067.

[9] L. de C. Alves, S. Yáñez-Vilar, Y. Piñeiro-Redondo, J. Rivas, Novel magnetic nanostructured beads for cadmium(II) removal, Nanomaterials 9 (2019). https://doi.org/10.3390/nano9030356.

[10]   A. Aichour, H. Zaghouane-Boudiaf, Synthesis and characterization of hybrid activated bentonite/alginate composite to improve its effective elimination of dyes stuff from wastewater, Appl. Water Sci. 10 (2020) 1–13. https://doi.org/10.1007/s13201-020-01232-0.

[11]   P.C. Lin, S. Lin, P.C. Wang, R. Sridhar, Techniques for physicochemical characterization of nanomaterials, Biotechnol. Adv. 32 (2014) 711–726. https://doi.org/10.1016/j.biotechadv.2013.11.006.

[12]   H. Fissan, S. Ristig, H. Kaminski, C. Asbach, M. Epple, Comparison of different characterization methods for nanoparticle dispersions before and after aerosolization, Anal. Methods 6 (2014) 7324–7334. https://doi.org/10.1039/c4ay01203h.

[13]   P. Luo, Y. Zhao, B. Zhang, J. Liu, Y. Yang, J. Liu, Study on the adsorption of Neutral Red from aqueous solution onto halloysite nanotubes, Water Res. 44 (2010) 1489–1497. https://doi.org/10.1016/j.watres.2009.10.042.

[14]   D.-S. Kim, Short Communication : Mesurement of Point of Zero Charge of Bentonite By Solubilization Technique and Its Dependence of Surface Potential on Ph, Environ. Eng. Res. 8 (2003) 222–227. https://doi.org/10.4491/eer.2003.8.4.222.

[15]   A.M. Oickle, S.L. Goertzen, K.R. Hopper, Y.O. Abdalla, H.A. Andreas, Standardization of the Boehm titration: Part II. Method of agitation, effect of filtering and dilute titrant, Carbon N. Y. 48 (2010) 3313–3322. https://doi.org/10.1016/j.carbon.2010.05.004.

[16]   A. Guediri, A. Bouguettoucha, D. Chebli, N. Chafai, A. Amrane, Molecular dynamic simulation and DFT computational studies on the adsorption performances of methylene blue in aqueous solutions by orange peel-modified phosphoric acid, J. Mol. Struct. 1202 (2020) 127290. https://doi.org/10.1016/j.molstruc.2019.127290.

[17]   A. Benhouria, M.A. Islam, H. Zaghouane-Boudiaf, M. Boutahala, B.H. Hameed, Calcium alginate-bentonite-activated carbon composite beads as highly effective adsorbent for methylene blue, Chem. Eng. J. 270 (2015) 621–630. https://doi.org/10.1016/j.cej.2015.02.030.

[18]   M. Doğan, M. Alkan, Ö. Demirbaş, Y. Özdemir, C. Özmetin, Adsorption kinetics of maxilon blue GRL onto sepiolite from aqueous solutions, Chem. Eng. J. 124 (2006) 89–101. https://doi.org/10.1016/j.cej.2006.08.016.

[19]   B.K. Nandi, A. Goswami, M.K. Purkait, Adsorption characteristics of brilliant green dye on kaolin, J. Hazard. Mater. 161 (2009) 387–395. https://doi.org/10.1016/j.jhazmat.2008.03.110.

[20] A. Aurich, J. Hofmann, R. Oltrogge, M. Wecks, R. Gläser, L. Blömer, S. Mauersberger, R.A. Müller, D. Sicker, A. Giannis, Improved Isolation of Microbiologically Produced (2R,3S)-Isocitric Acid by Adsorption on Activated Carbon and Recovery with Methanol, Org. Process Res. Dev. 21 (2017) 866–870. https://doi.org/10.1021/acs.oprd.7b00090.

[21] J. wei Wang, Lan Dai, Yong-qiang Liu, R. feng Li, X. ting Yang, G. hong Lan, H. yan Qiu, B. Xu, Adsorption properties of β-cyclodextrin modified hydrogel for methylene blue, Carbohydr. Res. 501 (2021). https://doi.org/10.1016/j.carres.2021.108276.

[22] S. Fan, Y. Wang, Z. Wang, J. Tang, J. Tang, X. Li, Removal of methylene blue from aqueous solution by sewage sludge-derived biochar: Adsorption kinetics, equilibrium, thermodynamics and mechanism, J. Environ. Chem. Eng. 5 (2017) 601–611. https://doi.org/10.1016/j.jece.2016.12.019.

[23] S.K. Pereira, S. Kini, B. Prabhu, G.P. Jeppu, A simplified modeling procedure for adsorption at varying pH conditions using the modified Langmuir–Freundlich isotherm, Appl. Water Sci. 13 (2023) 1–13. https://doi.org/10.1007/s13201-022-01800-6.

[24] M.H. Armbruster, J.B. Austin, The Adsorption of Gases on Plane Surfaces of Mica, J. Am. Chem. Soc. 60 (1938) 467–475. https://doi.org/10.1021/ja01269a066.

[25] Z. Wu, J. Wu, M. Huang, H. Liang, B. Sun, Preparation of reusable hydrogel spheres based on sodium alginate/Fe3O4 modified with carboxymethyl Huangshui polysaccharide and the efficient adsorption performance for methylene blue, Food Chem. 438 (2024) 138064. https://doi.org/10.1016/j.foodchem.2023.138064.

[26] H. Freundlich, Über die Adsorption in Lösungen, Zeitschrift Für Phys. Chemie 57U (1907) 385–470. https://doi.org/10.1515/zpch-1907-5723.

[27] L. Sellaoui, H. Guedidi, S. Knani, L. Reinert, L. Duclaux, A. Ben Lamine, Application of statistical physics formalism to the modeling of adsorption isotherms of ibuprofen on activated carbon, Fluid Phase Equilib. 387 (2015) 103–110. https://doi.org/10.1016/j.fluid.2014.12.018.

[28] L.S. Chan, W.H. Cheung, S.J. Allen, G. McKay, Error analysis of adsorption isotherm models for acid dyes onto bamboo derived activated carbon, Chinese J. Chem. Eng. 20 (2012) 535–542. https://doi.org/10.1016/S1004-9541(11)60216-4.

[29] F. Ogata, T. Nakamura, N. Kawasaki, Adsorption capability of virgin and calcined wheat bran for molybdenum present in aqueous solution and elucidating the adsorption mechanism by adsorption isotherms, kinetics, and regeneration, J. Environ. Chem. Eng. 6 (2018) 4459–4466. https://doi.org/10.1016/j.jece.2018.06.047.

[30] R. Wu, J.H. Liu, L. Zhao, X. Zhang, J. Xie, B. Yu, X. Ma, S.T. Yang, H. Wang, Y. Liu, Hydrothermal preparation of magnetic Fe3O4@C nanoparticles for dye adsorption, J. Environ. Chem. Eng. 2 (2014) 907–913. https://doi.org/10.1016/j.jece.2014.02.005.

[31] N. Djebri, M. Boutahala, N. Chelali, N. Boukhalfa, International Journal of Biological Macromolecules Enhanced removal of cationic dye by calcium alginate / organobentonite beads : Modeling , kinetics , equilibriums , thermodynamic and reusability studies, Int. J. Biol. Macromol. 92 (2016) 1277–1287. https://doi.org/10.1016/j.ijbiomac.2016.08.013.

[32] D. Bousba, C. Sobhi, E. Zouaoui, K. Rouibah, A. Boublia, H. Ferkous, A. Haddad, A. Gouasmia, I. Avramova, Z. Mohammed, V.I. Parvulescu, K.K. Yadav, M. Hasan, M.M.S. Cabral-Pinto, N. Elboughdiri, Y. Benguerba, Efficient biodiesel production from recycled cooking oil using a NaOH/CoFe2O4 magnetic nano-catalyst: synthesis, characterization, and process enhancement for sustainability, Energy Convers. Manag. 300 (2024) 118021. https://doi.org/10.1016/j.enconman.2023.118021.

[33] C. Boulechfar, H. Ferkous, A. Delimi, M. Berredjem, A. Kahlouche, A. Madaci, S. Djellali, S. Boufas, A. Djedouani, A. Errachid, A. Ali Khan, A. Boublia, T. Lemaoui, Y. Benguerba, Corrosion inhibition of Schiff base and their metal complexes with [Mn (II), Co (II) and Zn (II)]: Experimental and quantum chemical studies, J. Mol. Liq. 378 (2023) 121637. https://doi.org/10.1016/j.molliq.2023.121637.

[34] T. Yasmin, A. Mahmood, M. Farooq, U. Rehman, R.M. Sarfraz, H. Ijaz, M.R. Akram, A. Boublia, M.M. Salem Bekhit, B. Ernst, Y. Benguerba, Quince seed mucilage/β-cyclodextrin/Mmt-Na+-co-poly (methacrylate) based pH-sensitive polymeric carriers for controlled delivery of Capecitabine, Int. J. Biol. Macromol. 253 (2023) 127032. https://doi.org/10.1016/j.ijbiomac.2023.127032.

[35] T. Yasmin, A. Mahmood, M. Farooq, R.M. Sarfraz, A. Boublia, U. Rehman, M.U. Ashraf, J.K. Bhutto, B. Ernst, M. Albrahim, N. Elboughdiri, K.K. Yadav, M.A. Alreshidi, H. Ijaz, Y. Benguerba, Development and evaluation of a pH-responsive

Mimosa pudica seed mucilage/β- cyclodextrin-co-poly(methacrylate) hydrogel for controlled drug delivery: In vitro and in vivo assessment, Int. J. Biol. Macromol. (2024) 131832. https://doi.org/https://doi.org/10.1016/j.ijbiomac.2024.131832.

[36]   K.A. Moltved, K.P. Kepp, Performance of density functional theory for transition metal oxygen bonds, ChemPhysChem. 20 (2019) 3210–3220.

[37]   A. Mouffok, D. Bellouche, I. Debbous, A. Anane, Y. Khoualdia, A. Boublia, A.S. Darwish, T. Lemaoui, Y. Benguerba, Synergy of garlic extract and deep eutectic solvents as promising natural Antibiotics: Experimental and COSMO-RS, J. Mol. Liq. 375 (2023) 121321. https://doi.org/10.1016/j.molliq.2023.121321.

[38]   D. Uka, B. Blagojević, O. Alioui, A. Boublia, N. Elboughdiri, Y. Benguerba, T. Jurić, B.M. Popović, An innovative and environmentally friendly approach for resveratrol solubilization and bioaccessibility enhancement by using natural deep eutectic solvents, J. Mol. Liq. 391 (2023) 123411. https://doi.org/10.1016/j.molliq.2023.123411.

[39]   A. Boublia, Z. Guezzout, N. Haddaoui, M. Badawi, A.S. Darwish, T. Lemaoui, F. Banat, K.K. Yadav, B.H. Jeon, N. Elboughdiri, Y. Benguerba, I.M. Al Nashef, Enhancing precision in PANI/Gr nanocomposite design: Robust machine learning models, outlier resilience, and molecular input insights for superior electrical conductivity and gas sensing performance, J. Mater. Chem. A. 12 (2023) 2209–2236. https://doi.org/10.1039/d3ta06385b.

[40]   Z. Jebali, H. Ferkous, M. Zerroug, A. Boublia, A. Delimi, A. Bouzid, H. Majdoub, B. Ernst, N. Elboughdiri, Y. Benguerba, Unveiling the potent corrosion-inhibiting power of Ammophila arenaria aqueous extract for mild steel in acidic environments: An integrated experimental and computational study, J. Environ. Chem. Eng. 12 (2024) 112374. https://doi.org/10.1016/j.jece.2024.112374.

[41]   T. Lemaoui, A. Boublia, A.S. Darwish, M. Alam, S. Park, B.-H. Jeon, F. Banat, Y. Benguerba, I.M. AlNashef, Predicting the Surface Tension of Deep Eutectic Solvents Using Artificial Neural Networks, ACS Omega. (2022).

[42]   A. Boublia, T. Lemaoui, J. AlYammahi, A.S. Darwish, A. Ahmad, M. Alam, F. Banat, Y. Benguerba, I.M. AlNashef, Multitask Neural Network for Mapping the Glass Transition and Melting Temperature Space of Homo- and Co-Polyhydroxyalkanoates

Using σProfiles Molecular Inputs, ACS Sustain. Chem. Eng. 11 (2023) 208–227. https://doi.org/10.1021/acssuschemeng.2c05225.

[43] A. Boublia, T. Lemaoui, F. Abu Hatab, A.S. Darwish, F. Banat, Y. Benguerba, I.M. AlNashef, Molecular-based artificial neural network for predicting the electrical conductivity of deep eutectic solvents, J. Mol. Liq. 366 (2022) 120225. https://doi.org/10.1016/j.molliq.2022.120225.

[44] T. Lemaoui, A. Boublia, S. Lemaoui, A.S. Darwish, B. Ernst, M. Alam, Y. Benguerba, F. Banat, I.M. AlNashef, Predicting the CO2 Capture Capability of Deep Eutectic Solvents and Screening over 1000 of their Combinations Using Machine Learning, ACS Sustain. Chem. Eng. 11 (2023) 9564–9580. https://doi.org/10.1021/acssuschemeng.3c00415.

[45] J. AlYammahi, A.S. Darwish, T. Lemaoui, A. Boublia, Y. Benguerba, I.M. AlNashef, F. Banat, Molecular Guide for Selecting Green Deep Eutectic Solvents with High Monosaccharide Solubility for Food Applications, ACS Omega. 8 (2023) 26533–26547. https://doi.org/10.1021/acsomega.3c03326.

[46] T. Lemaoui, A.S. Darwish, G. Almustafa, A. Boublia, P.R. Sarika, N.A. Jabbar, T. Ibrahim, P. Nancarrow, K.K. Yadav, A.M. Fallatah, M. Abbas, J.S. Algethami, Y. Benguerba, B.H. Jeon, F. Banat, I.M. AlNashef, Machine learning approach to map the thermal conductivity of over 2,000 neoteric solvents for green energy storage applications, Energy Storage Mater. 59 (2023) 102795. https://doi.org/10.1016/j.ensm.2023.102795.

[47] S. Kr, M. Murmu, N. Chandra, P. Banerjee, Benzothiazolylhydrazine azomethine derivatives for efficient corrosion inhibition of mild steel in acidic environment : Integrated experimental and density functional theory cum molecular dynamics simulation approach, J. Mol. Liq. 364 (2022) 120033. https://doi.org/10.1016/j.molliq.2022.120033.

[48] E.R. Johnson, S. Keinan, P. Mori-Sánchez, J. Contreras-García, A.J. Cohen, W. Yang, Revealing noncovalent interactions, J. Am. Chem. Soc. 132 (2010) 6498–6506.https://doi.org/10.1021/ja100936w

[49] N. Benachour, A. Delimi, H. Allal, A. Boublia, A. Sedik, H. Ferkous, A. Djedouani, S.

Brioua, C. Boulechfar, H. Benzouid, A. Houssou, A. Oral, B. Ernst, M. Alam, Y. Benguerba, 3,4-Dimethoxy phenyl thiosemicarbazone as an effective corrosion inhibitor of copper under acidic solution: comprehensive experimental, characterization and theoretical investigations, RSC Adv. 14 (2024) 12533–12555. https://doi.org/10.1039/D3RA08629A.

[50]   N. Ramdane, Z. Marsa, A. Delimi, A. Sedik, A. Boublia, G.S. Albakri, M. Abbas, K. Kumar Yadav, M. Gabsi, A. Djedouani, K.O. Rachedi, L. Toukal, H. Benzouid, M. Berredjem, H. Ferkous, Y. Benguerba, Synergistic shielding of copper from nitric acid corrosion: Unveiling the mechanisms through electrochemical, characterization, and computational insights with 2-Hydroxybenzaldehyde oxime, Inorg. Chem. Commun. (2024) 112479. https://doi.org/https://doi.org/10.1016/j.inoche.2024.112479.

[51]   S. Mandal, S. Bej, P. Banerjee, Insights into the uses of two azine decorated d10-MOFs for corrosion inhibition application on mild steel surface in saline medium: Experimental as well as theoretical investigation, J. Mol. Liq. 381 (2023) 121789. https://doi.org/10.1016/j.molliq.2023.121789.

[52]   A. Boutouil, M.R. Laamari, I. Elazhary, L. Bahsis, H. Anane, S.-E. Stiriba, Towards a deeper understanding of the inhibition mechanism of a new 1,2,3-triazole derivative for mild steel corrosion in the hydrochloric acid solution using coupled experimental and theoretical methods, Mater. Chem. Phys. 241 (2020) 122420. https://doi.org/https://doi.org/10.1016/j.matchemphys.2019.122420.

[53]   K. Benbouguerra, N. Chafai, S. Chafaa, Y.I. Touahria, H. Tlidjane, New α-Hydrazinophosphonic acid: Synthesis, characterization, DFT study and in silico prediction of its potential inhibition of SARS-CoV-2 main protease, J. Mol. Struct. 1239 (2021) 130480. https://doi.org/10.1016/j.molstruc.2021.130480.

[54]   T. Lu, F. Chen, Multiwfn: A multifunctional wavefunction analyzer, J. Comput. Chem. 33 (2012) 580–592. https://doi.org/10.1002/jcc.22885

[55]   W. Humphrey, A. Dalke, K. Schulten, VMD: Visual molecular dynamics, J. Mol. Graph. 14 (1996) 33–38. https://doi.org/https://doi.org/10.1016/0263-7855(96)00018-5.

[56]   T. Williams, C. Kelley, H.B. Bröker, J. Campbell, R. Cunningham, D. Denholm, E. Elber, R. Fearick, C. Grammes, L. Hart, Gnuplot 4.5: an interactive plotting program. 2011, URL Http//Www. Gnuplot. Info. 56 (2017).

CHAPTER III

Characterization and study of the adsorption of Methylene blue by magnetic bentonite and magnetic bentonite beads

CHAPTER III

CHARACTERIZATION AND STUDY OF THE ADSORPTION OF METHYLENE BLUE BY MAGNETIC BENTONITE AND MAGNETIC BENTONITE BEADS

III.1. Introduction

In this chapter, which will be divided into three parts, we will study, in a discontinuous system, the adsorption of methylene blue (MB) on magnetic bentonite and magnetic bentonite beads.

In the first part, we will interpret the characterization results of the materials prepared during this study to better identify their textural, morphological, and physicochemical properties. The methods used include Fourier transform infrared spectroscopy (FTIR), X-ray diffraction (XRD), scanning electron microscopy (SEM)/energy-dispersive X-ray spectroscopy (EDS), and the determination of isoelectric points (pHpzc).

In the second part, we will analyze the experimental results of the adsorption process for each adsorbent. This includes the impact of pH, adsorbent dosage, temperature, and thermodynamic adsorption parameters, as well as the effect of the initial adsorbate concentration. We will also examine adsorption kinetics to determine the contact time required to reach equilibrium, along with adsorption isotherms characteristic of each adsorbent-adsorbate system.

In the third part, we will focus on the theoretical study of adsorption on magnetic bentonite beads. Molecular modeling computations will be performed using DFT, AIM, FMO, MEP, RDG, and QTAIM analysis to gain deeper insight into the adsorption mechanism at the molecular level.

III.2. Characterization

III.2.1. Fourier-transform infrared spectroscopy

Bent, MBent, Alginate and MBent-A beads spectrums are depicted in Figure III.1 to follow the functional groups of Bentonite raw material before and after modification. The broadband appeared at 3442 cm^{-1} for the Bent spectrum and is assigned to OH hydroxy group stretching vibrations. In addition, 1637 cm^{-1} may be referred to as H-O-H deformation. The peak that appeared at 1031 cm^{-1} is Si-O, whereas those shown at 530 cm^{-1} and 463 cm^{-1} are assigned to the deformation of Al-O-Si and Si-O-Si.

In the MBent spectrum, the broad, intense absorption peak at around 3423 cm-1 corresponds to the HO-H vibration of water molecules absorbed on the silicate surface. In contrast, the peak at 3619 cm^{-1} is due to the O-H stretching vibration of silanol groups (Si-OH) [1]. The peak at 1637 cm^{-1} is attributed to the bending HO-H bonding of water molecules retained in the silicate matrix. The strong band at 1031 cm^{-1} and the band at 792 cm^{-1} represent the tetrahedral sheet's Si-O-Si groups. In addition, the absorption bands at 637.91, 567.08 and 463 cm^{-1} can observe the presence of magnetite nanoparticles. These bands result from splitting the first vibration band at 570 cm^{-1} corresponding to the Fe-O bond of bulk magnetite [2] and the shift of the second vibration band of the Fe-O bond of bulk magnetite to a higher wave spectrum [3].

Alginate's structure is well-known in the literature [4]. Their characteristic functional groups are well observed: 3423 cm^{-1} is also attributed to OH hydroxy group stretching vibrations, whereas 2929 cm^{-1} this peak is attributed to C-H vibration. Additionally, 1127 cm^{-1} is due to the C-O of the ether group. Moreover, 1031 cm^{-1} is the C-O of the alcoholic group, whereas the peaks located at 1617 and 1419 cm^{-1} are attributed to the asymmetric and symmetric stretching vibration of the carboxylate group.

The spectrum of MBent-A exhibits bands located at 3437, 2929,1617, 1426, and 463cm^{-1}, which bears a resemblance to the bands observed in both alginate and Bentonite which indicates the modification of Bentonite with alginate noteworthy a noticeable peak appeared at 572 cm^{-1} referred to Fe-O vibration which due to nanoparticles Fe$_3$O$_4$ [3].
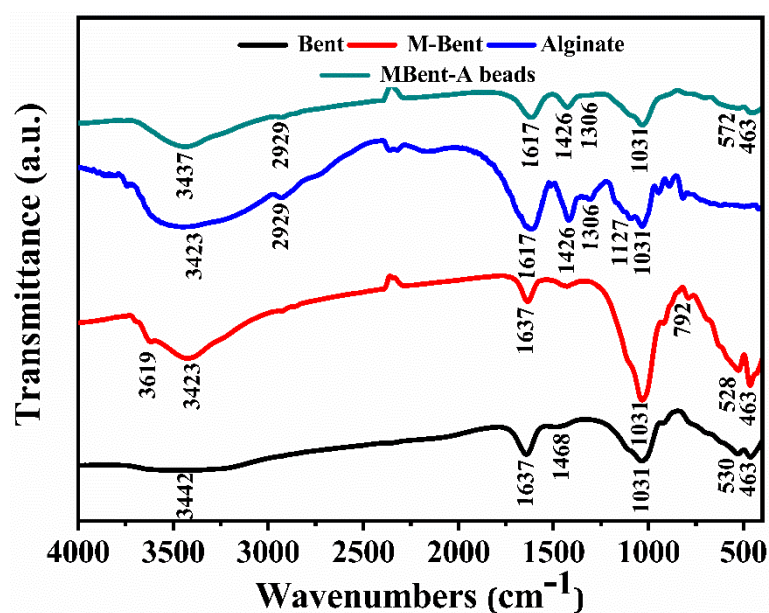
Figure III.1. FTIR spectrum of Bent, MBent, Alginate and MBent-A beads.

III.2.2. X-ray diffraction

X-ray diffraction characteristic of Bent, M-Bent and MBent-A bead's is shown in Figure III.2. The XRD study shows peaks of diffraction in both illustrations at $2\theta = 7.24°$, $19.9°$, and $26.7°$, which correspond to the Bentonite's (0 0 1), (1 1 0), and (2 1 0) planes, respectively [5]. The seven different peaks that appear at $2\theta = 20.1°$, $30.2°$, $35.7°$, $43.1°$, $53.9°$, $57.2°$, and $63.1°$ can be indexed by the (1 1 1) (2 0 0), (3 1 1), (4 0 0), (4 2 2), and (5 1 1) planes according to the magnetic crystalline phase. The Fe_3O_4-NPs incorporated in the M-Bent and MBent-A bead's structure verify the presence of the Fe_3O_4 cubic structure (01-075-0449 JCPD standard) [6,7] and show that the crystallinity nature was maintained throughout the whole synthesis. The relative intensity and peak locations are in agreement with the magnetite theoretical pattern.
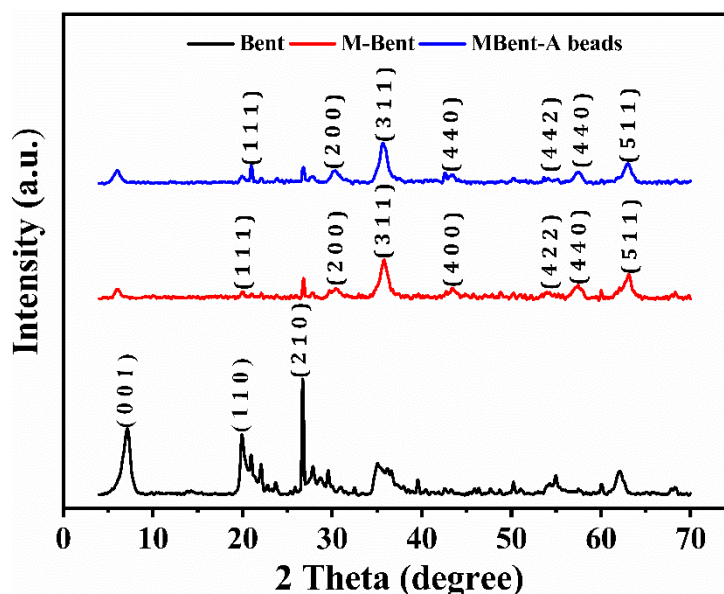
Figure III.2. XRD curve of Bent, MBent, and MBent-A beads.

III.2.3. Scanning electron microscopy /energy-dispersive X-ray spectroscopy

The SEM images of Bent, M-Bent and MBent-A beads are shown in in Figure III.3 (a,b and c), respectively. in Figure III.3 (a), it is evident that the majority of particles show heterogeneity and porosity of the microstructure of Bentonite. Comparing in Figure III.3 (a) to in Figure III.3 (b), aggregation of Fe_3O_4 nanoparticles as well as several individual Fe_3O_4 nanoparticles with nano-size were seen on the surface of bentonite. Fe_3O_4 nanoparticles indicate that M-Bent is a magnetic adsorbent, and the porous structure of the Fe_3O_4 aggregation indicates that the presence of Fe_3O_4 around the bentonite surface has no negative

effect on the interaction between MB and bentonite. The SEM image in Figure III.3 (c) illustrates a single MBent-A beads with a nearly spherical shape, indicative of successful beads formation By comparing the electron microscope (EDS) results represented in the tables inside Figure III.3 (a,b and c), the atomic percentage of iron has increased from 1.8 % to 14.4 %, verifying the presence of additional Fe_3O_4 nanoparticles on the surface of bentonite and indicating that Bentonite and iron nanoparticle have been smoothly incorporated into the composition of M-Bent. After encapsulation of magnetic bentonite with alginate, the atomic percentage of iron is reduced from 14.4 % to 2.28 %, which explains the influence of alginate on the atomic percentage of iron, but the beads retain their magnetic properties [8].

a)

Element	Atomic %
O	53.40
Na	2.92
Mg	0.84
Al	7.69
Si	29.18
Cl	0.28
K	0.87
Ca	1.05
Ti	0.83
V	0.70
Mn	0.57
Fe	1.7

b)

Element	Atomic %
O	58.39
Na	-
Mg	0.45
Al	4.86
Si	14.35
Cl	0.15
K	1.05
Ca	0.86
Ti	-
V	2.02
Mn	2.50
Fe	15.38

c)

Element	Atomic %
O	75.21
Na	0
Mg	0.62
Al	2.80
Si	12.1
Cl	0.48
K	0.18
Ca	4.03
Ti	0
V	0.99
Mn	1.36
Fe	2.28
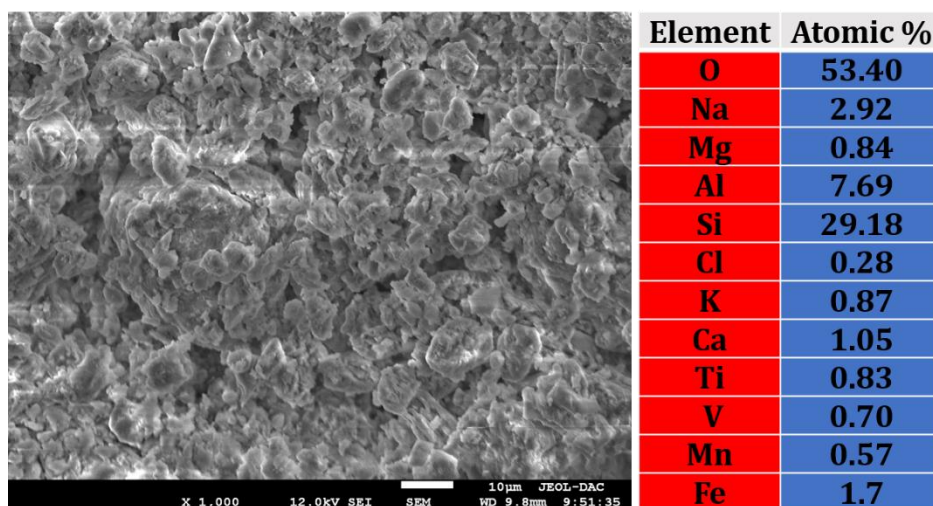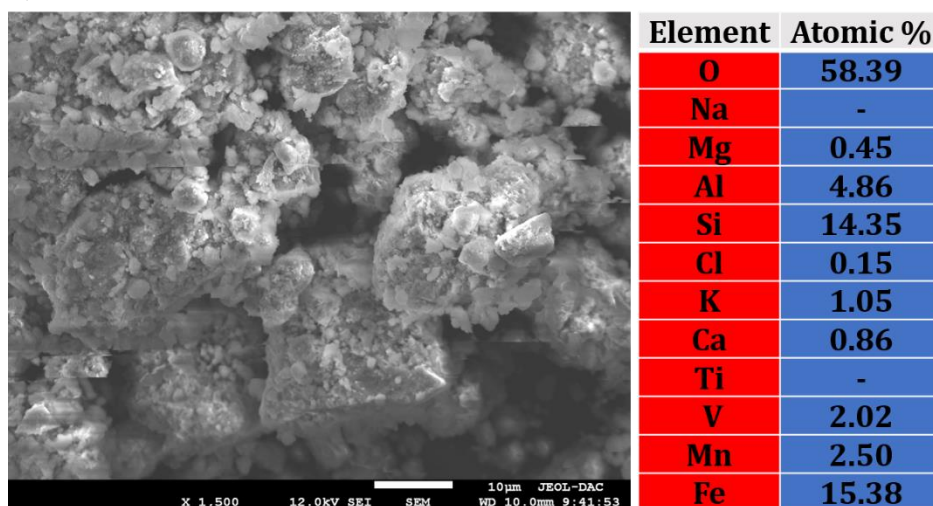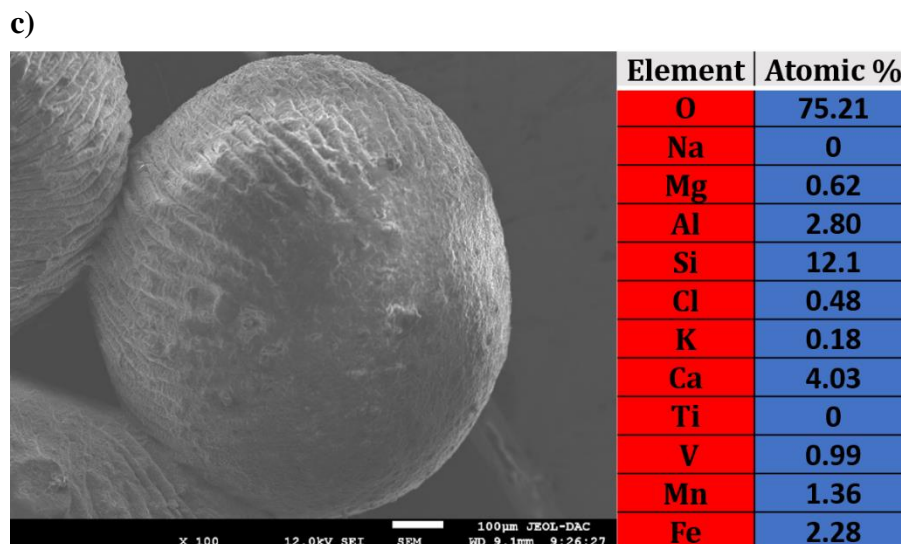
Figure III.3. SEM images and EDS curves (a) of Bent, (b) of M-Bent and (c) of MBent-A beads.

III.2.4. Point of zero charge

The zero charge pH_{pzc} for both M-Bent and MBent-A beads was ascertained and is shown in Figure III.4. The pH at the point of zero charge (pH_{pzc}) signifies the pH level at which the surface charge of the material is neutral, indicating an absence of net charge. This is essential for comprehending the adsorption process and the interactions between the adsorbent and adsorbate. For M-Bent (Figure III.3 (a)), the pH at the point of zero charge (pH_{pzc}) is 8.41. At pH levels below 8.41, the surface of M-Bent is positively charged, and at pH values over 8.41, it becomes negatively charged. The curve illustrating the disparity between the starting pH (pH_i) and the final pH (pH_f) clearly intersects the pH axis at 8.41, therefore validating the zero-charge point, MBent-A beads Figure III.3 (b) demonstrate a reduced pH_{pzc} of 7.70. At pH levels below 7.70, the MBent-A beads possess a positive surface charge, but at pH values over 7.70, they exhibit a negative surface charge [9]. The curve's intersection with the pH axis at this value signifies the zero-charge point for MBent-A [10].
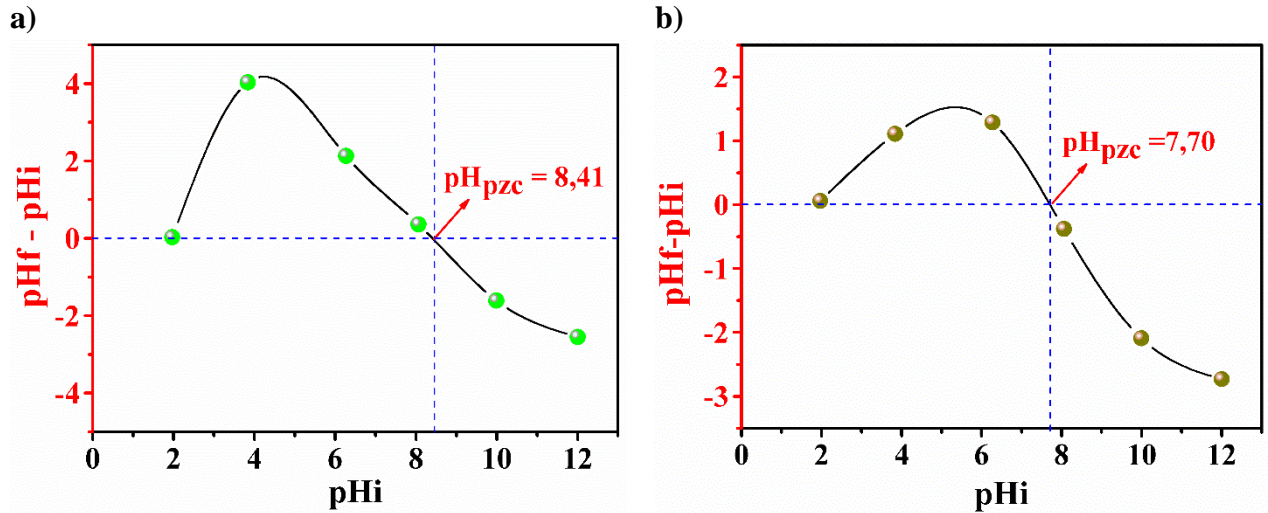
Figure III.4. Zero charge pH (pH_{pzc}) point (a) of M-Bent and (b) of MBent-A beads.

In summary, the pH point of zero charge (pH_{pzc}) values for both materials show minor variations, with M-Bent presenting a higher pH_{pzc} (8.41) in contrast to MBent-A (7.70). This indicates that the MBent-A beads possess a neutral surface charge at a lower pH relative to M-Bent, potentially affecting their adsorption characteristics across different pH conditions.

III.3. Adsorption parameters experimental results

III.3.1. pH parameter impact
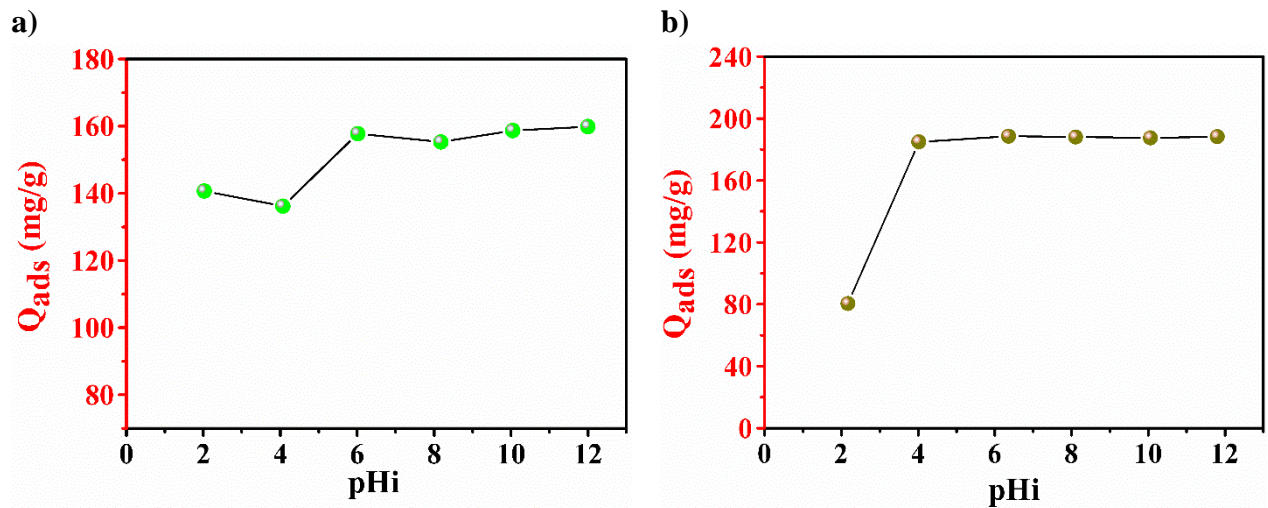
Figure III.5. Effect of pH (a) of M-Bent and (b) of MBent-A beads (Initial MB dye concentration = 200 mg/L, V = 20 ml, W= 20 mg, T = 25 °C and stirring speed = 250rpm).

The influence of pH on the adsorption capacity (Qads) for both M-Bent and MBent-A beads is seen in Figure III.5. In the case of M-Bent (Figure III.5 (a)), the adsorption capacity exhibits a progressive increase with rising pH, especially beyond pH = 4. The adsorption maxima occur between pH 6 and 8, after which stabilization ensues, demonstrating a little pH dependence at higher levels. The adsorption behavior of MBent-A beads (Figure III.5 (b)) exhibits a pronounced rise in adsorption capacity until pH = 4, after which the capacity levels off over the subsequent pH range. This indicates that while both materials provide excellent adsorption at elevated pH levels, MBent-A beads exhibit a more significant pH dependence at reduced pH, subsequently followed by stability. The findings suggest that MBent-A beads exhibit a more robust initial contact with the adsorbate at low pH relative to M-Bent; nonetheless, both materials attain comparable adsorption effectiveness at elevated pH levels [11].

III.3.2. Dosage absorbent parameter impact

a)

b)
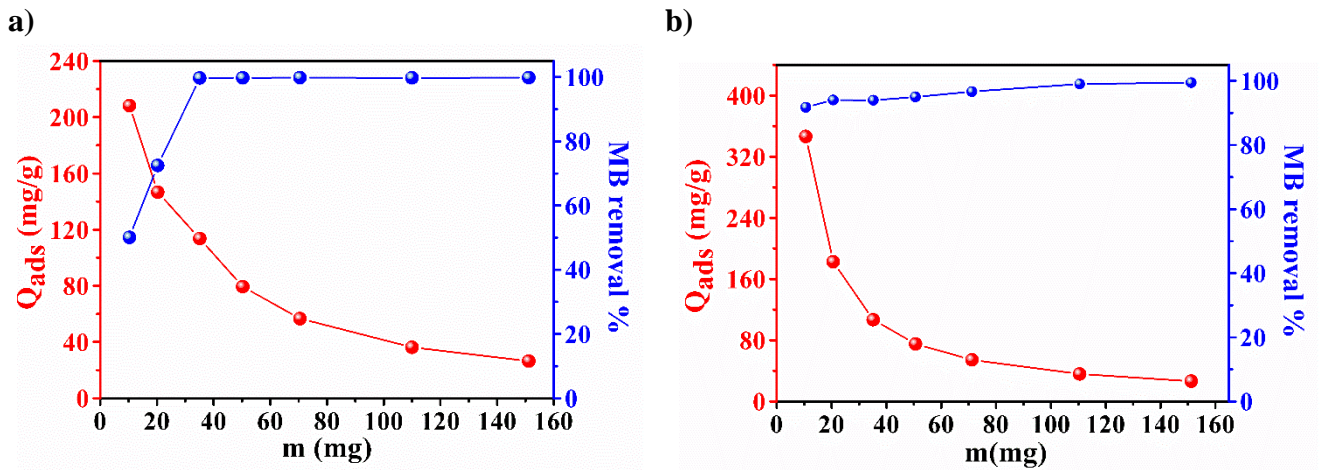
Figure III.6. Effect of dosage adsorbent (a) of M-Bent and (b) of MBent-A beads (Initial MB dye concentration = 200 mg/L, V = 20 ml, T = 25 °C and stirring speed = 250rpm).

Figure III.6 illustrates the impact of adsorbent dosage on the adsorption capacity (Qads) and Methylene Blue (MB) removal percentage of both M-Bent and MBent-A beads. The adsorption capacity of M-Bent (Figure III.6 (a)) experiences a substantial decrease as the adsorbent dosage increases, with a precipitous drop initially and a gradual decline thereafter. This behavior can be attributed to the availability and saturation of active sites on the surface of the adsorbent. At lower dosages, the active sites are readily available, allowing for high

adsorption capacity per unit mass. However, as the adsorbent dosage increases, the total number of available sites increases, but the ratio of adsorbate molecules to available active sites decreases, leading to lower adsorption efficiency per gram of adsorbent. Conversely, the MB removal percentage experiences a rapid increase, culminating in a nearly 100% removal rate at approximately 40 mg of adsorbent, after which it remains consistent. This suggests that despite the decrease in adsorption capacity per unit mass, the total number of active sites becomes sufficient to achieve near-complete MB removal as the dosage increases. Similarly, the adsorption capacity of MBent-A beads (Figure III.6 (b)) exhibits a significant decline with increasing adsorbent dosage, a trend that can also be explained by the saturation of active sites. [12] have observed that this behavior is consistent with the results of comparable studies, in which the MB removal percentage increases rapidly and reaches a plateau at 40 mg, where it is nearly 100 %. These findings demonstrate that, despite the decrease in adsorption capacity per unit mass as adsorbent dosage increases, both materials effectively remove MB, attaining near-complete removal at modest dosages. MBent-A beads, however, exhibit a higher maximal adsorption capacity than M-Bent, likely due to a greater number of active sites or stronger interactions between the dye molecules and the surface of the adsorbent [13].

III.3.3. Temperature parameter impact and thermodynamic adsorption parameters
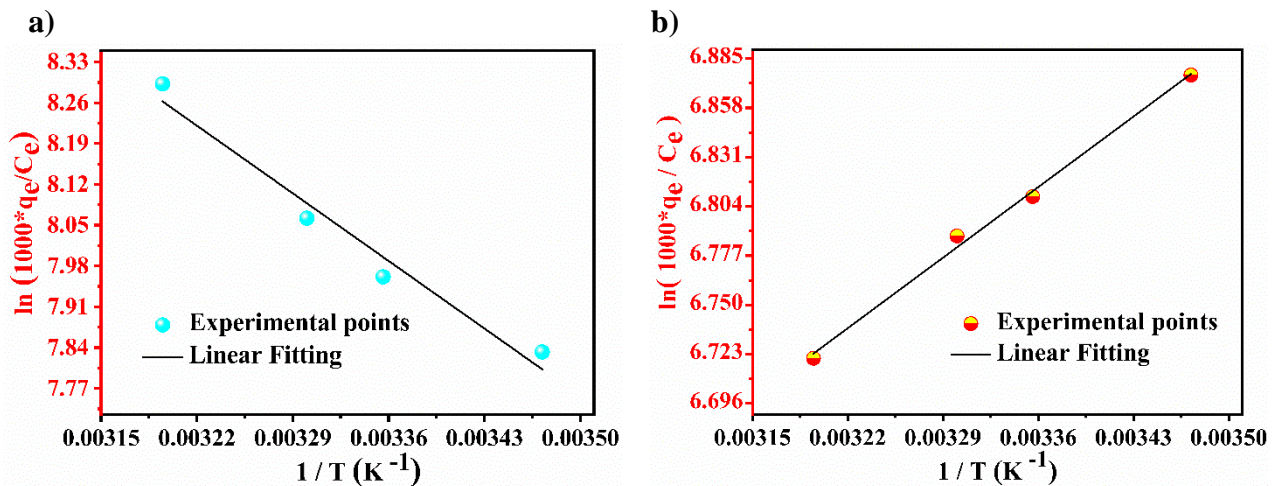
Figure III.7. Regression of the thermodynamic parameters on the MB adsorption onto (a) of M-Bent and (b) of MBent-A beads.

Figure III.7 illustrates the thermodynamic behavior of the adsorption process, depicting the regression of the thermodynamic parameters for the adsorption of Methylene Blue (MB) onto M-Bent and MBent-A beads.

Figure III.7 (a), despiting the adsorption onto M-Bent, adsorption increases with temperature, indicating an endothermic process. This is confirmed by the positive ΔH° value in Table III.1, meaning that the system absorbs heat to facilitate MB adsorption. Additionally, the positive ΔS° value indicates an increase in disorder at the solid-liquid interface, suggesting that MB molecules are more randomly distributed on the adsorbent surface after adsorption. The negative Gibbs free energy (ΔG°) values at all temperatures confirm that the process is spontaneous, with spontaneity increasing as temperature rises, which is characteristic of an endothermic reaction [14].

Table III.1. Thermodynamic properties of MB adsorption on M-Bent.

T (K)	ΔH° (kJ/mol)	ΔS° (J/mol^{-1}K)	ΔG° (kJ/mol)
288			-18.68
298			-19.81
303	13.78	112.71	-20.37
313			-21.50

On the other hand, Figure III.7 (b), illustrating the adsorption of MB onto MBent-A beads, highlights an exothermic process, as evidenced by the negative ΔH° values in Table III.2. Adsorption decreases with increasing temperature, meaning that the system releases heat, making the process more favorable at lower temperatures. The positive ΔS° value also reflects an increase in disorder. The negative ΔG° values confirm that adsorption is thermodynamically favorable at all studied temperatures, although the decrease in ΔG° with rising temperature indicates lower spontaneity at higher temperatures [15].

Table III.2. Thermodynamic properties of MB adsorption on MBent-A beads.

T (K)	ΔH° (kJ/mol)	ΔS° (J/mol^{-1}K)	ΔG° (kJ/mol)
288			-16.47
298			-16.88
303	-4.59	41.23	-17.08
313			-17.50

Thus, adsorption on M-Bent is an endothermic process, requiring an energy input [16] and leading to a significant increase in disorder at the solid-liquid interface. In contrast, adsorption on MBent-A is an exothermic process, favored at lower temperatures and accompanied by a more moderate change in entropy.

III.3.4. MB initial concentration and contact time parameters influence
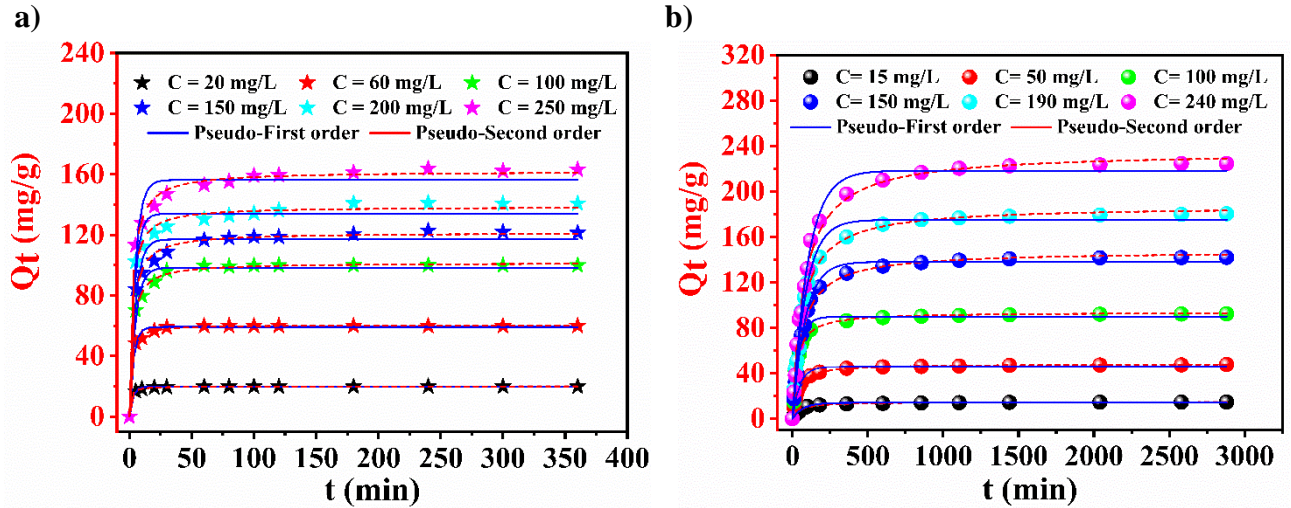
Figure III.8. Initial dye concentration and non-linear fitting of pseudo-first-order and pseudo-second-order model (a) of M-Bent and (b) of MBent-A beads
($V = 20$ ml, $W = 20$ mg, $T = 25$ °C and stirring speed $= 250$rpm).

The analysis of the acquired curves demonstrates the influence of the initial MB dye concentration, as seen in Figure III.8 (a and b), with concentrations evaluated from 20 to 250 mg/L for M-Bent and 15 to 240 mg/L for MBent-A beads.

An increased starting dye concentration resulted in a greater adsorption capability. For M-Bent Figure III.8 (a), at a dosage of 20 mg/L, the adsorption capacity was around 15 mg/g, while at 250 mg/L, it was around 160 mg/g. This phenomenon may be attributed to the prevalence of vacant active sites in the early phases of adsorption. At reduced MB dye concentrations (20 mg/L), equilibrium was attained rapidly, in around 25 minutes, but at elevated concentrations (250 mg/L), equilibrium was achieved more gradually, in about 100 minutes. At high concentrations, this may result from the gradual saturation of active sites, impeding the equilibrium process [17].

A same pattern is seen with MBent-A beads (Figure III.8 (b)). At a low concentration of 15 mg/L, the adsorption capacity achieved around 10 mg/g, with equilibrium established after

roughly 20 minutes. At a concentration of 240 mg/L, the adsorption capacity attained roughly 215 mg/g, with equilibrium established after about 600 minutes (10 hours). This indicates that at elevated concentrations, the diffusion of solute molecules into the adsorbent's matrix is impeded, extending the adsorption duration. An increase in the initial MB concentration enhances adsorption capacity but delays equilibrium attainment, possibly owing to accelerated saturation of active sites and reduced diffusion through the adsorbent. The equilibrium period for methylene blue adsorption on MBent-A beads is around 10 hours at elevated concentrations.

III.3.5. Kinetic modeling

Kinetic parameters were derived through non-linear regression analysis and are presented in Table III.3 and 4. The experimental data for M-Bent (Table III.3) demonstrates a strong correlation with the pseudo-second-order model, as evidenced by the high R^2 values, which range from 0.992 to 0.999. The equilibrium adsorption capacity qe for MB increases from 20.06 mg/g to 162.02 mg/g as the initial concentration increases from 20 mg/L to 250 mg/L.

For the MBent-A beads (Table III.4), the pseudo-second-order model demonstrates a strong fit, with R^2 values ranging from 0.989 to 0.999. The equilibrium adsorption capacity q_e for MB significantly increases from 14.90 mg/g at an initial concentration of 15 mg/L to 235.03 mg/g at 240 mg/L. The results indicate a higher adsorption capacity at increased initial dye concentrations for both M-Bent and MBent-A, suggesting a greater availability of active sites during the initial stages of adsorption.

The high determination coefficient (R^2) values, which range from 0.992 to 0.999 in Table III.3, indicate that the pseudo-second-order kinetic model effectively describes the adsorption of MB dye on M-Bent within the examined concentration range. The pseudo-first-order model demonstrated R^2 values between 0.963 and 0.996, suggesting a less accurate fit to the experimental data. The rate constants k_1 and k_2 are significantly affected by the initial concentrations of MB dye. The k_1 values decline from $36.29.10^{-2}$ L/min at 20 mg/L to $21.76.10^{-2}$ L/min at 250 mg/L for the pseudo-first-order model. In a similar manner, the values of k_2 decrease from $53.39.10^{-3}$ g/mg min at a concentration of 20 mg/L to $2.500.10^{-3}$ g/mg min at a concentration of 250 mg/L. The observed decrease in rate constants with increasing initial concentration C_0 indicates slower adsorption kinetics at elevated concentrations, likely resulting from the saturation of available active sites [18]

Table III.3. Kinetic parameters for MB adsorption onto M-Bent at 25 ℃.

C_0	q_{exp}	Pseudo-first-order			Pseudo-second-order		
(mg/L)	(mg/g)	$K_1 \times 10^2$ (L/min)	q_{cal} (mg/g)	R^2	$K_2 \times 10^3$ (g/mg min)	q_{cal} (mg/g)	R^2
20	19.89	36.29	19.74	0.996	53.39	20.06	0.999
60	59.87	30.76	59.23	0.989	12.59	60.51	0.998
100	99.88	21.15	98.34	0.980	4.140	101.58	0.997
150	121.37	21.12	117.08	0.964	3.190	121.55	0.995
200	140.71	24.73	134.03	0.963	3.420	138. 64	0.992
250	163.09	21.76	156.25	0.967	2.500	162.02	0.996

The high determination coefficient (R^2) values, ranging from 0.989 to 0.999 as presented in Table III.4, indicate that the pseudo-second-order kinetic model effectively describes the adsorption of MB dye on MBent-A beads within the studied concentration range. The pseudo-first-order model demonstrated R^2 values between 0.984 and 0.994, suggesting a marginally less accurate fit to the experimental data. The rate constants k_1 and k_2 are significantly affected by the initial concentrations of MB dye. The k_1 values decline from $14.75.10^{-3}$ L/min at 15 mg/L to $9.80.10^{-3}$ L/min at 240 mg/L for the pseudo-first-order model. In the case of the pseudo-second-order model, the values of k_2 decrease from $13.80.10^{-4}$ g/mg min at a concentration of 15 mg/L to $0.555.10^{-4}$ g/mg min at 240 mg/L. The observed decrease in rate constants with increasing initial concentration (C_0) suggests a slower adsorption process at elevated concentrations, likely attributable to the diminished availability of active sites as saturation occurs [19].

Table III.4. Kinetic parameters for MB adsorption onto MBent-A beads composite at 25 ℃.

C_0	q_{exp}	Pseudo-first-order			Pseudo-second-order		
(mg/L)	(mg/g)	$K_1 \times 10^3$ (L/min)	q_{cal} (mg/g)	R^2	$K_2 \times 10^4$ (g/mg min)	q_{cal} (mg/g)	R^2
15	14.71	14.75	14.03	0.987	13.80	14.90	0.991
50	47.64	20.86	45. 67	0.984	6.303	48.08	0.999
100	92.34	23.44	89.71	0.984	3.838	93. 65	0.989
150	141.95	11.87	138.06	0.994	1.111	147.55	0.994
190	180.36	11.41	174.98	0.989	0.836	187.27	0.992
240	224.47	9.80	218.27	0.993	0.555	235.03	0.994

The adsorption of Methylene Blue (MB) onto M-Bent and MBent-A beads was examined using the intra-particle diffusion model, as seen in Figure III.9. Figure III.9 (a) illustrates the adsorption capacity Q_t as a function of the square root of time ($t^{0.5}$) for M-Bent at different starting MB concentrations, spanning from 20 to 250 mg/L. As the starting concentration rises, the adsorption capacity correspondingly increases. The curves demonstrate a multi-stage pattern, indicating that the adsorption process transpires in many stages. The plateau seen in the last phases of the curves indicates that adsorption equilibrium has been attained. Figure III.9 (b) illustrates the intra-particle diffusion of MB onto MBent-A beads at concentrations ranging from 15 to 240 mg/L. The adsorption process, similar to Figure III.9 (a), adheres to a multi-stage mechanism. In this instance, the adsorption capabilities are much greater than those of M-Bent, demonstrating that MBent-A beads possess enhanced adsorption efficacy. This indicates that MBent-A has a superior affinity for MB molecules, resulting in enhanced adsorption at equilibrium [20].

a)

b)
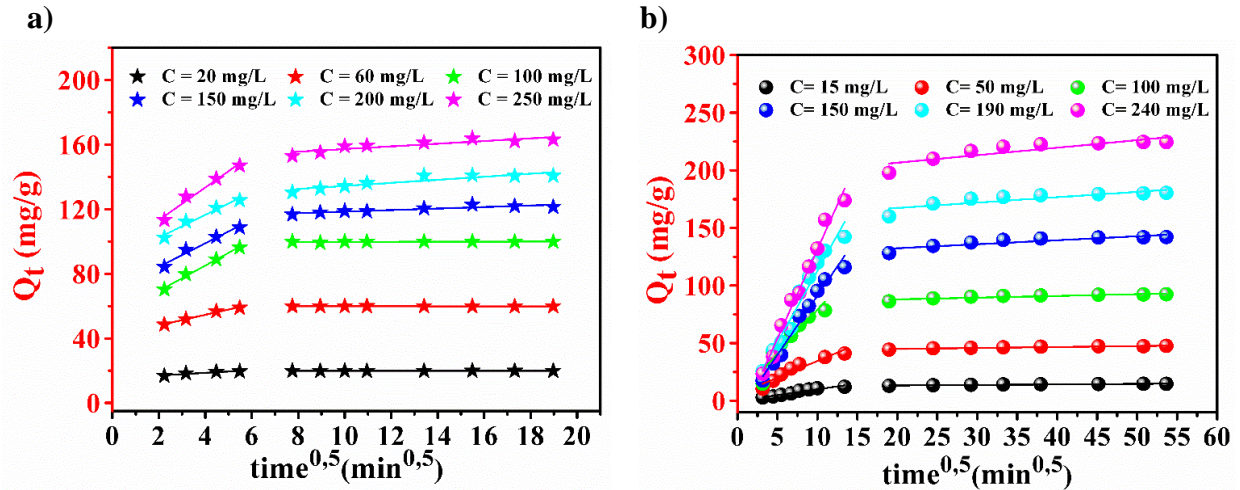
Figure III.9. plots of the intra-particle diffusion model on the MB adsorption onto (a) of M-Bent and (b) of MBent-A beads (V = 20 ml, W = 20 mg, T = 25 °C and stirring speed = 250rpm).

The plots of the intraparticle diffusion model, illustrated in Figure III.9 (a and b), demonstrated a non-linear segment throughout all time intervals, which can be categorized into two distinct stages. This result can be attributed to variations in mass transfer rates throughout the adsorption process. The initial stage indicates rapid adsorption attributed to the abundance of active sites, succeeded by a slower second stage, presumably influenced by the intraparticle diffusion of the adsorbate into the pores of the adsorbent. Table III.5, indicates that the values for kid1 exceed those of k_{id2}, and both k_{id1} and k_{id2} values rise with the initial concentration of MB on M-Bent. The observed result is due to the high availability of active sites at the onset of the adsorption process, resulting in a swift increase in adsorption during the initial phase.

Table III.5. Intraparticle diffusion parameters for MB adsorption onto M-Bent

C_0 (mg/L)	Intraparticle diffusion model					
Parameters	**Step 1**			**Step 2**		
	k_{id1}	C_{i1}	R^2	k_{id2}	C_{i2}	R^2
20	0.827	15.34	0.838	0.006	19.81	0.398
60	3.278	41.49	0.983	0.007	59.98	0.185
100	7.874	53.58	0.991	0.025	99.48	0.031
150	7.317	69. 62	0.961	0.471	113.8	0.785
200	7.043	88.30	0.957	0.947	124.9	0.793
250	10.11	93.04	0.961	0.825	149.0	0.752

Table III.6 also demonstrates a similar trend in the adsorption of MB onto MBent-A beads. The values for k_{id1} consistently exceed those of k_{id2}, with both exhibiting an increase corresponding to the initial concentration. The increased adsorption capacity observed may result from structural modifications in MBent-A beads, which enhance the accessibility of active sites and improve adsorption efficiency at elevated concentrations [21].

The rapid initial stage in both scenarios is associated with external surface adsorption, whereas the slower second stage pertains to intraparticle diffusion.

Table III.6. Intraparticle diffusion parameters for MB adsorption onto MBent-A beads composite.

C_0 (mg/L)	Intraparticle diffusion model					
Parameters	**Step 1**			**Step 2**		
	k_{id1}	C_{i1}	R^2	k_{id2}	C_{i2}	R^2
15	1.013	0.168	0.927	0.046	12.41	0.901
50	2.896	5.565	0.903	0.084	43.33	0.895
100	7.626	2.599	0.877	0.149	85.01	0.783
150	10.22	11.24	0.971	0.346	125.5	0.747
190	12.45	11.71	0.956	0.465	158.0	0.677
240	15.45	23.11	0.980	0.653	193.5	0.715

The findings validate that MBent-A beads has higher efficacy in MB removal owing to its improved diffusion properties and increased adsorption capacity at equilibrium.

III.3.6. Isotherm modeling

c)

d)
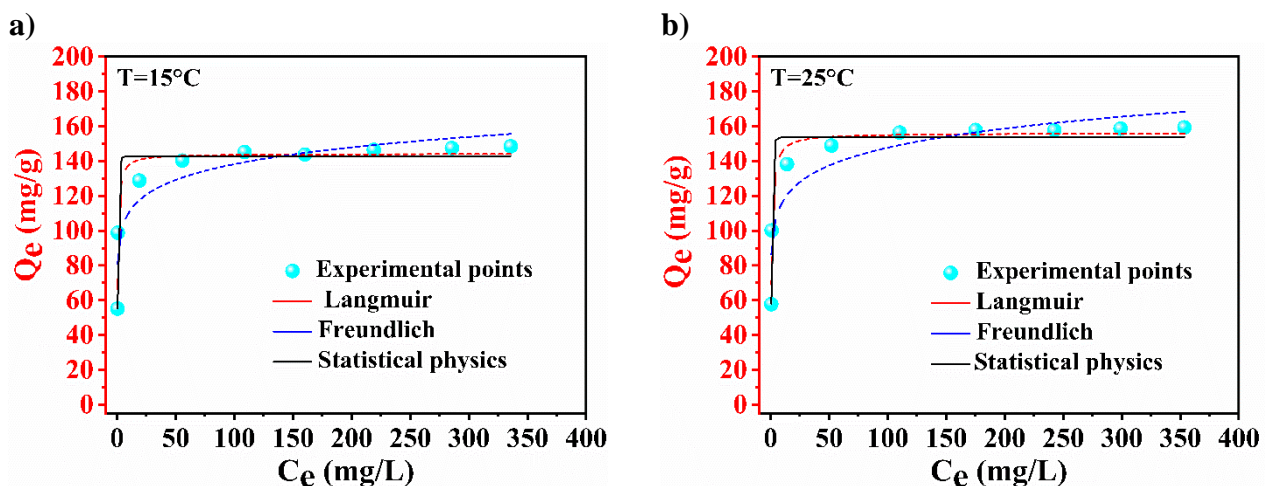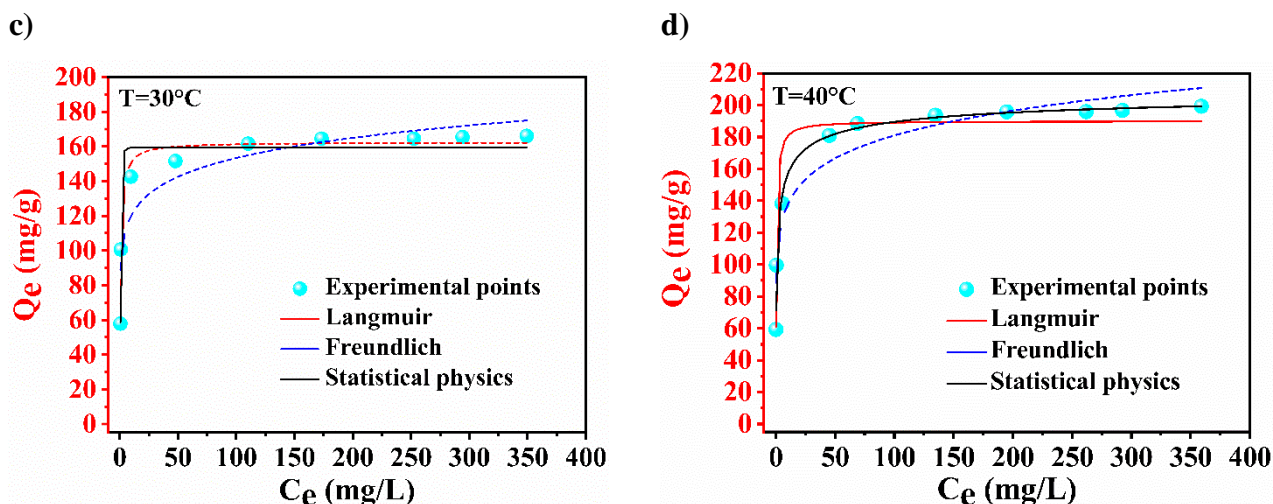
Figure III.10. Adsorption isotherms for MB adsorption onto M-Bent composite at 15, 25, 30, and 40 ℃ (V = 20 ml, W = 20 mg and stirring speed = 250rpm).

An analysis of the adsorption isotherms for M-Bent composite at temperatures of 15, 25, 30, and 40 °C provides insights into the interaction between the MB molecule and the adsorbent surface (Figure III.10). The experimental data were analyzed using the Langmuir and Freundlich models to elucidate the adsorption process under varying temperature conditions.

The Langmuir isotherm, which represents monolayer adsorption on a uniform surface, demonstrates a strong fit at all temperatures. The Langmuir maximum adsorption capacity q_m increases from 144.28 mg/g at 15 °C to 190.06 mg/g at 40 °C, as shown in Table III.7, demonstrating a significant enhancement in the adsorption capacity of the M-Bent composite with increasing temperature. The Langmuir constant K_L, while variable, indicates that the adsorption affinity remains relatively stable, with a significant increase observed at 40 °C. The R_L separation factor values, which range from 0.0009 to 0.013 across various temperatures, suggest that the adsorption process is favorable under all conditions. The Freundlich isotherm, representing multilayer adsorption on a heterogeneous surface, demonstrates a less accurate fit, especially at lower temperatures, as evidenced by the lower R² values relative to the Langmuir model. The Freundlich constant K_f increases with temperature, indicating a greater adsorption capacity at elevated temperatures. The 1/n values, consistently below 1 across all temperatures, indicate favorable adsorption; nonetheless, the Langmuir model is more effective in representing the overall adsorption behavior of MB onto the M-Bent composite.

Table III.7. Isotherms parameters for MB adsorption onto M-Bent
at 15, 25, 30 and 40 °C.

Models	Parameters	Temperatures			
		15 °C	**25 °C**	**30 °C**	**40 °C**
Langmuir	q_m (mg/g)	144.28	156.12	162.47	190.06
	K_L (L/mg)	2.132	1.396	1.304	1.884
	R^2	0.930	0.947	0.950	0.915
	R_L (Min-Max)	0.008 – 0.001	0.012 - 0.001	0.013- 0.002	0.009 – 0.0009
Freundlich	K_f ((mg/g) (L/ g)$^{1/n}$)	88.19	91.64	94.39	104.49
	$1/n$	0.098	0.104	0.105	0.119
	R^2	0.83	0.823	0.817	0.908
Statistic physics	N	2.337	2.419	2.467	0.463
	D_m (mg/g)	61.180	63.651	64. 674	460.09
	Nsat (mg/g)	142.98	153.97	159.55	213.02
	$C_{1/2}$ (mg/L)	0.4896	0.698	0.714	1.0999
	R^2	0.954	0.953	0.945	0.975

The analysis across varying temperatures elucidates the adsorption behavior of MB molecules onto the MBent composite, indicating that adsorption capacity enhances with rising temperature. The process is accurately represented by the Langmuir isotherm, suggesting predominant monolayer adsorption [22].

a)

b)

c)

d)
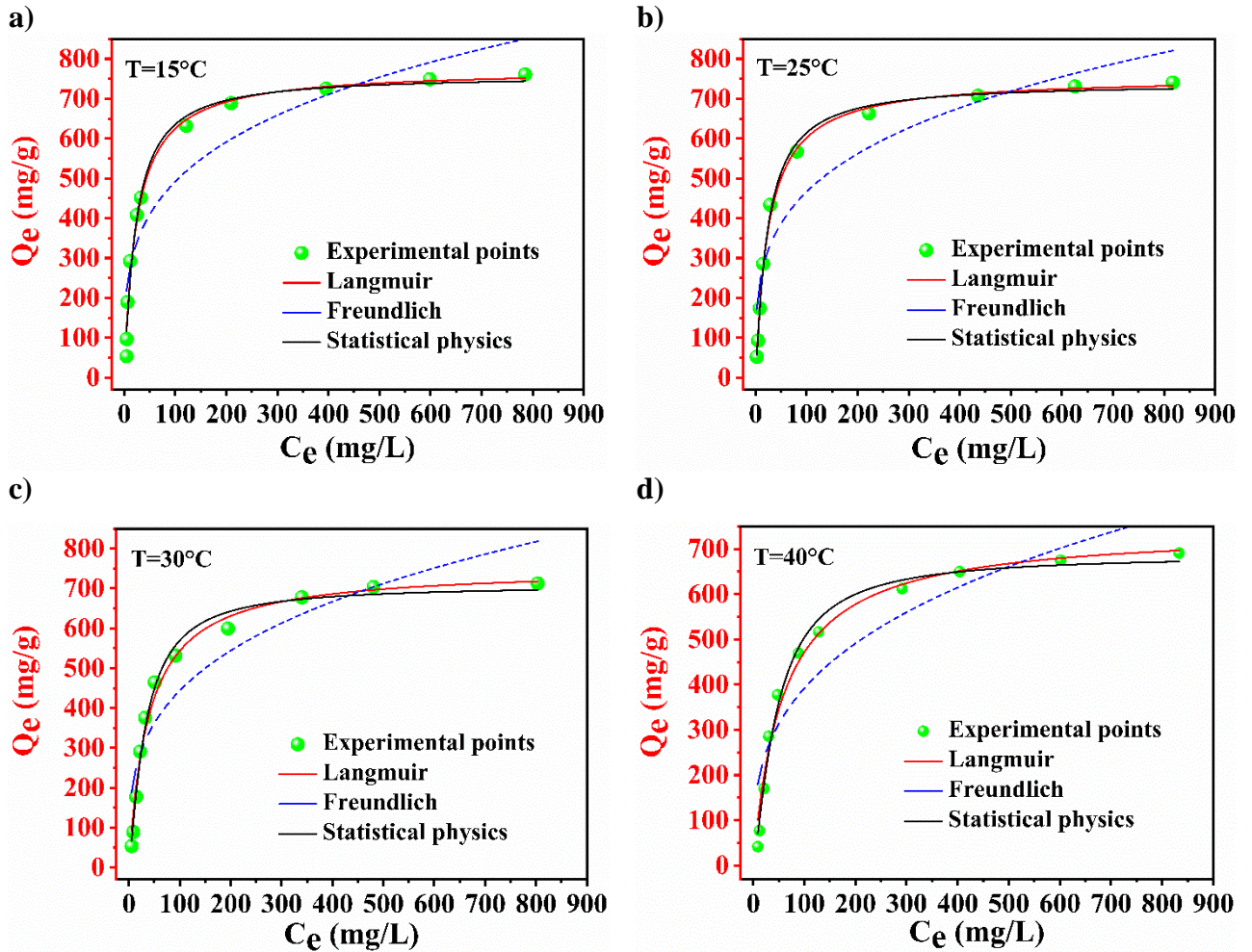
Figure III.11. Adsorption isotherms for MB adsorption onto MBent-A beads composite at 15, 25, 30, and 40 ℃ (V = 20 ml, W = 20 mg and stirring speed = 250rpm).

The examination of the adsorption isotherms for MB on MBent-A beads at temperatures of 15, 25, 30, and 40 °C (Figure III.11) elucidates the interaction between the MB molecule and the adsorbent surface. The experimental data were analyzed through the Langmuir and Freundlich models to elucidate the adsorption process at varying temperatures. The Langmuir isotherm, which characterizes monolayer adsorption on a uniform surface, demonstrates a robust fit across all temperatures. Table III.8 illustrates that the Langmuir maximum adsorption capacity, q_m, exhibits a slight decrease with rising temperature, from 774.32 mg/g at 15 °C to 745.25 mg/g at 40 °C, indicating a minor reduction in adsorption efficiency as temperature increases. The Langmuir constant K_L demonstrates a decreasing affinity with increasing temperature, varying from 0.0419 L/mg at 15 °C to 0.0172 L/mg at 40 °C. The R_L separation factor values range from 0.015 to 0.534 across the temperatures, suggesting that the adsorption process is favorable under all tested conditions. Conversely, the Freundlich

70

isotherm, indicative of multilayer adsorption on a heterogeneous surface, demonstrates a poorer fit, as shown by lower R^2 values relative to the Langmuir model, especially at reduced temperatures. Table III.8 illustrates that the Freundlich constant K_f decreases from 145.12 mg/g at 15 °C to 87.912 mg/g at 40 °C. The 1/n values, remaining below 1 at all temperatures, indicate that adsorption is favorable.

Table III.8. Isotherms parameters for MB adsorption onto MBent-A beads at 15, 25, 30 and 40 °C.

Models	Parameters	Temperatures			
		15 °C	**25 °C**	**30 °C**	**40 °C**
Langmuir	q_m (mg/g)	774.32	755.17	751.89	745.25
	K_L(L/mg)	0.0419	0.0394	0.0261	0.0172
	R^2	0.986	0.995	0.985	0.980
	R_L (Min-Max)	0.015 - 0.292	0.016 - 0.317	0.025 - 0.393	0.037 - 0.534
Freundlich	K_f ((mg/g) (L/ g)$^{1/n}$)	145.12	135.05	114.84	87.912
	1/n	0.2652	0.269	0.294	0.325
	R^2	0.866	0.879	0.852	0.859
Statistic physics	N	1.089	1.103	1.254	1.322
	D_m (mg/g)	697.76	670. 62	564.92	519. 639
	Nsat (mg/g)	757.77	739. 69	708.41	686.96
	$C_{1/2}$ (mg/L)	22.23	23.53	32.41	46.397
	R^2	0.985	0.997	0.989	0.988

The Langmuir model more accurately represents the overall adsorption behavior of MB on MBent-A beads, particularly at elevated temperatures.

III.3.7. Statistical physics model

The examination of adsorption isotherms for MB on MBent and MBent-A beads through the statistical physics model provides significant insights into the interaction between MB molecules and the adsorbent surface.

The statistical physics model for MBent indicates that the maximum adsorption density D_m increases from 61.18 mg/g at 15 °C to 64.674 mg/g at 30 °C, followed by a significant rise to 460.09 mg/g at 40 °C. The saturation number N_{sat} increases from 142.98 mg/g to 213.02 mg/g with temperature, signifying enhanced adsorption capacity. The $C_{1/2}$ value, indicative of the concentration required to occupy half of the adsorption sites, rises from 0.4896 mg/L at 15 °C to 1.0999 mg/L at 40 °C, demonstrating that increased concentrations are necessary at higher temperatures. The quantity of adsorption sites per molecule N is consistent from 15 °C to 30 °C, but showing a significant decline at 40 °C. The R^2 values, ranging from 0.945 to 0.975, indicate a strong model fit [23].

The maximum adsorption density D_m declines from 697.76 mg/g at lower temperatures to 519.639 mg/g at higher temperatures, suggesting a diminished capacity for MB adsorption with increasing temperature. The saturation number N_{sat} decreases from 757.77 mg/g to 686.96 mg/g, indicating a reduction in adsorption capacity. The $C^{1/2}$ values exhibit a notable increase from 22.23 mg/L to 46.397 mg/L, indicating that greater concentrations of MB are required to occupy half of the adsorption sites at higher temperatures. The model demonstrates robustness, as evidenced by R^2 values between 0.985 and 0.997, which indicate a strong correlation with the experimental data. This analysis highlights the intricate relationship between temperature and MB adsorption on M-Bent-A beads, providing critical insights for the optimization of adsorption processes.

III.3.8. Regeneration study

The regeneration and reuse of adsorbents are critical in adsorption processes, providing both economic and environmental advantages across various applications [24]. Over time, adsorbents can become saturated with adsorbates, leading to a reduction in their adsorption capacity. Regeneration involves the removal of adsorbates from the adsorbent's surface, restoring its effectiveness and extending its lifespan. Various regeneration methods are used for this purpose [25]. Figure III.12 shows promising results, demonstrating that MBent-A beads can be reused over five cycles, with efficiency decreasing only slightly from 98.54 % to 90.60 %, indicating their notable cost-effectiveness.
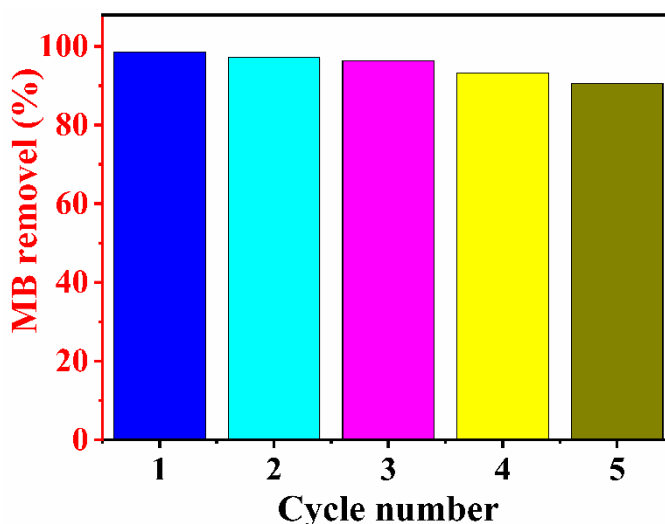
Figure III.12. Regeneration of MBent-A beads composite after adsorption of MB (initial MB dye concentration = 100 mg/L, T = 25 ℃, V = 50 mL, W = 50 mg and stirring speed = 250 rpm).

III.4. Molecular modeling computations

For example, we conducted molecular modeling to investigate the adsorption of methylene blue (MB) onto magnetic bentonite beads. By applying density functional theory (DFT) and the Atoms in Molecules (AIM) approach alongside other computational methods, this combined theoretical and experimental framework enabled a comprehensive interpretation of the data, refining and validating the proposed concepts.

To assess the reactivity and electronic properties of the MB molecule, we analyzed Frontier Molecular Orbitals (FMO), Molecular Electrostatic Potential (MEP), and Mulliken charge distribution. This evaluation was based on the energy levels of the Highest Occupied Molecular Orbital (HOMO) and the Lowest Unoccupied Molecular Orbital (LUMO).

Additionally, we performed Reduced Density Gradient (RDG) and Quantum Theory of Atoms in Molecules (QTAIM) analyses to explore non-covalent interactions and the underlying mechanism governing the interaction between MB and the adsorbent. The QTAIM analysis provided valuable insights into these interactions, clarifying the nature and strength of the intermolecular forces involved. This significantly deepened our fundamental understanding of intermolecular interactions within the system.

III.4.1. Optimized structures and FMO analysis

III.4.1.1. Methylene Bleu Dye

In this investigation, DFT calculations have been performed to unravel the intricate interplay between the removal of the cationic dye MB and its molecular structure and its adsorption onto the surface of the composite material. Our exploration commenced by subjecting the MB dye to a comprehensive quantum analysis, focusing on its electronic properties. Figure III.13 illustrates key aspects, including (a) the Highest Occupied Molecular Orbital (HOMO) and Lowest Unoccupied Molecular Orbital (LUMO) orbitals, (b) molecular electrostatic potential maps, and ((c) and (d)) Mulliken atomic charge maps with associated distributions.

The MB molecule, known for its preference towards high-energy conformers, highlights its predominantly polar organic nature. This heightened polarization index is a crucial contributor to the exceptional efficiency observed in MB removal through biosorption [26,27].

Delving into molecular electronic properties, the spotlight is on the HOMO and LUMO orbitals. The energy values of HOMO (E_{HOMO}) and LUMO (E_{LUMO}) play pivotal roles, conveying the molecule's ability to donate or accept electrons. Higher E_{HOMO} values indicate a greater propensity for electron donation, while lower E_{LUMO} values signify reduced receptiveness. The chemical stability of MB is intricately linked to its energy gap (E_g), representing the difference between HOMO and LUMO energy levels. A relatively narrow E_g of 2.428 eV emphasizes MB's high reactivity, rendering it exceptionally amenable to adsorption on a substrate's surface [26].
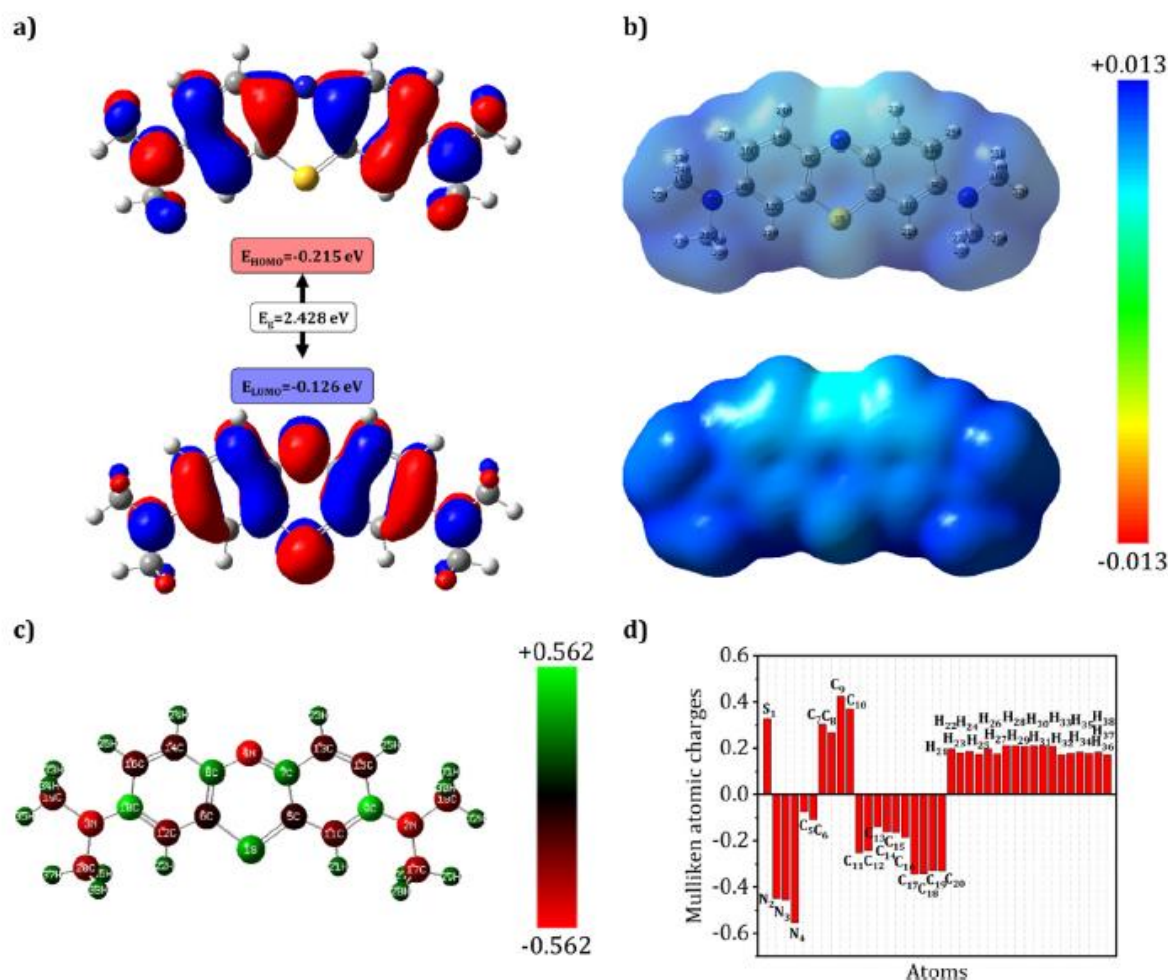
Figure III.13. LUMO, HOMO orbitals (a), Molecular electrostatic potential maps (b), and Mulliken charges distributions (c and d) of the MB dye molecule.

Figure III.13 (a) provides a detailed exploration of HOMO and LUMO orbitals, revealing a distribution pattern across the molecular structure. This distribution, influenced by lone electron pairs at the nitrogen atom and delocalized π electrons within phenyl groups, signifies an electron conjugation effect. Figure III.13 (b) showcases the electrophilic reactivity of the MB cationic dye through a blue (positive) field, indicating its ability to interact with bioadsorbent surfaces by sharing free electrons. Examining Mulliken atomic charges in Figure III.13 ((c) and (d)), N heteroatoms within the MB molecule emerge as primary centers of negativity, underscoring their pivotal role in the adsorption and retention processes during MB remediation.

75

III.4.1.2. MB adsorption system onto composite's surface

In Figure III.14 (a), a visually compelling representation unveils the optimized adsorption system featuring MBent-A beads, a composite comprising a bentonite@Fe_3O_4@Alginate complex with MB dye molecules. Employing the DFT M06-2X functional and TZVP basis set, this representation provides meticulous insight into the dynamic interaction between MB and the diverse components of the adsorbent.

The theoretical exploration of the adsorption process is noteworthy, reinforcing that the MB adsorption system exhibits a highly promising configuration for efficient adsorption. Furthermore, Figure III.14 (b) enhances our comprehension of the MB adsorption system by presenting a 3D molecular structure coupled with charge density distributions. In this detailed visualization, the red region denotes negative "hydrogen acceptor" surfaces, the blue area signifies positive "hydrogen donor" surfaces, and the green region represents neutral "non-polar" system surfaces. These charge density distributions are pivotal in designing efficient adsorption systems, especially for applications like wastewater treatment. It is crucial to note that the MB molecule can manifest in various forms within the adsorption system. It can be attached to alginate, bound to Fe_3O_4 nanoparticles, or affixed to the bentonite surface. This versatility in attachment modes further accentuates the adaptability and potential applications of the MB adsorption system. Beyond advancing our understanding of adsorption processes, these findings hold significant promise for developing practical and efficient adsorption systems across various applications. Essentially, this analysis not only deepens our comprehension of the electronic properties of the MB molecule, showcasing its versatility as both an electron donor and acceptor with heightened reactivity, but also positions it as an excellent candidate for adsorption on diverse surfaces. This includes those utilized in biocomposite-based adsorption systems, providing a solid foundation for advancing the field and addressing real-world challenges.
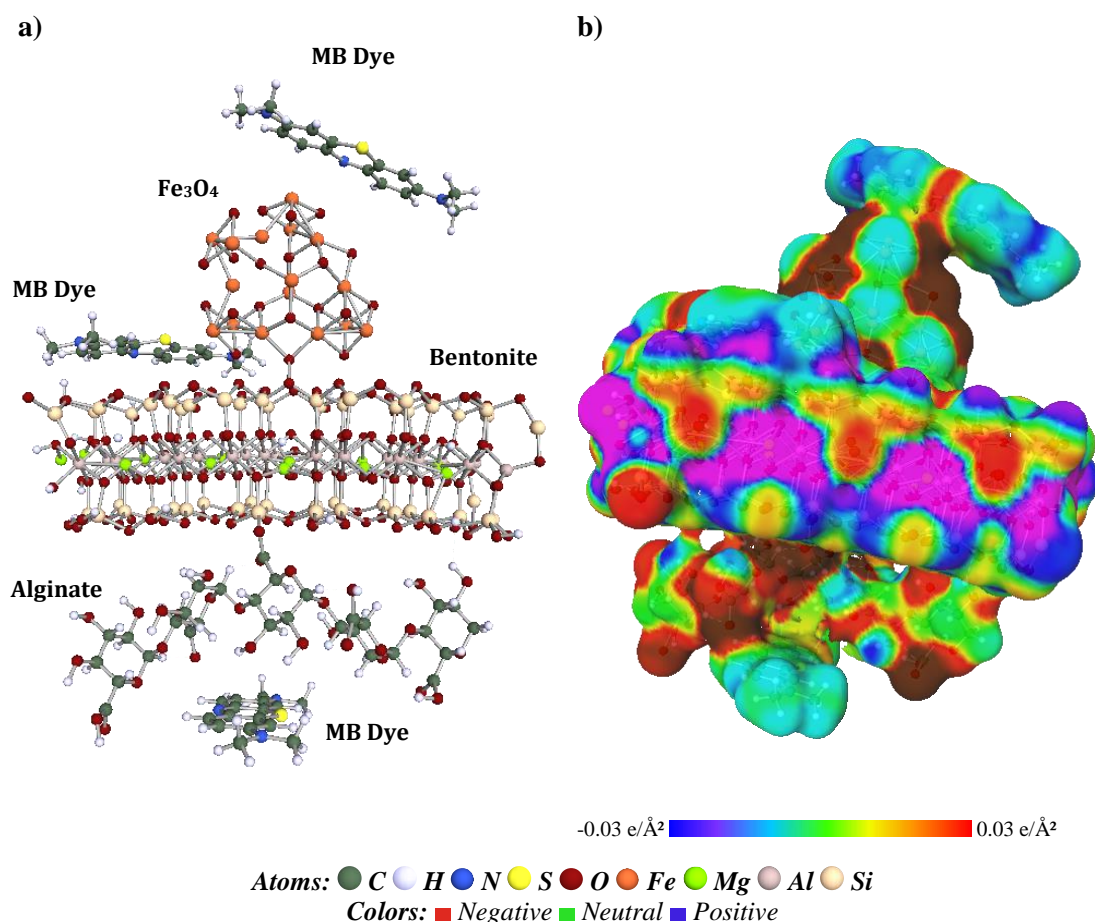
Figure III.14. The optimized structure (a), COSMO-RS charge distribution (b) of the adsorption system of MB dye onto the composite's surface.

III.4.2. Non-covalent interaction (NCI) analysis

In Figure III.15, we present an insightful Non-covalent Interaction (NCI) analysis of the MB dye (Figure III.15 (a)) and the adsorbed MB on the adsorption system (Figure III.15 (b)). This analysis employs the reduced density gradient (RDG), a function of sign $\lambda_2 \times \rho$, where ρ represents electron density and λ_2 corresponds to the largest eigenvalue of the Hessian matrix, providing a nuanced understanding of electron density variations near critical points [28,29]. The color-coded regions in the analysis offer invaluable insights into the non-covalent interactions governing the MB molecule's interaction with the adsorbent material. The green regions in the analysis represent van der Waals (VDW) interactions, known for their relatively weak but widespread influence across the system and characterized by low electron densities. Simultaneously, red regions denote repulsive interactions primarily localized within cyclic structures, originating from steric effects. These repulsive forces result from clashes in

molecular configurations due to spatial constraints, with steric effects playing a minor role compared to VDW interactions [30–32].

a) Methylene Bleu

b) Adsorption System
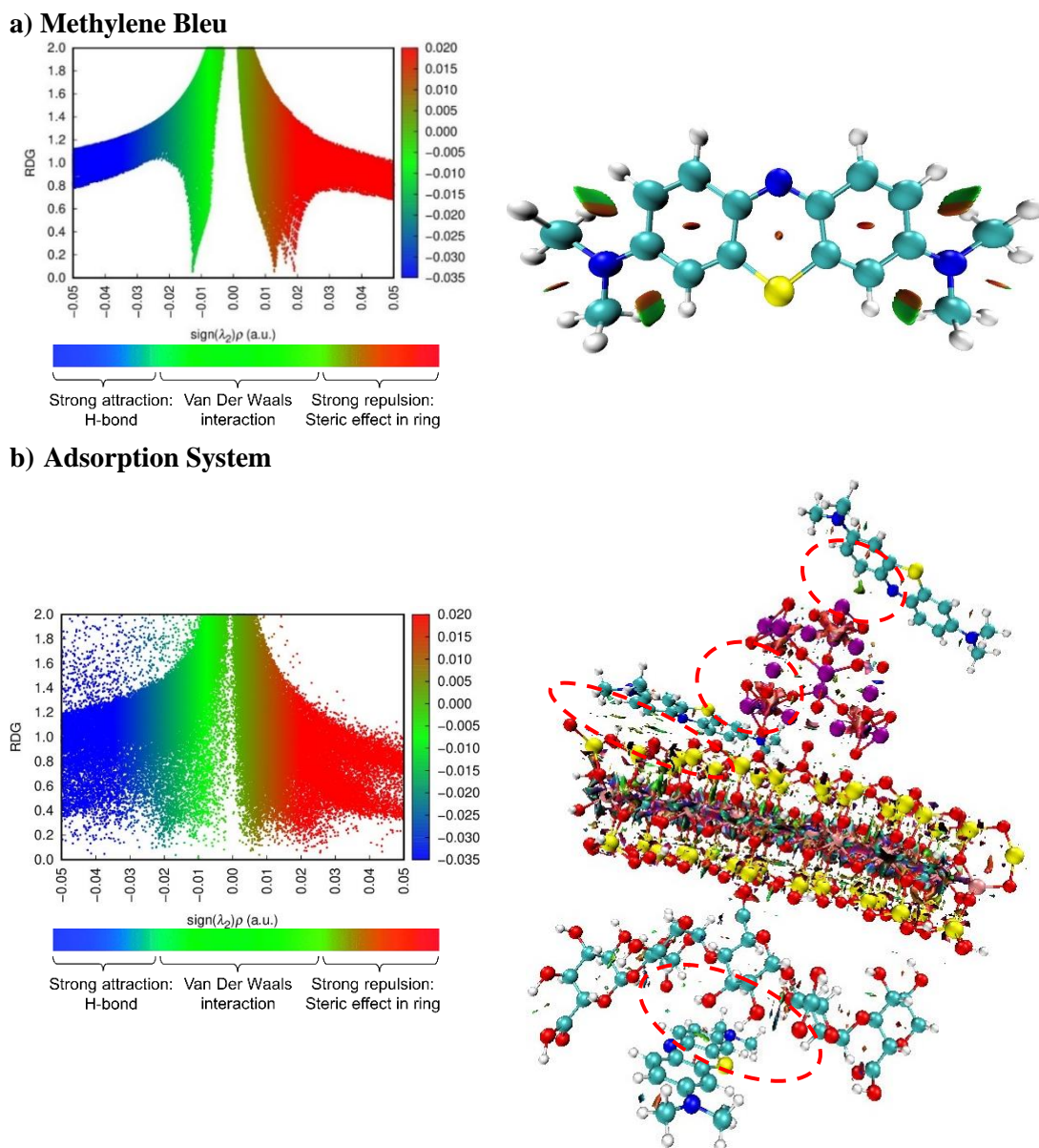
Figure III.15.   The RDG scatter plots (upper) and NCI plots (bottom) isosurface (s = 0.5 a.u.) of MB dye (a) and the adsorbed MB dye onto composite's surface (b).

Figure III.15 (b) vividly illustrates the intriguing blue spots in our NCI analysis, indicative of hydrogen bonding—a phenomenon recognized for its robust interactions characterized by high electron density. Remarkably, at an RDG level of 0.5, these distinct blue spots underscore the occurrence of hydrogen bonding forces during the MB adsorption onto the adsorbent material. This critical observation accentuates the significance of hydrogen bonding in the complex dynamics of MB adsorption. Crucially, it is imperative to emphasize the

diverse forms of attachment that the MB molecule exhibits within the adsorption system. Whether tethered to alginate, bonded to Fe_3O_4 nanoparticles, or adhered to the bentonite surface, each distinct form of attachment contributes to the nuanced nature of non-covalent interactions. This multi-faceted attachment framework introduces an additional layer of complexity to our NCI analysis, enriching our understanding of the intricate intermolecular forces. Our exhaustive RDG analysis yields a compelling conclusion—despite their relatively weaker nature, VDW forces and H-bonding dominate the MB adsorption process on the adsorbent. This underscores the paramount importance of VDW interactions in this system, with steric effects playing a comparatively minor role.

Consequently, our NCI analysis unveils a clear and nuanced portrayal of the MB adsorption process. Predominantly governed by VDW interactions, with steric effects assuming a minor role, and the appearance of H-bonding forces at the RDG level of 0.5, these findings provide invaluable insights into the driving forces orchestrating the MB adsorption process. This contribution significantly deepens our understanding of the intricate interactions dictating the success of MB adsorption, opening avenues for breakthroughs in designing highly effective adsorption systems tailored for wastewater treatment applications.

III.4.3. Quantum theory of atoms in molecules (QTAIM) analysis

The QTAIM analysis, visually represented in Figure III.16 and presented comprehensively in Table III.9 unveils the intricate nature of chemical bonds formed during the interaction of MB with the MBent-A beads adsorbent represented by Fe_3O_4@Bentonite@Alginate composite. This analysis serves as a crucial tool for dissecting the strengths and characteristics of these bonds, offering a nuanced perspective on each MB interaction segment. Notably, the QTAIM results bring forth the inherent diversity in the strength of chemical bonds, showcasing unique features such as differences in electron density and Laplacian values. Understanding the strength of a bond is pivotal for comprehending its behavior, and the metrics provided in Table III.9 offer valuable insights into this aspect. This novel visualization method effectively captures interactions, including H-bonding and VdW forces, between the MB dye molecules and the surface of MBent-A beads.

Adsorption system

Keys: • *Bond CPs* • *Ring CPs* • *Cage CPs*
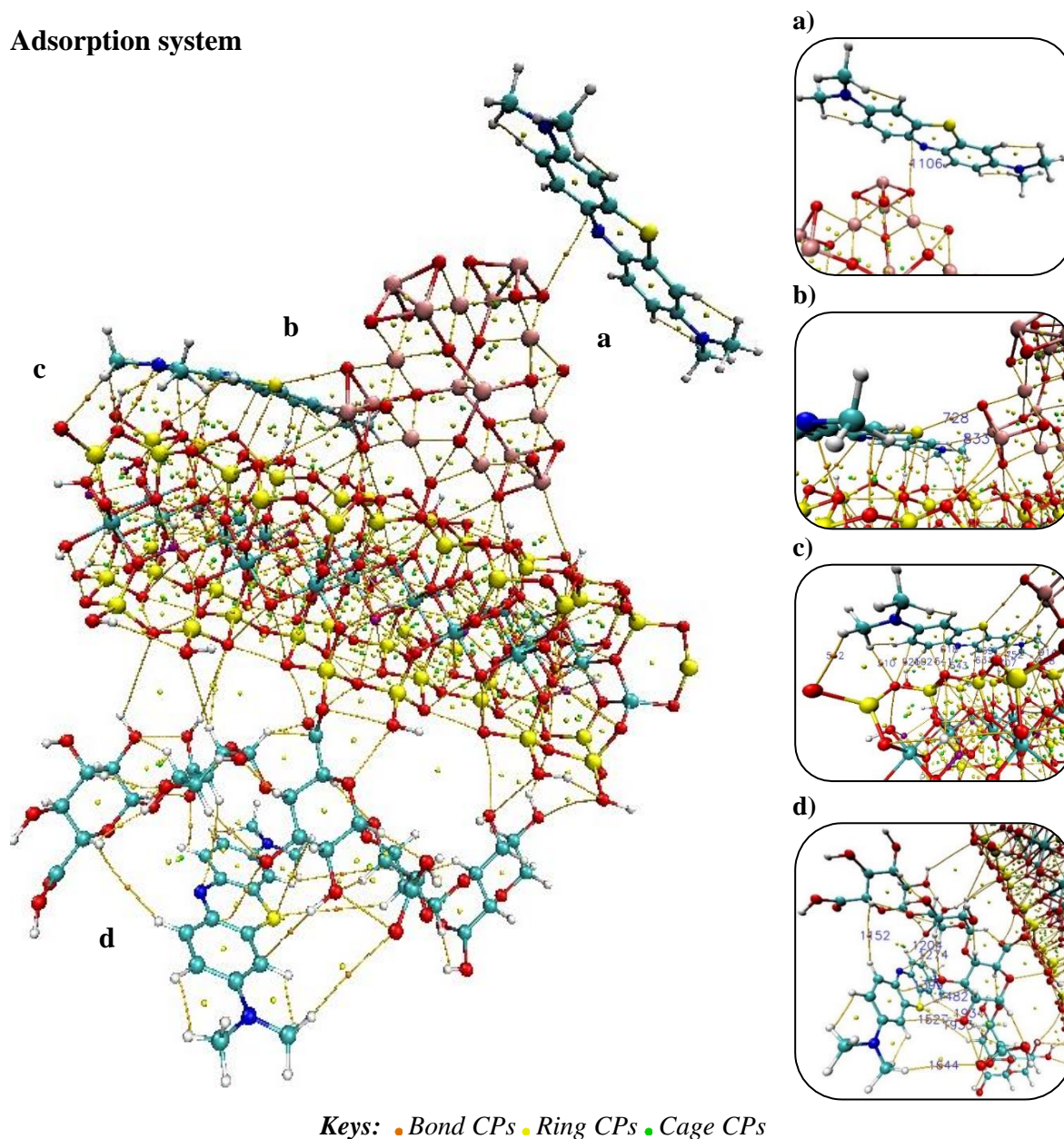
Figure III.16. Molecular graphical representation using QTAIM for the adsorption of MB Dye system onto the composite surface.

Analyzing Figure III.16 and delving into the details presented in Table III.9, a granular insight emerges into the topological characteristics of interaction sites at selected Bond Critical Points (BCPs) within the MB adsorption system on the composite. In the MB@Fe_3O_4 segment (Figure III.16 (a and b)), specific BCPs involving S, O, and Fe exhibit distinct characteristics. The negative values of $\nabla^2\rho(r)$ and $|V(r)|/G(r)$ suggest attractive forces, while positive values of $V(r)$ and $H(r)$ signify predominantly closed-shell interactions. This observation provides a detailed understanding of the forces governing the MB@Fe_3O_4

interaction, crucial for assessing its stability and efficiency. Figure III.16 (c) sheds light on the MB@Bentonite section, where hydrogen (H), carbon (C), and silicon (Si) BCPs reveal intricate intermolecular characteristics. Pronounced negative values in $\nabla^2\rho(r)$ and $|V(r)|/G(r)$ indicate attractive forces, with the presence of hydrogen bonding at specific BCPs, such as 928(H) -- 455(H) and 603(Si) -- 40(O), evident from large negative H(r) values. Moving on to the MB@Alginate interactions showcased in Figure III.16 (d), a spectrum of interactions involving H, O, N, C, and S BCPs is observed. Negative $\nabla^2\rho(r)$ and $|V(r)|/G(r)$ values indicate attractive forces, with notable hydrogen bonding at BCPs 1204(O) -- 363(O) and 631(C) -- 430(C). The negative values in H(r) emphasize closed-shell interactions, contributing significantly to the stability of the adsorption system [32,33].

Table III.9. Topological features of interaction sites (in atomic units) at selected bond critical points (BCPs).

BCP	X − Y	$\rho(r)$	$\nabla^2\rho(r)$	V(r)	G(r)	|V(r)|/G(r)	H(r)
			MB@Fe₃O₄				
728	423(S) -- 268(O)	0.005601	0.018387	-0.003350	0.003973	0.843107	0.000623
833	444(H) -- 260(Fe)	0.002207	0.007255	-0.001266	0.001540	0.821948	0.000274
1106	467(C) -- 249(O)	0.003256	0.012012	-0.001516	0.002260	0.671026	0.000743
			MB@Bentonite				
928	455(H) -- 247(H)	0.031459	0.063783	-0.023821	0.019883	1.198036	**-0.003938**
914	459(H) -- 142(O)	0.018226	0.061577	-0.015054	0.015224	0.988812	0.000170
752	434(C) -- 198(O)	0.012581	0.042090	-0.008656	0.009589	0.902668	0.000933
691	423(S) -- 72(O)	0.009106	0.027834	-0.006571	0.006765	0.971327	0.000194
707	438(C) -- 237(H)	0.017476	0.052136	-0.011157	0.012095	0.922402	0.000939
603	66(Si) -- 40(O)	0.076577	0.245381	-0.109579	0.085462	1.282196	**-0.024117**
502	235(H) -- 445(H)	0.008960	0.033613	-0.005434	0.006918	0.785383	0.001485
541	435(C) -- 124(O)	0.012362	0.043106	-0.008771	0.009774	0.897375	0.001003
510	449(H) -- 138(O)	0.012273	0.040888	-0.009771	0.009997	0.977456	0.000225
512	53(O) -- 451(H)	0.012748	0.039103	-0.009876	0.009826	1.005117	**-0.000050**
			MB@Alginate				
1152	365(H) -- 407(H)	0.000463	0.001486	-0.000122	0.000247	0.493517	0.000125
1204	363(O) -- 408(H)	0.014124	0.055922	-0.010878	0.012429	0.875172	0.001552
1274	345(H) -- 388(N)	0.000964	0.003477	-0.000339	0.000604	0.560781	0.000265
1399	391(C) -- 336(O)	0.002561	0.009905	-0.001364	0.001920	0.710459	0.000556
1482	335(H) -- 385(S)	0.000396	0.001645	-0.000154	0.000283	0.544524	0.000129
1527	395(C) -- 333(H)	0.001523	0.005762	-0.000638	0.001039	0.613813	0.000401
1644	415(H) -- 324(O)	0.000214	0.001268	-0.000045	0.000181	0.247028	0.000136
1933	385(S) -- 311(H)	0.000224	0.000964	-0.000071	0.000156	0.455060	0.000085
1934	406(H) -- 313(H)	0.000015	0.000062	-0.000004	0.000010	0.447590	0.000006
521	437(C) -- 138(O)	0.006683	0.022938	-0.004014	0.004874	0.823495	0.000860
618	433(C) -- 43(O)	0.008604	0.025419	-0.005471	0.005913	0.925255	0.000442
543	135(O) -- 426(N)	0.002223	0.010544	-0.001324	0.001980	0.668868	0.000656
631	430(C) -- 40(O)	0.017083	0.068471	-0.013119	0.015118	0.867736	0.002000

Therefore, QTAIM analysis elucidates the bonding dynamics in the MB adsorption system on MBent-A beads, highlighting the presence of hydrogen bonding, attractive forces,

and closed-shell interactions at critical points. These findings deepen our understanding of the adsorption mechanism, underpinning the system's stability and efficiency, especially for wastewater treatment applications.

III.5. Conclusion

In this chapter, we studied the adsorption of methylene blue (MB) onto magnetic bentonite (M-Bent) and magnetic bentonite beads (MBent-A). The first part focused on characterizing both adsorbents using techniques such as FTIR, X-ray diffraction (XRD), scanning electron microscopy (SEM/EDS), and the determination of the point of zero charge (pHpzc) to better understand their textural and physicochemical properties.

The second part examined the adsorption parameters, including the effects of pH, adsorbent dosage, temperature, and initial concentration. Adsorption on M-Bent was found to be endothermic and spontaneous, while adsorption on MBent-A was exothermic but still spontaneous. The adsorption capacity increased with higher initial concentrations of MB, but equilibrium was reached more slowly at elevated concentrations due to the saturation of active sites. The pseudo-second-order kinetic model fitted well for both adsorbents, while Langmuir isotherm analysis confirmed uniform monolayer adsorption. Emphasizing the economic feasibility and environmental friendliness of adsorption-based processes, the study underscores the importance of regenerating adsorbents and their reusability.

This study integrates experimental and theoretical methods to elucidate the adsorption mechanisms of MBent-A beads, highlighting the key role of VdW forces and H-bonding in methylene blue adsorption. Theoretical analyses (DFT, FMO, RDG, QTAIM, NCI) confirm these interactions, enhancing adsorption efficiency and material stability. These findings pave the way for improved adsorbents in wastewater treatment and sustainable environmental solutions.

References

[1] Y. Turhan, Z.G. Alp, M. Alkan, M. Doğan, Preparation and characterization of poly(vinylalcohol)/modified bentonite nanocomposites, Microporous Mesoporous Mater. 174 (2013) 144–153. https://doi.org/10.1016/j.micromeso.2013.03.002.

[2] F.Y. Zhao, Y.L. Li, L.H. Li, Preparation and characterization of magnetite nanoparticles, Appl. Mech. Mater. 618 (2014) 24–27. https://doi.org/10.4028/www.scientific.net/AMM.618.24.

[3] M. Yamaura, R.L. Camilo, L.C. Sampaio, M.A. Macêdo, M. Nakamura, H.E. Toma, Preparation and characterization of (3-aminopropyl)triethoxysilane-coated magnetite nanoparticles, J. Magn. Magn. Mater. 279 (2004) 210–217. https://doi.org/10.1016/j.jmmm.2004.01.094.

[4] A. Mohammadi, H. Abdolvand, A.P. Isfahani, Alginate beads impregnated with sulfonate containing calix[4]arene-intercalated layered double hydroxides: In situ preparation, characterization and methylene blue adsorption studies, Int. J. Biol. Macromol. 146 (2020) 89–98. https://doi.org/10.1016/j.ijbiomac.2019.12.229.

[5] R.S. Hebbar, A.M. Isloor, B. Prabhu, Inamuddin, A.M. Asiri, A.F. Ismail, Removal of metal ions and humic acids through polyetherimide membrane with grafted bentonite clay, Sci. Rep. 8 (2018). https://doi.org/10.1038/s41598-018-22837-1.

[6] T.J. Gilberto, L. Marçal, J.M. Silva, L.A. Rocha, K.J. Ciuffi, E.H. Faria, E.J. Nassar, Hybrid materials based on bentonite functionalized with amine groups via the hydrolytic sol-gel method, J. Braz. Chem. Soc. 27 (2016) 933–940. https://doi.org/10.5935/0103-5053.20150348.

[7] Z. Wang, J. Xu, Y. Hu, H. Zhao, J. Zhou, Y. Liu, Z. Lou, X. Xu, Functional nanomaterials: Study on aqueous Hg(II) adsorption by magnetic Fe3O4@SiO2-SH nanoparticles, J. Taiwan Inst. Chem. Eng. 60 (2016) 394–402. https://doi.org/10.1016/j.jtice.2015.10.041.

[8] Z. Lou, Z. Zhou, W. Zhang, X. Zhang, X. Hu, P. Liu, H. Zhang, Magnetized bentonite by Fe3O4 nanoparticles treated as adsorbent for methylene blue removal from aqueous solution: Synthesis, characterization, mechanism, kinetics and regeneration, J. Taiwan Inst. Chem. Eng. 49 (2015) 199–205. https://doi.org/10.1016/j.jtice.2014.11.007.

[9] A. Dąbrowski, Adsorption - From theory to practice, Adv. Colloid Interface Sci. 93 (2001) 135–224. https://doi.org/10.1016/S0001-8686(00)00082-8.

[10] L.C.A. Oliveira, D.I. Petkowicz, A. Smaniotto, S.B.C. Pergher, Magnetic zeolites: A

new adsorbent for removal of metallic contaminants from water, Water Res. 38 (2004) 3699–3704. https://doi.org/10.1016/j.watres.2004.06.008.

[11] A. Sari, M. Tuzen, Biosorption of cadmium(II) from aqueous solution by red algae (Ceramium virgatum): Equilibrium, kinetic and thermodynamic studies, J. Hazard. Mater. 157 (2008) 448–454. https://doi.org/10.1016/j.jhazmat.2008.01.008.

[12] N.G. Turan, B. Mesci, O. Ozgonenel, The use of artificial neural networks (ANN) for modeling of adsorption of Cu(II) from industrial leachate by pumice, Chem. Eng. J. 171 (2011) 1091–1097. https://doi.org/10.1016/j.cej.2011.05.005.

[13] A.S. Sartape, A.M. Mandhare, V. V. Jadhav, P.D. Raut, M.A. Anuse, S.S. Kolekar, Removal of malachite green dye from aqueous solution with adsorption technique using Limonia acidissima (wood apple) shell as low cost adsorbent, Arab. J. Chem. 10 (2017) S3229–S3238. https://doi.org/10.1016/j.arabjc.2013.12.019.

[14] A. Nasrullah, A.H. Bhat, A. Naeem, M.H. Isa, M. Danish, High surface area mesoporous activated carbon-alginate beads for efficient removal of methylene blue, Int. J. Biol. Macromol. 107 (2018) 1792–1799. https://doi.org/10.1016/j.ijbiomac.2017.10.045.

[15] A.A. Abd, S.Z. Naji, A.S. Hashim, M.R. Othman, Carbon dioxide removal through physical adsorption using carbonaceous and non-carbonaceous adsorbents: A review, J. Environ. Chem. Eng. 8 (2020) 104142. https://doi.org/10.1016/j.jece.2020.104142.

[16] J. Fu, Z. Chen, M. Wang, S. Liu, J. Zhang, J. Zhang, R. Han, Q. Xu, Adsorption of methylene blue by a high-efficiency adsorbent (polydopamine microspheres): Kinetics, isotherm, thermodynamics and mechanism analysis, Chem. Eng. J. 259 (2015) 53–61. https://doi.org/10.1016/j.cej.2014.07.101.

[17] T.N. Chikwe, R.E. Ekpo, I. Okoye, Competitive Adsorption of Organic Solvents Using Modified and Unmodified Calcium Bentonite Clay Mineral, Chem. Int. 4 (2018) 230–239.

[18] J.P. Simonin, On the comparison of pseudo-first order and pseudo-second order rate laws in the modeling of adsorption kinetics, Chem. Eng. J. 300 (2016) 254–263. https://doi.org/10.1016/j.cej.2016.04.079.

[19] M.A.U.R. Al-Kazragi, D.T.A. Al-Heetimi, Pretreated Fishbone as Low Cost-Adsorbent for Cationic Dye Adsorption from Aqueous Solutions: Equilibrium, Optimization, Kinetic and Thermodynamic Study, J. Phys. Conf. Ser. 1879 (2021). https://doi.org/10.1088/1742-6596/1879/2/022073.

[20] A. Benhouria, M.A. Islam, H. Zaghouane-Boudiaf, M. Boutahala, B.H. Hameed,

Calcium alginate-bentonite-activated carbon composite beads as highly effective adsorbent for methylene blue, Chem. Eng. J. 270 (2015) 621–630. https://doi.org/10.1016/j.cej.2015.02.030.

[21] C. Wong, R.T. Yang, Surface Diffusion, Catal. Rev. 31 (1989) 129–214. https://doi.org/10.1080/01614948909351350.

[22] T. Handayani, Emriadi, Deswati, P. Ramadhani, R. Zein, Modelling studies of methylene blue dye removal using activated corn husk waste: Isotherm, kinetic and thermodynamic evaluation, South African J. Chem. Eng. 47 (2024) 15–27. https://doi.org/10.1016/j.sajce.2023.10.003.

[23] L. Sellaoui, H. Guedidi, S. Knani, L. Reinert, L. Duclaux, A. Ben Lamine, Application of statistical physics formalism to the modeling of adsorption isotherms of ibuprofen on activated carbon, Fluid Phase Equilib. 387 (2015) 103–110. https://doi.org/10.1016/j.fluid.2014.12.018.

[24] L.M. Sanchez, R.P. Ollier, V.A. Alvarez, Sorption behavior of polyvinyl alcohol/bentonite hydrogels for dyes removal, J. Polym. Res. 26 (2019). https://doi.org/10.1007/s10965-019-1807-4.

[25] P.K. Jaseela, J. Garvasis, A. Joseph, Selective adsorption of methylene blue (MB) dye from aqueous mixture of MB and methyl orange (MO) using mesoporous titania (TiO2) – poly vinyl alcohol (PVA) nanocomposite, J. Mol. Liq. 286 (2019) 110908. https://doi.org/10.1016/j.molliq.2019.110908.

[26] M. Khnifira, S. El Hamidi, A. Mahsoune, M. Sadiq, G. Serdaroˇglu, S. Kaya, S. Qourzal, N. Barka, M. Abdennouri, Adsorption of methylene blue cationic dye onto brookite and rutile phases of titanium dioxide: quantum chemical and molecular dynamic simulation studies, Inorg. Chem. Commun. 129 (2021), https://doi.org/10.1016/j.inoche.2021.108659.

[27] A. Kausar, S.U. Rehman, F. Khalid, A. Bonilla-Petriciolet, D.I. Mendoza-Castillo, H.N. Bhatti, S.M. Ibrahim, M. Iqbal, Cellulose, clay and sodium alginate composites for the removal of methylene blue dye: experimental and DFT studies, Int. J. Biol. Macromol. 209 (2022) 576–585, https://doi.org/10.1016/j. ijbiomac.2022.04.044.

[28] Q.H. Zhang, B.S. Hou, Y.Y. Li, Y. Lei, X. Wang, H.F. Liu, G.A. Zhang, Two amino acid derivatives as high efficient green inhibitors for the corrosion of carbon steel in CO2-saturated formation water, Corros. Sci. 189 (2021) 109596, https://doi. org/10.1016/j.corsci.2021.109596.

[29] M. Murmu, N.C. Murmu, M. Ghosh, P. Banerjee, Density functional theory, Monte Carlo simulation and non-covalent interaction study for exploring the adsorption and corrosion inhibiting property of double azomethine functionalised organic molecules, J. Adhes. Sci. Technol. 36 (2022) 2732–2760.

[30] H. Ferkous, A. Sedik, A. Delimi, R. Redjemia, K. Abdesalem, C. Boulechfar, A. Abdennouri, A. Madaci, M. Berredjem, A. Boublia, M. Sajid Ali, B.H. Jeon, K. Kumar Yadav, Y. Benguerba, A comparative study of novel synthesized sulfamide compounds: Electrochemical, morphological, XPS, and theoretical investigations on copper corrosion inhibition in 1.0 M HCl, J. Mol. Liq. 394 (2024) 123781, https://doi.org/10.1016/j.molliq.2023.123781.

[31] N. Elboughdiri, I. Lakikza, A. Boublia, S.I. Aouni, N.E.H. Hammoudi, J. Georgin, D.S.P. Franco, H. Ferkous, D. Ghernaout, Y. Benguerba, Application of statistical physical, DFT computation and molecular dynamics simulation for enhanced removal of crystal violet and basic fuchsin dyes utilizing biosorbent derived from residual watermelon seeds (Citrullus lanatus), Process Saf. Environ. Prot. (2024).

[32] N. Elboughdiri, H. Ferkous, K. Rouibah, A. Boublia, A. Delimi, K.K. Yadav, A. Erto, D. Ghernaout, A.A.M. Salih, M. Benaissa, Y. Benguerba, Comprehensive investigation of Cu2+ adsorption from wastewater using olive-waste-derived adsorbents: experimental and molecular insights, Int. J. Mol. Sci. 25 (2024), https://doi.org/10.3390/ijms25021028.

[33] O. Moumeni, M. Mehri, R. Kerkour, A. Boublia, F. Mihoub, K. Rebai, A.A. Khan, A. Erto, A.S. Darwish, T. Lemaoui, N. Chafai, Y. Benguerba, Experimental and detailed DFT/MD simulation of α-aminophosphonates as promising corrosion inhibitor for XC48 carbon steel in HCl environment, J. Taiwan Inst. Chem. Eng. 147 (2023) 104918, https://doi.org/10.1016/j.jtice.2023.104918.

CHAPTER IV

Characterization and study of the adsorption of Methylene blue by magnetic organophilic bentonite and magnetic organophilic bentonite beads

CHAPTER IV

CHARACTERIZATION AND STUDY OF THE ADSORPTION OF METHYLENE BLUE BY MAGNETIC ORGANOPHILIC BENTONITE AND MAGNETIC ORGANOPHILIC BENTONITE BEADS

IV.1. Introduction

This chapter, structured into two distinct sections, will examine the adsorption of methylene blue (MB) on both magnetic organophilic bentonite and magnetic organophilic bentonite beads within a discontinuous system.

In the first section, we will analyze the characterization results of the materials synthesized in this study to better understand their textural, morphological, and physicochemical properties. The techniques employed include Fourier transform infrared spectroscopy (FTIR), scanning electron microscopy coupled with energy-dispersive X-ray spectroscopy (SEM/EDS), and the evaluation of isoelectric points (pHpzc).

In the second section, we will examine the experimental outcomes related to the adsorption process for each adsorbent. This includes the influence of pH, the impact of adsorbent dosage, the effect of temperature, and the thermodynamic parameters of adsorption. Additionally, we will assess the effect of the initial adsorbate concentration and investigate adsorption kinetics to determine the contact time required to achieve equilibrium between the adsorbent and adsorbate. Furthermore, we will analyze the characteristic adsorption isotherms of each adsorbent-adsorbate system. This investigation will enhance our understanding of the adsorption mechanisms, quantify the maximum amount of dye removed by our materials, explore statistical physics models, and ultimately examine the regeneration of encapsulated adsorbents.

IV.2. Characterization

IV.2.1. Fourier-transform infrared spectroscopy
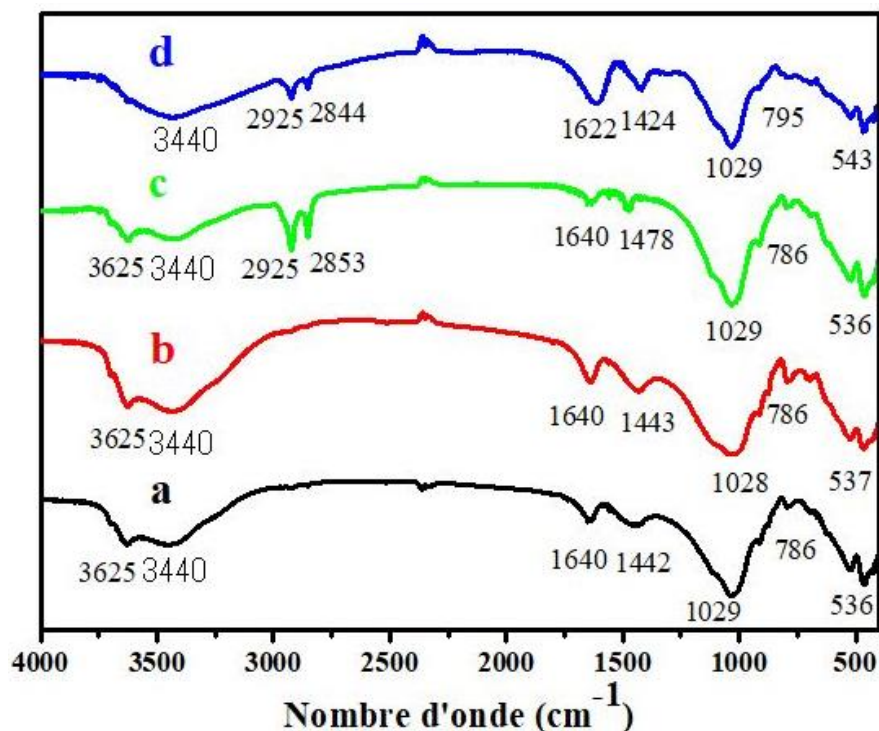
Figure IV.1: Infrared spectra (IRTF) of (a) Raw bentonite, (b) Purified bentonite, (c) Magnetic organophilic bentonite, (d) Beads of magnetic organophilic bentonite.

In this study, we analyzed the infrared spectra of contaminated bentonite, purified bentonite, magnetic organophilic bentonite, and beads of magnetic organophilic bentonite, as depicted in Figure IV.1. The spectra reveal key absorption bands linked to the vibrational modes of various functional groups. A broad band centered at 3624-3620 cm^{-1} corresponds to the valence vibrations of OH groups associated with octahedral Al cations (Al-OH-Al) [1]. Additionally, the band at 3440-3430 cm^{-1} is attributed to OH-Fe^{3+} vibrations, which broadens the overall absorption profile. An intense band at 1034-1028 cm^{-1} reflects the valence vibrations of the Si-O bond in the plane, while bands observed at 858-847, 792-788, 626-617, and 520-514 cm^{-1} are related to the deformation vibrations of Si-O-Al / Al-OH-Mg bonds, Cristobalite, Si-O-Mg bonds, and Mg-OH bonds, respectively [2]. Furthermore, the spectra of magnetic organophilic bentonite and its beads indicate the presence of surfactants, evidenced by the symmetric valence vibration bands between 2858 and 2850 cm^{-1} and the antisymmetric bands between 2928 and 2921 cm^{-1} for the CH$_2$ group. This analysis underscores the chemical

modifications that occur during the purification and organophilization processes, which are crucial for understanding the material's functional properties [3].

IV.2.2. Scanning electron microscopy /energy-dispersive X-ray spectroscopy

The SEM images of MBent-organo and MBent-organo-A beads are shown in in Figure IV.2 (a and b), respectively. in Figure IV.2 (a), it is evident that the aggregation of Fe_3O_4 nanoparticles as well as several individual Fe_3O_4 nanoparticles with nano-size were seen on the surface of organophilic bentonite. Fe_3O_4 nanoparticles indicate that MBent-organo is a magnetic adsorbent [4]. The SEM image in Figure IV.2 (b) illustrates a single MBent-organo-A beads with a nearly spherical shape, indicative of successful bead formation. The electron microscope (EDS) results represented in the tables inside Figure IV.2 (a and b), indicate that the atomic percentage of iron is 9.34 % for MBent-organo and 4.80 % for MBent-organo-A beads, This verifies the presence of additional Fe_3O_4 nanoparticles on the surface of the organophilic bentonite and indicates that the bentonite and iron nanoparticles have been smoothly incorporated into the bead composition [5].

a)

Element	Atomic %
O	56.86
Na	-
Mg	0.569
Al	7.119
Si	20.98
Cl	0.449
K	0.917
Ca	0.47
Ti	-
V	0.97
Mn	2.33
Fe	9.34

b)

Element	Atomic %
O	69.67
Na	1.07
Mg	0. 678
Al	3.38
Si	12.6
Cl	1.13
K	0.29
Ca	5.08
Ti	-
V	-
Mn	1.30
Fe	4.80
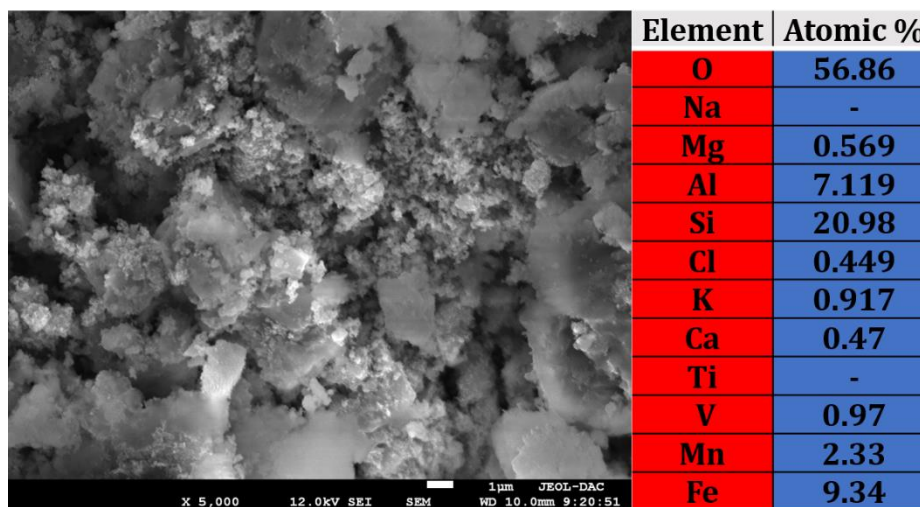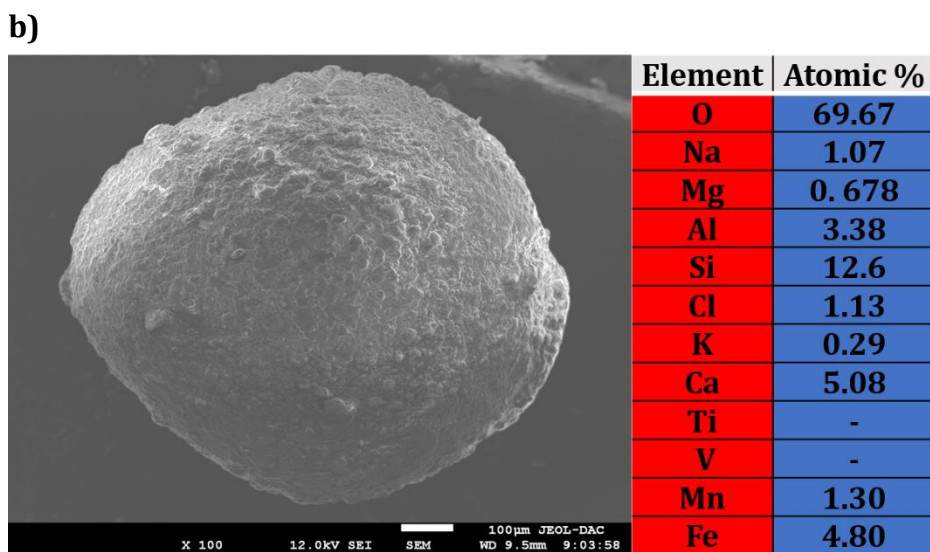
Figure IV.2. SEM images and EDS curves (a) of MBent-organo and (b) of MBent-organo-A beads.

IV.2.3. Point of zero charge

The pH at the point of zero charge (pH_{pzc}) for both MBent-organo and MBent-organo-A beads was identified, as displayed in Figure IV.3. The pH_{pzc} corresponds to the pH at which the material's surface has no net charge, which is essential for predicting how the material will interact with various adsorbates in adsorption processes [6]. In Figure IV.3 (a), the pH_{pzc} for MBent-organo is observed at 7.07. At pH levels lower than 7.07, the MBent-organo surface becomes positively charged, while it turns negatively charged when the pH exceeds this value. The curve showing the difference between the initial pH (pH_i) and final pH (pH_f) crosses the X-axis at this point, confirming the pH_{pzc}. Similarly, for MBent-organo-A beads (Figure IV.3 (b)), the pH_{pzc} is slightly higher, at 7.29. Below this pH, the MBent-organo-A beads carry a positive charge, while above 7.29, the surface becomes negatively charged. The curve again intersects the X-axis, marking the zero-charge point [7].

a)

b)
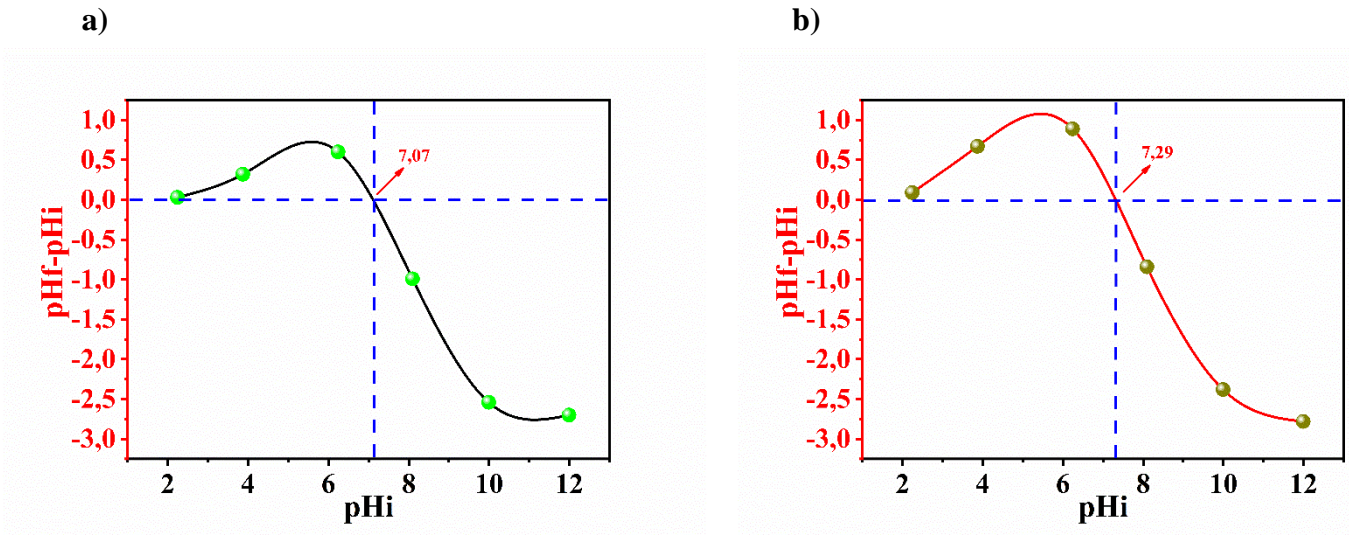
Figure IV.3. Zero charge pH (pH$_{pzc}$) point (a) of MBent-organo and (b) of MBent-organo-A beads.

In conclusion, MBent-organo and MBent-organo-A beads exhibit close but distinct pHpzc values, with MBent-organo-A beads having a slightly higher pHpzc (7.29) than MBent-organo (7.07). This suggests that MBent-organo-A beads reach a neutral surface charge at a higher pH, which may influence their adsorption capacity under different pH conditions.

IV.3. Adsorption parameters experimental results

IV.3.1. pH parameter impact

a)

b)
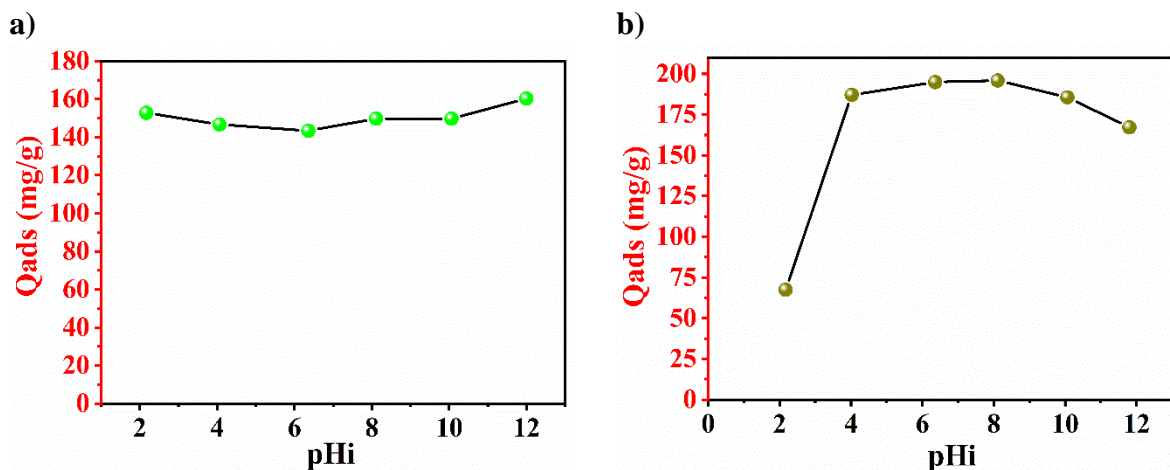
Figure IV.4. Effect of pH (a) of MBent-organo and (b) of MBent-organo-A beads (Initial MB dye concentration = 200 mg/L, V = 20 ml, W= 20 mg, T = 25 °C and stirring speed = 250rpm).

The effect of pH on the adsorption capacity (Qads) for MBent-organo and MBent-organo-A beads is illustrated in Figure IV.4. The adsorption behavior of both materials is significantly influenced by the pH, affecting their capacity to retain the adsorbate. For MBent-organo (Figure IV.4 (a)), the adsorption capacity remains relatively stable across the pH range, with values consistently around 160 mg/g. There is no dramatic change as the pH increases, indicating that the adsorption capacity of MBent-organo is not highly pH-dependent, maintaining efficiency over a wide pH spectrum.

In contrast, the MBent-organo-A beads (Figure IV.4 (b)) show a more distinct variation in adsorption capacity with pH. The adsorption capacity increases sharply up to a peak value of approximately 200 mg/g around pH **7**, after which it slightly decreases. This behavior suggests that MBent-organo-A beads exhibit higher adsorption efficiency around neutral pH, with a notable dependency on pH at lower values, followed by stabilization at higher pH levels [7,8].

IV.3.2. Dosage absorbent parameter impact
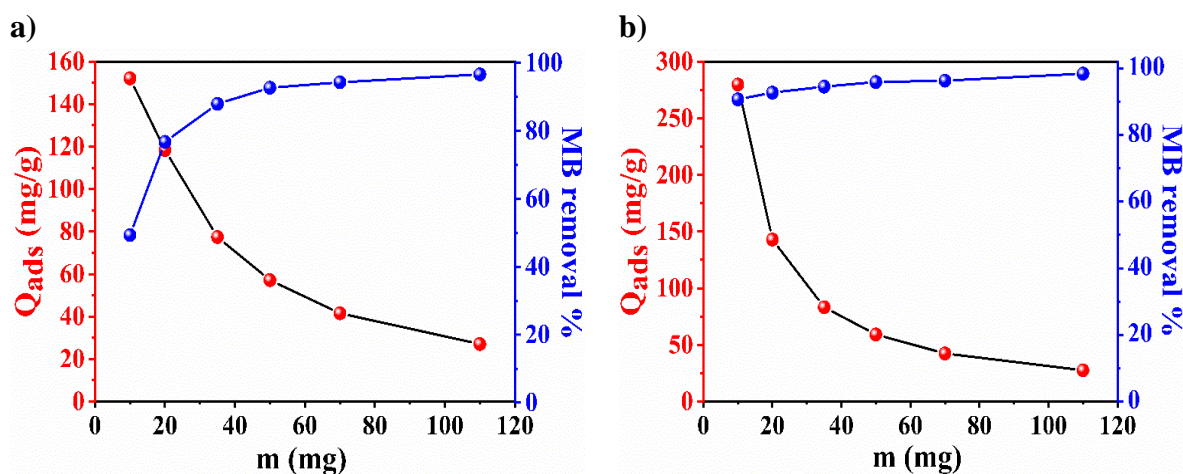
Figure IV.5. Effect of dosage adsorbent (a) of MBent-organo and (b) of MBent-organo-A beads (Initial MB dye concentration = 200 mg/L, V = 20 ml, T = 25 °C and stirring speed = 250rpm).

Figure IV.5 illustrates the relationship between the quantity of adsorbent and both the adsorption capacity (Q_{ads}) and the percentage removal of methylene blue (R %). The fluctuation of these parameters in relation to the adsorbent mass (m) offers valuable insights into the efficacy of MBent-organo and MBent-organo-A beads materials. In the case of

MBent-organo (Figure IV.5 (a)), there is a marked decline in adsorption capacity with an increase in adsorbent dosage, decreasing from 152 mg/g to approximately 27 mg/g at a dosage of 110 mg. The observed decline can be explained by the saturation of active sites, at reduced dosages, these sites are abundantly accessible, whereas an increase in adsorbent mass leads to a decrease in the quantity of dye available for each active site. Simultaneously, the percentage of methylene blue removal increases significantly, achieving around 90 % with merely 40 mg of adsorbent before leveling off [9].

In the instance of MBent-organo-A beads (Figure IV.5 (b)), a comparable pattern is noted: the adsorption capacity experiences a significant reduction, decreasing from 280 mg/g to approximately 28 mg/g as the adsorbent mass increases. Similar to MBent-organo, this reduction arises from the saturation of active sites when higher dosages are applied. Nonetheless, the percentage of methylene blue removal nearly reaches 95 % at just 40 mg, demonstrating remarkable removal efficiency, even though there is a decline in adsorption capacity per gram [8].

In summary, although the adsorption capacity per unit mass decreases with an increase in the quantity of adsorbent for both materials. MBent-organo-A beads demonstrate a superior initial adsorption capacity relative to MBent-organo, presumably attributable to a higher density of active sites or improved interactions with the dye.

IV.3.3. Temperature parameter impact and thermodynamic adsorption parameters
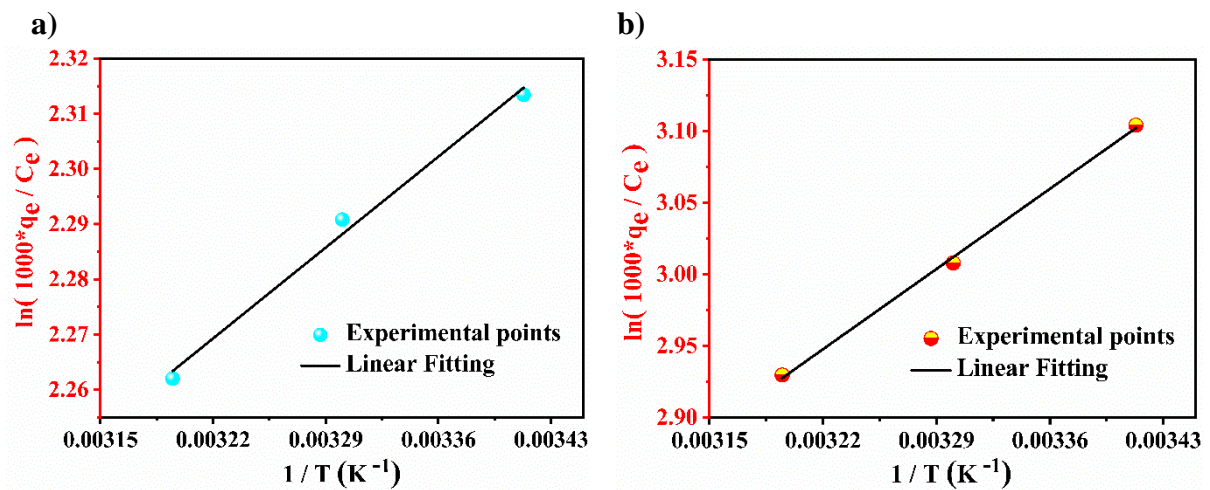
Figure IV.6. Regression of the thermodynamic parameters on the MB adsorption onto (a) of MBent-organo and (b) of MBent-organo-A beads.

Figure IV.6 clearly illustrates the thermodynamic behavior of the adsorption process, depicting the regression of the thermodynamic parameters for the adsorption of Methylene Blue (MB) onto both MBent-organo and MBent-organo-A beads. The analysis confirms that the adsorption is exothermic for both materials, as evidenced by the negative enthalpy change ($\Delta H°$) values in Tables IV.1 and IV.2. As expected for an exothermic process, adsorption capacity decreases with increasing temperature [10].

Table IV.1. Thermodynamic properties of MB adsorption on MBent-organo.

T (K)	$\Delta H°$ (kJ/mol)	$\Delta S°$ (J/mol^{-1}K)	$\Delta G°$ (kJ/mol)
293			-5.64
303	-1.96	12.56	-5.76
313			-5.89

The spontaneity of the adsorption is confirmed by the negative Gibbs free energy ($\Delta G°$) values at all tested temperatures. Additionally, $\Delta G°$ values become slightly more negative as temperature increases, indicating that the spontaneity of adsorption remains stable [11].

The positive entropy change ($\Delta S°$) for both adsorbents suggests an increase in disorder at the solid-liquid interface during adsorption [12]. The higher entropy change for MBent-organo suggests stronger interactions between MB molecules and the adsorbent surface, leading to a more thermodynamically favorable adsorption process compared to MBent-organo-A beads.

Table IV.2. Thermodynamic properties of MB adsorption on MBent-organo-A beads.

T (K)	$\Delta H°$ (kJ/mol)	$\Delta S°$ (J/mol^{-1}K)	$\Delta G°$ (kJ/mol)
293			-7.56
303	-6.65	3.08	-7.59
313			-7.62

In summary, the thermodynamic analysis confirms that the adsorption of MB onto both MBent-organo and MBent-organo-A beads is exothermic and spontaneous [13], with stronger adsorption interactions observed in the MBent-organo system. The higher entropy change and enthalpic favorability of MBent-organo suggest a more efficient adsorption process compared to MBent-organo-A beads [11].

IV.3.4. MB initial concentration and contact time parameters influence

a)   b)
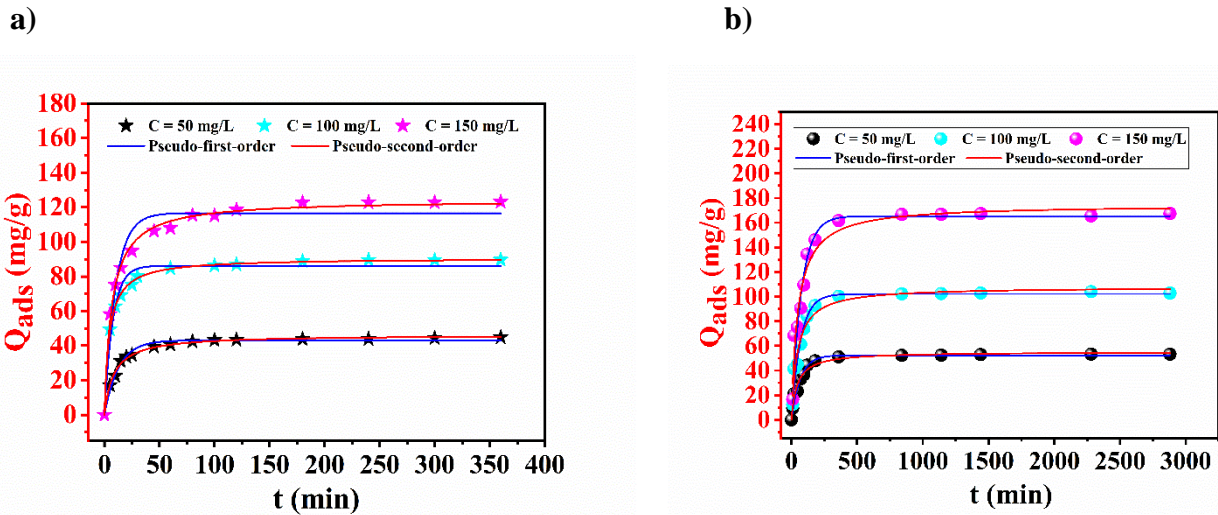
Figure IV.7. Initial dye concentration and non-linear fitting of pseudo-first-order and pseudo-second-order model (a) of MBent-organo and (b) of MBent-organo-A beads (V = 20 ml, W = 20 mg, T = 25 °C and stirring speed = 250rpm).

Based on the data presented in Figure IV.7 (a) and Figure IV.7 (b), the analysis reveals the influence of initial dye concentrations MBent-organo and MBent-organo-A beads. The experiments were conducted using initial concentrations of 50, 100, and 150 mg/L, with the adsorption processes modeled using both pseudo-first-order and pseudo-second-order kinetics [14]. For MBent-organo (Figure IV.7 (a)), it is evident that higher initial dye concentrations led to an increase in adsorption capacity. At 50 mg/L, the adsorption capacity Qads stabilized around 44 mg/g, whereas at 150 mg/L, the capacity reached approximately 123 mg/g. The adsorption process occurred more rapidly at lower concentrations, achieving equilibrium within approximately 50 minutes for 50 mg/L. However, at higher concentrations such as 150 mg/L, equilibrium was reached more gradually, after about 100 minutes. This could be due to the slower saturation of active sites at elevated concentrations, which impedes the adsorption process over time [15].

Similarly, for MBent-organo-A beads (Figure IV.7 (b)), an increase in the initial dye concentration led to a significant rise in adsorption capacity. At 50 mg/L, the adsorption capacity reached about 53 mg/g, while at 150 mg/L, the capacity increased to roughly 167 mg/g. The time required to reach equilibrium was substantially longer for MBent-organo-A beads compared to MBent-organo. At 50 mg/L, equilibrium was established after nearly 250 minutes, while for 150 mg/L, it took about 500 minutes (approximately 8 hours). This indicates that higher concentrations not only increase adsorption capacity but also significantly prolong the equilibrium time, likely due to slower diffusion of dye molecules into the adsorbent's matrix [16].

In both cases, the pseudo-second-order model provided a better fit to the experimental data, suggesting that chemisorption is the dominant mechanism controlling the adsorption kinetics. As initial dye concentrations increase, the number of available adsorption sites becomes saturated more quickly, leading to delayed equilibrium times and higher adsorption capacities [17].

IV.3.5. Kinetic modeling

Kinetic parameters were derived through non-linear regression analysis and are presented in Table IV.3 and Table IV.4. The experimental data for MBent-organo (Table IV.3) demonstrates a strong correlation with the pseudo-second-order model, as evidenced by the high R² values, which range from 0.995 to 0.999. The adsorption capacity Q_{ads} for MB increases from 44.81 mg/g to 123.22 mg/g as the initial concentration increases from 50 mg/L to 150 mg/L [18].

For the MBent-organo-A beads composite (Table IV.4), the pseudo-second-order model demonstrates a strong fit, with R^2 values ranging from 0.962 to 0.982. The adsorption capacity Q_{ads} for MB significantly increases from 53.24 mg/g at an initial concentration of 50 mg/L to 167.47 mg/g at 150 mg/L. The results indicate a higher adsorption capacity at increased initial dye concentrations for both MBent-organo and the MBent-organo-A beads composite, suggesting a greater availability of active sites during the initial stages of adsorption [13]. The high determination coefficient (R^2) values, ranging from 0.995 to 0.999 in Table IV.3, indicate that the pseudo-second-order kinetic model effectively describes the adsorption of MB dye on MBent-organo within the examined concentration range. The pseudo-first-order model demonstrated R^2 values between 0.958 and 0.985, suggesting a less

accurate fit to the experimental data. The rate constants k_1 and k_2 are significantly affected by the initial concentrations of MB dye. The k_1 values decline from $0.13.10^{-2}$ L/min to $0.08.10^{-2}$ L/min for the pseudo-first-order model. In a similar manner, the values of k_2 decrease from $0.003.10^{-3}$ g/mg min at 50 mg/L to $0.001.10^{-3}$ g/mg min at 150 mg/L. The observed decrease in rate constants with increasing initial concentration C_0 indicates slower adsorption kinetics at elevated concentrations, likely resulting from the saturation of available active sites [19].

Table IV.3. Kinetic parameters for MB adsorption onto MBent-organo at 25 ℃.

C_0 (mg/L)	q_{exp} (mg/g)	Pseudo-first-order			Pseudo-second-order		
		$K_1 \times 10^2$ (L/min)	q_{cal} (mg/g)	R^2	$K_2 \times 10^3$ (g/mg min)	q_{cal} (mg/g)	R^2
50	44.81	0.08	43.06	0.985	0.003	46.26	0.995
100	89.64	0.13	86.18	0.972	0.003	90.59	0.999
150	123.22	0.09	116.56	0.958	0.001	124.34	0.995

The high determination coefficient (R^2) values, ranging from 0.962 to 0.982 as presented in Table IV.4, indicate that the pseudo-second-order kinetic model effectively describes the adsorption of MB dye on the MBent-organo-A beads composite within the studied concentration range. The pseudo-first-order model demonstrated R^2 values between 0.962 and 0.98, suggesting a marginally less accurate fit to the experimental data [20]. The rate constants k_1 and k_2 are significantly affected by the initial concentrations of MB dye. The k_1 values decline from $0.015. 10^{-3}$ L/min at 50 mg/L to $0.013. 10^{-3}$ L/min at 150 mg/L for the pseudo-first-order model. In the case of the pseudo-second-order model, the values of k_2 decrease from $4.27.10^{-4}$ g/mg min at 50 mg/L to $1.17.10^{-4}$ g/mg min at 150 mg/L. The observed decrease in rate constants with increasing initial concentration C_0 suggests a slower adsorption process at elevated concentrations, likely attributable to the diminished availability of active sites as saturation occurs.

Table IV.4. Kinetic parameters for MB adsorption onto MBent-organo-A beads composite at 25 ℃.

C_0	q_{exp}	Pseudo-first-order			Pseudo-second-order		
(mg/L)	(mg/g)	$K_l \times 10^3$	q_{cal}	R^2	$K_2 \times 10^4$	q_{cal} (mg/g)	R^2
		(L/min)	(mg/g)		(g/mg min)		
50	53.24	0.015	52.35	0.98	4.27	55.17	0.982
100	102.88	0.014	102.18	0.973	2.06	107.86	0.967
150	167.47	0.013	165.34	0.962	1.17	174.62	0.962

Overall, the pseudo-second-order model provides a better fit to the experimental data for both MBent-organo and MBent-organo-A beads composite, with the latter showing higher adsorption capacities at the same initial concentrations of MB. This suggests that the composite offers superior adsorption efficacy compared to MBent-organo alone [21].

The adsorption of Methylene Blue (MB) onto MBent-organo and MBent-organo-A beads was investigated using the intra-particle diffusion model, as shown in Figure IV.8. Figure IV.8 (a) depicts the adsorption capacity q_t as a function of the square root of time $t^{0.5}$ for MBent-organo at various initial MB concentrations, ranging from 50 to 150 mg/L. The adsorption capacity increases as the initial concentration increases, with a clear multi-stage behavior, indicating that the adsorption process occurs in different phases. The plateau observed towards the end suggests that adsorption equilibrium has been reached [22].
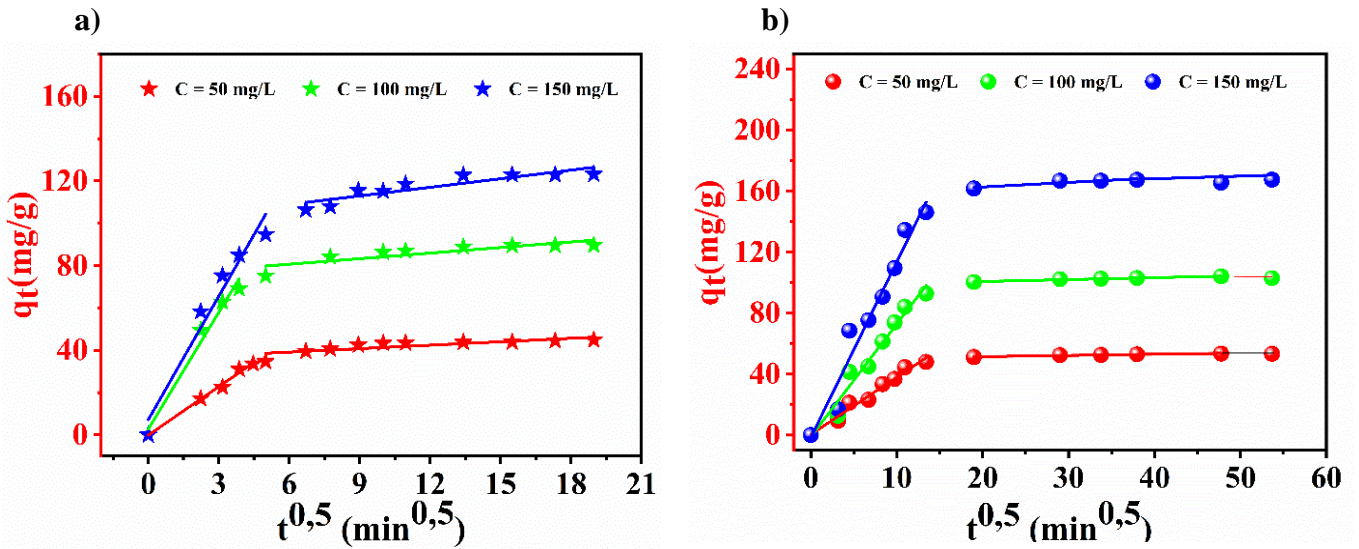
Figure IV.8. plots of the intra-particle diffusion model on the MB adsorption onto (a) of MBent-organo and (b) of MBent-organo-A beads (V = 20 ml, W = 20 mg, T = 25 °C and stirring speed = 250rpm).

Similarly, Figure IV.8 (b) presents the intra-particle diffusion of MB onto MBent-organo-A beads at the same concentration range, 50 to 150 mg/L. Just like in MBent-organo, the adsorption process follows a multi-stage mechanism. However, MBent-organo-A beads show a significantly higher adsorption capacity compared to MBent-organo, suggesting enhanced adsorption efficiency. This demonstrates that MBent-organo-A beads have a higher affinity for MB molecules, leading to better adsorption at equilibrium. The plots in Figure IV.8 (both a and b) reveal a non-linear trend throughout the adsorption process, which can be broken down into two distinct phases. This can be attributed to changes in mass transfer rates during adsorption. The first phase shows rapid adsorption, which is likely due to the abundance of available active sites, followed by a slower second phase, influenced by the diffusion of the adsorbate within the pores of the adsorbent.

Table IV.5 presents the intra-particle diffusion parameters for MB adsorption onto MBent-organo. The data indicates that the values of k_{id1} are consistently higher than those of k_{id2} (Step 2), and both values increase as the initial concentration of MB increases. This initial high adsorption rate is due to the availability of active sites in the early stages of the process. For example, at 150 mg/L, k_{id1} is 19.41, while k_{id2} is much lower at 1.352, emphasizing the rapid early adsorption.

Table IV.5. Intraparticle diffusion parameters for MB adsorption onto MBent-organo.

C_0 (mg/L)	Intraparticle diffusion model					
Parameters	**Step 1**			**Step 2**		
	k_{id1}	C_{i1}	R^2	k_{id2}	C_{i2}	R^2
50	7.63	0.118	0.991	0.543	35.88	0.629
100	18.36	2.742	0.966	0.877	75.43	0.696
150	19.41	7.22	0.94	1.352	100.8	0.776

Similarly, Table IV.6 shows the parameters for MB adsorption onto MBent-organo-A beads. The same trend is observed, with k_{id1} values being higher than k_{id2}, and both increasing with higher initial concentrations. For instance, at 150 mg/L, k_{id1} is 11.50, and k_{id2} is 0.302. This highlights the enhanced structural properties of MBent-organo-A beads, which result in greater adsorption efficiency, particularly at higher concentrations.

Table IV.6. Intraparticle diffusion parameters for MB adsorption onto MBent-organo-A beads.

C_0 (mg/L)	Intraparticle diffusion model					
Parameters	**Step 1**					**Step 2**
	k_{id1}	C_{i1}	R^2	k_{id2}	C_{i2}	R^2
50	3.75	0.379	0.971	0.077	49.84	0.925
100	7.38	1.016	0.962	0.125	98.24	0.958
150	11.50	1.52	0.949	0.302	156.62	0.798

In both cases, the first stage of rapid adsorption is linked to external surface adsorption, while the second stage represents intraparticle diffusion. The results confirm that MBent-organo-A beads have superior MB removal efficiency, attributed to improved diffusion properties and higher adsorption capacity at equilibrium [23].

IV.3.6. Isotherm modeling

a)   b)

c)
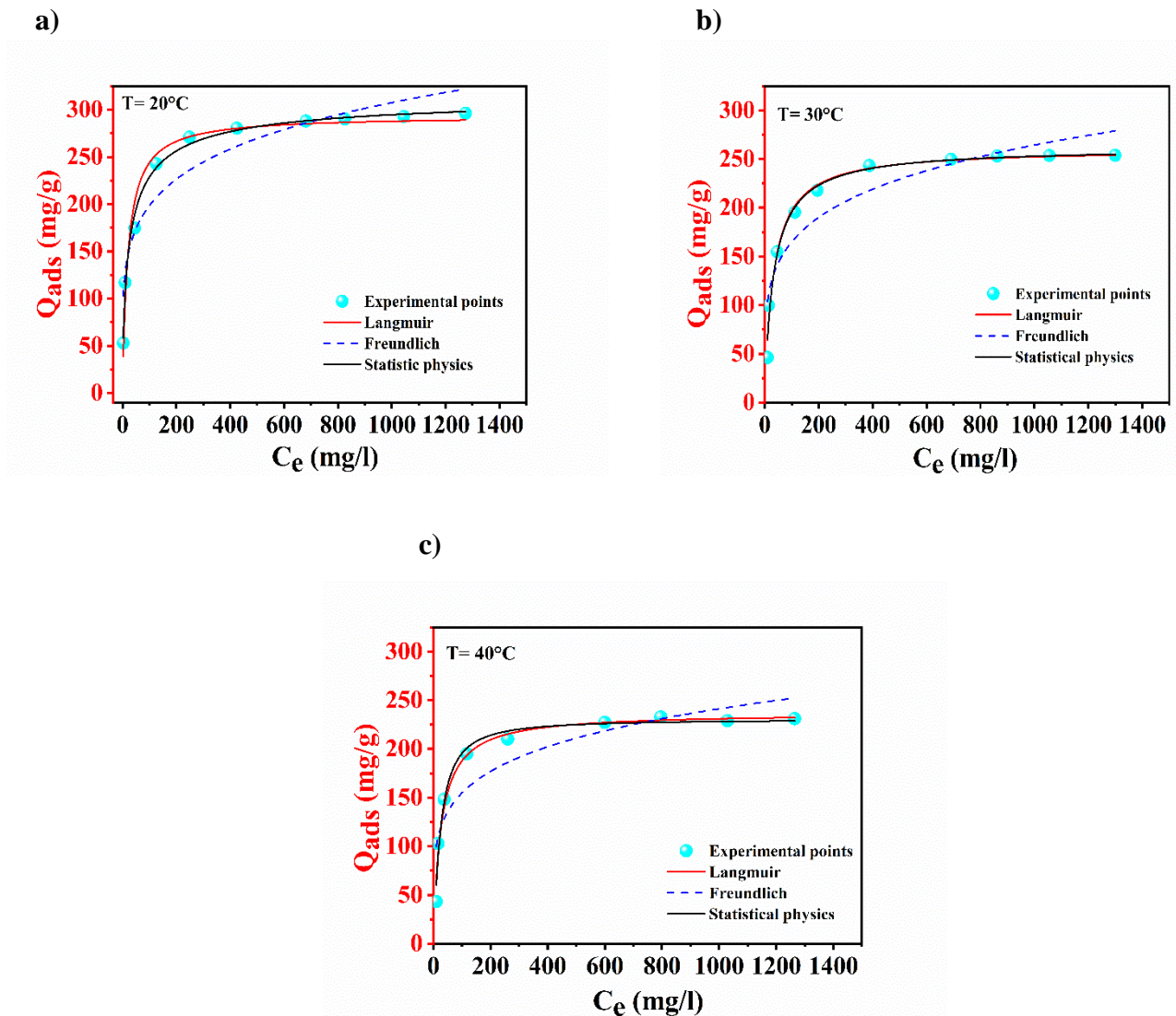
Figure IV.9. Adsorption isotherms for MB adsorption onto MBent-organo at 20, 30, 40 ℃
(V = 20 ml, W = 20 mg and stirring speed = 250rpm).

The adsorption isotherms shown in Figure IV.9 present the behavior of MB adsorption onto the MBent-organo composite at temperatures of 20 °C, 30 °C, and 40 °C. The experimental points are plotted alongside the Langmuir and Freundlich models to provide a comparative analysis of how well each model fits the data at different temperatures.

The Langmuir isotherm, which assumes a single layer of adsorption on a uniform surface, fits well with the data across all temperatures, as seen in the high R^2 values of 0.974, 0.984, and 0.978 for 20, 30, and 40 °C, respectively (Table IV.7). The maximum adsorption capacity

q_m decreases with increasing temperature, starting from 293.64 mg/g at 20 °C and dropping to 237.05 mg/g at 40 °C. This decline suggests that the adsorption capacity decreases at higher temperatures, which is often characteristic of exothermic adsorption processes. The Langmuir constant K_L shows some variability, with values of 0.049 L/mg at 20 °C, 0.031 L/mg at 30 °C, and 0.038 L/mg at 40 °C. Despite this variability, the R_L values confirm that the adsorption is favorable at all temperatures. The Freundlich model, which describes adsorption on heterogeneous surfaces with the possibility of multilayer adsorption, shows a lower degree of fit compared to the Langmuir model, with R^2 values of 0.904, 0.863, and 0.832 for 20, 30, and 40 °C, respectively. The Freundlich constant K_F decreases with increasing temperature, from 82.68 mg/g at 20 °C to 63.86 mg/g at 40 °C, indicating that the adsorption capacity declines at higher temperatures. The 1/n values remain below 1 across all temperatures, suggesting favorable adsorption conditions, though the Freundlich model does not describe the process as accurately as the Langmuir model.

Table IV.7. Isotherms parameters for MB adsorption onto MBent-organo at 20, 30, 40 °C.

Models	Parameters	20 °C	30 °C	40 °C
Langmuir	q_m (mg/g)	293.64	260.45	237.05
	K_L (L/mg)	0.049	0.031	0.038
	R^2	0.974	0.984	0.978
	R_L (Min-Max)	0.267-0.013	0.362-0.021	0.329-0.017
Freundlich	K_f ((mg/g) (L/ g)$^{1/n}$)	82.68	64.29	63.86
	1/n	0.19	0.205	0.192
	R^2	0.904	0.863	0.832
Statistic physics	n	0.702	0.965	1.212
	D_m (mg/g)	451.905	271.877	190.424
	Nsat (mg/g)	317.237	262.361	230.791
	$C_{1/2}$ (mg/L)	25.9256	33.0019	24.3286
	R^2	0.991	0.984	0.982

In summary, the Langmuir isotherm provides a better fit for the data, indicating monolayer adsorption on a relatively uniform surface. The decrease in adsorption capacity with

increasing temperature suggests an exothermic adsorption process, and although the Freundlich model captures some aspects of the adsorption behavior, it is less effective in describing the overall process [24].

a)

b)

c)
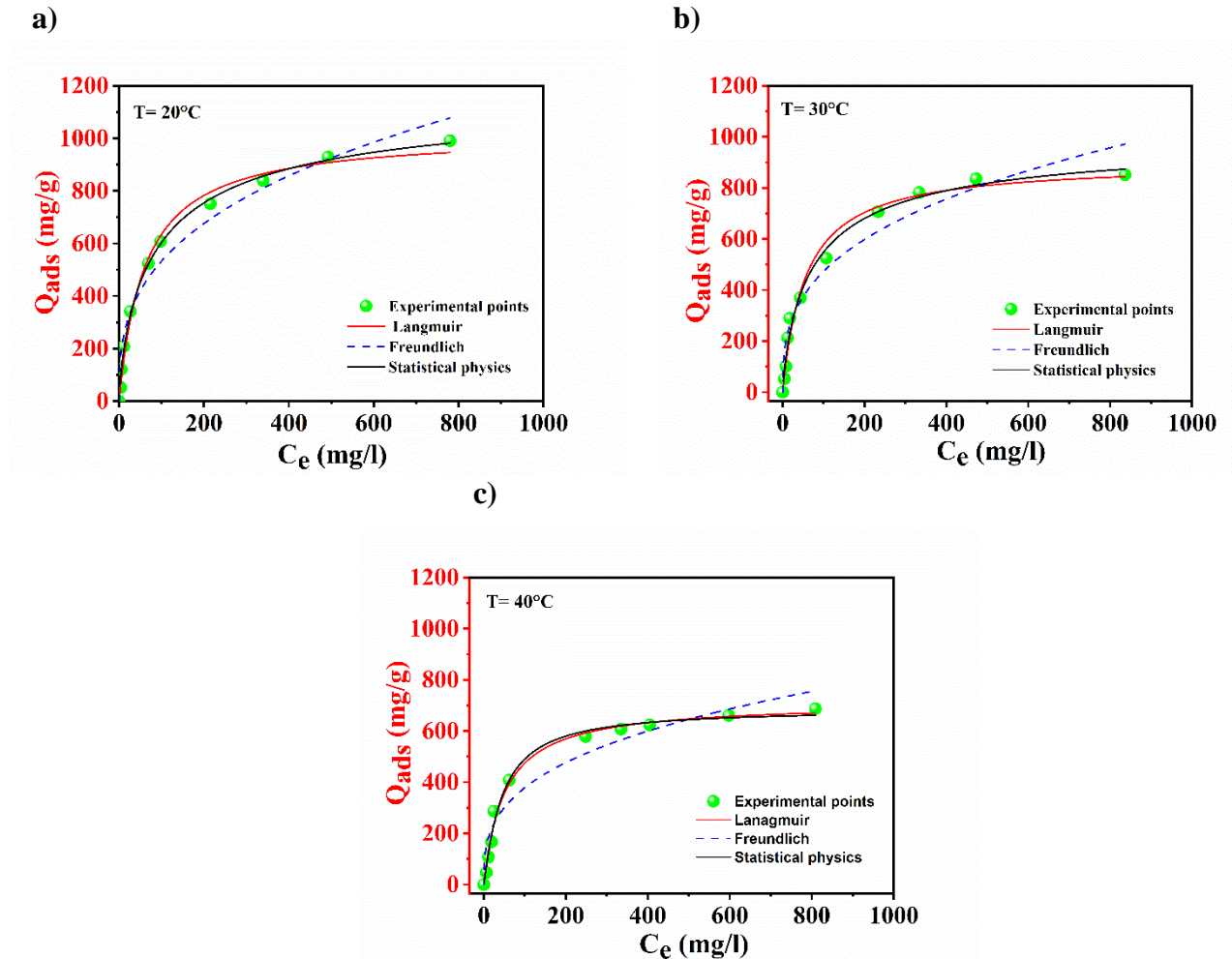
Figure IV.10. Adsorption isotherms for MB adsorption onto MBent-organo-A beads composite at 15, 25, 30, and 40 ℃ (V = 20 ml, W = 20 mg and stirring speed = 250rpm).

The adsorption isotherms for MB on MBent-organo-A beads composite at temperatures of 20 °C, 30 °C, and 40 °C (Figure IV.10) provide insights into the behavior of the adsorbent at various temperatures. The Langmuir and Freundlich models were employed to analyze the experimental data, which describe different aspects of adsorption. The Langmuir isotherm model, which assumes monolayer adsorption on a homogenous surface, fits well across all temperatures, as evidenced by the high R^2 values of 0.991 at 20 °C and 40 °C (Table IV.8), and 0.986 at 30 °C. This model reflects a gradual decrease in the maximum adsorption

capacity q_m from 1019.36 mg/g at 20 °C to 711.86 mg/g at 40 °C, indicating that higher temperatures reduce the adsorption capacity. The Langmuir constant K_L which indicates the affinity between the adsorbate and the adsorbent, shows a slight increase with temperature, varying from 0.0165 L/mg at 20 °C to 0.0199 L/mg at 40 °C. The R_L separation factor remains within a favorable range, suggesting that the adsorption process is favorable under all tested conditions. On the other hand, the Freundlich model, which accounts for multilayer adsorption on heterogeneous surfaces, does not fit as well, as reflected by the lower R² values compared to the Langmuir model. The Freundlich constant K_f decreases from 109.96 mg/g at 20 °C to 82.11 mg/g at 40 °C, indicating a reduction in adsorption capacity with increasing temperature. The 1/n values, which remain below 1 across the temperatures (ranging from 0.34 to 0.33), suggest that the adsorption process is favorable, though not as strongly represented as in the Langmuir model [6].

Table IV.8. Isotherms parameters for MB adsorption onto MBent-organo-A beads at 20, 30 and 40 °C.

Models	Parameters	20 °C	30 °C	40 °C
Langmuir	q_m (mg/g)	1019.36	900.38	711.86
	K_L (L/mg)	0.0165	0.0179	0.0199
	R^2	0.991	0.986	0.991
	R_L (Min-Max)	0.52-0.033	0.496-0.032	0.484-0.032
Freundlich	K_f ((mg/g) (L/ g)$^{1/n}$)	109.96	99.31	82.11
	1/n	0.34	0.34	0.33
	R^2	0.968	0.951	0.942
Statistic physics	n	0.758	0.800	1.119
	D_m (mg/g)	1555.25	1258.57	613.44
	Nsat (mg/g)	1178.879	1006.856	686.439
	$C_{1/2}$ (mg/L)	93.42	79.82	44.17
	R^2	0.997	0.990	0.992

Overall, the Langmuir model better describes the adsorption behavior of MB on MBent-organo-A beads at the temperatures studied, particularly at lower temperatures, where the adsorption capacity is highest.

IV.3.7. Statistical physics model

The analysis of adsorption isotherms for methylene blue (MB) on MBent-organo and MBent-organo-A beads using a statistical physics model reveals distinct trends in adsorption behavior across varying temperatures.

For MBent-organo, the parameters indicate a notable decrease in maximum adsorption density D_m as the temperature rises: from 451.91 mg/g at 20 °C to 271.88 mg/g at 30 °C, and further to 190.42 mg/g at 40 °C. This trend suggests that higher temperatures lead to reduced capacity for MB adsorption. Concurrently, the saturation number N_{sat} also decreases from 317.24 mg/g at 20 °C to 230.79 mg/g at 40 °C, reinforcing the notion of diminished adsorption potential with increasing temperature. The $C^{\frac{1}{2}}$ value, reflecting the concentration needed to occupy half of the adsorption sites, fluctuates, starting at 25.93 mg/L at 20°C, rising to 33.00 mg/L at 30 °C, and then dropping to 24.33 mg/L at 40 °C. This pattern indicates varying requirements for concentration at different temperatures. The model fit remains strong, with R^2 values ranging from 0.982 to 0.991, showcasing good correlation with experimental data (Table IV.7).

In contrast, the adsorption characteristics for MBent-organo-A beads present a different scenario. The maximum adsorption density D_m is significantly higher, starting at 1555.25 mg/g at 20 °C, decreasing to 1258.57 mg/g at 30 °C, and further dropping to 613.44 mg/g at 40 °C. This indicates that MBent-organo-A beads have a much greater initial capacity for MB adsorption compared to MBent-organo. The saturation number N_{sat} also reflects this trend, starting at 1178.88 mg/g at 20 °C and decreasing to 686.44 mg/g at 40 °C, illustrating a substantial decline in adsorption capacity at elevated temperatures. The $C^{\frac{1}{2}}$ values indicate that significantly higher concentrations are needed to occupy half of the adsorption sites, beginning at 93.42 mg/L at 20 °C, dropping to 79.82 mg/L at 30 °C, and further to 44.17 mg/L at 40°C. These shifts in $C^{\frac{1}{2}}$ values suggest enhanced accessibility at lower concentrations at higher temperatures. The robustness of the model is confirmed by high R^2 values ranging from 0.990 to 0.997, indicating a very strong alignment with experimental findings (Table IV.8) [4].

In summary, the comparative analysis of MB adsorption on MBent-organo and MBent-organo-A beads illustrates the complex interplay between temperature and adsorption capacity, highlighting the superior initial adsorption potential of MBent-organo-A beads

while also emphasizing the decline in capacity with rising temperatures. This information is vital for optimizing adsorption processes in practical applications.

IV.3.8. Regeneration study

The regeneration and reuse of adsorbents are essential aspects of adsorption processes, offering both economic benefits and reducing environmental impact in various applications. As adsorbents gradually become saturated with adsorbates, their capacity to adsorb diminishes. Regeneration, which involves removing the adsorbed substances from the adsorbent's surface, helps restore its efficiency and prolong its usability. Several techniques are employed to achieve this.

Figure IV.11 presents promising findings, showing the successful regeneration of MBent-organo-A beads composite after adsorbing Methylene Blue (MB) dye. Across five regeneration cycles, the adsorption efficiency drops only slightly, from about 98 % in the first cycle to roughly 90 % in the fifth. This minimal decrease underscores the material's strong potential for reuse and cost-effectiveness. The adsorption process was carried out under consistent conditions: an initial MB concentration of 100 mg/L, temperature of 25 °C, 50 mL solution volume, 50 mg of adsorbent, and a stirring speed of 250 rpm. These results emphasize the durability of MBent-organo-A beads for multiple cycles of MB dye removal [25].
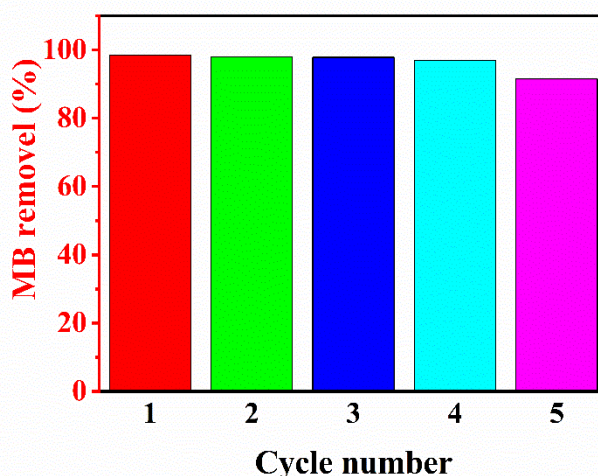

Figure IV.11. Regeneration of MBent-organo-A beads composite after adsorption of MB (initial MB dye concentration = 100 mg/L, T = 25 ℃, V = 50 mL, W = 50 mg and stirring speed = 250 rpm).

IV.4. Comparative analysis of our adsorbents versus adsorbents employed in previous studies

The efficiency of our adsorbents, MBent, MBent-A, MBent-organo, and MBent-organo-A, obtained in this work for the adsorption of methylene blue, was compared to that of other adsorbents reported in the literature (Table IV.9). The initial pollutant concentration C_0, adsorbent dosage, point of zero charge (pHpzc), pH, and maximum adsorption capacity were used as comparison parameters. These parameters, in relation to other adsorbents, demonstrate that they are effective adsorbents and can be considered promising candidates for wastewater treatment.

Table IV.9. Comparison of maximum monolayer adsorption capacity on various adsorbents.

Adsorbents	C_0 (mg/L)	Dose (g/L)	pH_{pzc}	pH	Q_{max} (mg/g)	References
Magnetic organo-bentonite	-	1	-	7	98.15	[26]
Magnetic nanoparticles CS-Glu-MCM	1400	1	-	7	185.10	[27]
Alginate	-	1	6.4	6.6	483.60	[28]
Coffee-alginate residue composites	5000	2	7.6	11	667.80	[29]
Activated bentonite composite organophilic-alginate	2000	0.4	4.2	7	769	[30]
Magnetic modification of coffee husk hydrochar	-	1.2	7.3	10	77.91	[31]
Magnetic alginate beads	300	1	-	11	106.38	[32]
Magnetic bentonite	**500**	**1**	**8.41**	**6.4**	**190.06**	**This study**
Magnetic bentonite/alginate beads	**1500**	**1**	**7.7**	**6.4**	**774.32**	**This study**
Magnetic-organo bentonite	**500**	**1**	**7.07**	**6.4**	**293.64**	**This study**
Magnetic bentonite-organo /alginate beads	**1500**	**1**	**7.29**	**6.4**	**1019.36**	**This study**

IV.5. Conclusion

This chapter investigates the adsorption of methylene blue (MB) onto magnetic organophilic bentonite (MBent-organo) and magnetic organophilic bentonite beads (MBent organo-A) in a batch system. The first section focuses on material characterization using techniques such as FTIR spectroscopy, SEM/EDS, and determining isoelectric points (pHpzc) to assess their textural and physicochemical properties.

In the second section, the study of adsorption parameters (pH, dosage, temperature) confirms that adsorption on both MBent-organo and MBent-organo-A is exothermic and thermodynamically favorable at lower temperatures. Both materials exhibit adsorption kinetics that align with the pseudo-second-order model, suggesting a rapid adsorption process. The Langmuir isotherm analysis confirms the formation of a uniform monolayer on the adsorbent surface. Higher initial MB concentrations enhance adsorption capacity, though equilibrium is gradually achieved, especially with MBent-organo-A. Nonetheless, MBent-organo-A demonstrates superior adsorption performance compared to MBent-organo. Moreover, the beads are durable, retaining a good adsorption capacity even after five regeneration cycles.

References

[1]   M. Hayati-Ashtiani, Use of FTIR spectroscopy in the characterization of natural and treated nanostructured bentonites (montmorillonites), Part. Sci. Technol. 30 (2012) 553–564. https://doi.org/10.1080/02726351.2011.615895.

[2]   M. Hayati-Ashtiani, Characterization of nano-porous bentonite (Montmorillonite) particles using FTIR and BET-BJH analyses, Part. Part. Syst. Charact. 28 (2011) 71–76. https://doi.org/10.1002/ppsc.201100030.

[3]   H. Zhang, X. Liang, C. Yang, C. Niu, J. Wang, X. Su, Nano γ-Fe2O3/bentonite magnetic composites: Synthesis, characterization and application as adsorbents, J. Alloys Compd. 688 (2016) 1019–1027. https://doi.org/10.1016/j.jallcom.2016.07.036.

[4]   Z. Lou, Z. Zhou, W. Zhang, X. Zhang, X. Hu, P. Liu, H. Zhang, Magnetized bentonite by Fe3O4 nanoparticles treated as adsorbent for methylene blue removal from aqueous solution: Synthesis, characterization, mechanism, kinetics and regeneration, J. Taiwan Inst. Chem. Eng. 49 (2015) 199–205. https://doi.org/10.1016/j.jtice.2014.11.007.

[5]   K. Vaezi, G. Asadpour, S.H. Sharifi, Bio nanocomposites based on cationic starch reinforced with montmorillonite and cellulose nanocrystals: Fundamental properties and biodegradability study, Int. J. Biol. Macromol. 146 (2020) 374–386. https://doi.org/10.1016/j.ijbiomac.2020.01.007.

[6]   A. Oussalah, A. Boukerroui, A. Aichour, B. Djellouli, Cationic and anionic dyes removal by low-cost hybrid alginate/natural bentonite composite beads: Adsorption and reusability studies, Int. J. Biol. Macromol. 124 (2019) 854–862. https://doi.org/10.1016/j.ijbiomac.2018.11.197.

[7]   J. Fu, Z. Chen, M. Wang, S. Liu, J. Zhang, J. Zhang, R. Han, Q. Xu, Adsorption of methylene blue by a high-efficiency adsorbent (polydopamine microspheres): Kinetics, isotherm, thermodynamics and mechanism analysis, Chem. Eng. J. 259 (2015) 53–61. https://doi.org/10.1016/j.cej.2014.07.101.

[8]   T. Handayani, Emriadi, Deswati, P. Ramadhani, R. Zein, Modelling studies of methylene blue dye removal using activated corn husk waste: Isotherm, kinetic and thermodynamic evaluation, South African J. Chem. Eng. 47 (2024) 15–27. https://doi.org/10.1016/j.sajce.2023.10.003.

[9]   A. Öztürk, E. Malkoc, Adsorptive potential of cationic Basic Yellow 2 (BY2) dye onto natural untreated clay (NUC) from aqueous phase: Mass transfer analysis, kinetic and equilibrium profile, Appl. Surf. Sci. 299 (2014) 105–115.

https://doi.org/10.1016/j.apsusc.2014.01.193.

[10] J. Zhang, D. Cai, G. Zhang, C. Cai, C. Zhang, G. Qiu, K. Zheng, Z. Wu, Adsorption of methylene blue from aqueous solution onto multiporous palygorskite modified by ion beam bombardment: Effect of contact time, temperature, pH and ionic strength, Appl. Clay Sci. 83–84 (2013) 137–143. https://doi.org/10.1016/j.clay.2013.08.033.

[11] T.A. Aragaw, A.N. Alene, A comparative study of acidic, basic, and reactive dyes adsorption from aqueous solution onto kaolin adsorbent: Effect of operating parameters, isotherms, kinetics, and thermodynamics, Emerg. Contam. 8 (2022) 59–74. https://doi.org/10.1016/j.emcon.2022.01.002.

[12] R. Nodehi, H. Shayesteh, A.R. Kelishami, Enhanced adsorption of congo red using cationic surfactant functionalized zeolite particles, Microchem. J. 153 (2020) 104281. https://doi.org/10.1016/j.microc.2019.104281.

[13] N. Yasir, A.S. Khan, M.F. Hassan, T.H. Ibrahim, M.I. Khamis, P. Nancarrow, Ionic Liquid Agar–Alginate Beads as a Sustainable Phenol Adsorbent, Polymers (Basel). 14 (2022) 1–22. https://doi.org/10.3390/polym14050984.

[14] X. Hao, H. Liu, G. Zhang, H. Zou, Y. Zhang, M. Zhou, Y. Gu, Applied Clay Science Magnetic fi eld assisted adsorption of methyl blue onto organo-bentonite, Appl. Clay Sci. 55 (2012) 177–180. https://doi.org/10.1016/j.clay.2011.11.019.

[15] A. Mohammadi, H. Abdolvand, A.P. Isfahani, Alginate beads impregnated with sulfonate containing calix[4]arene-intercalated layered double hydroxides: In situ preparation, characterization and methylene blue adsorption studies, Int. J. Biol. Macromol. 146 (2020) 89–98. https://doi.org/10.1016/j.ijbiomac.2019.12.229.

[16] R.S. Hebbar, A.M. Isloor, B. Prabhu, Inamuddin, A.M. Asiri, A.F. Ismail, Removal of metal ions and humic acids through polyetherimide membrane with grafted bentonite clay, Sci. Rep. 8 (2018). https://doi.org/10.1038/s41598-018-22837-1.

[17] F.Y. Zhao, Y.L. Li, L.H. Li, Preparation and characterization of magnetite nanoparticles, Appl. Mech. Mater. 618 (2014) 24–27. https://doi.org/10.4028/www.scientific.net/AMM.618.24.

[18] A. Benhouria, H. Zaghouane-Boudiaf, R. Bourzami, F. Djerboua, B.H. Hameed, M. Boutahala, Cross-linked chitosan-epichlorohydrin/bentonite composite for reactive orange 16 dye removal: Experimental study and molecular dynamic simulation, Int. J. Biol. Macromol. 242 (2023) 124786. https://doi.org/10.1016/j.ijbiomac.2023.124786.

[19] N. Belhouchat, H. Zaghouane-boudiaf, C. Viseras, Applied Clay Science Removal of anionic and cationic dyes from aqueous solution with activated organo-bentonite /

sodium alginate encapsulated beads, Appl. Clay Sci. (2016). https://doi.org/10.1016/j.clay.2016.08.031.

[20] A. Sari, M. Tuzen, Biosorption of cadmium(II) from aqueous solution by red algae (Ceramium virgatum): Equilibrium, kinetic and thermodynamic studies, J. Hazard. Mater. 157 (2008) 448–454. https://doi.org/10.1016/j.jhazmat.2008.01.008.

[21] A.A. Abd, S.Z. Naji, A.S. Hashim, M.R. Othman, Carbon dioxide removal through physical adsorption using carbonaceous and non-carbonaceous adsorbents: A review, J. Environ. Chem. Eng. 8 (2020) 104142. https://doi.org/10.1016/j.jece.2020.104142.

[22] A.S. Sartape, A.M. Mandhare, V. V. Jadhav, P.D. Raut, M.A. Anuse, S.S. Kolekar, Removal of malachite green dye from aqueous solution with adsorption technique using Limonia acidissima (wood apple) shell as low cost adsorbent, Arab. J. Chem. 10 (2017) S3229–S3238. https://doi.org/10.1016/j.arabjc.2013.12.019.

[23] I. Diffusion-adsorption, P. Describir, 1665-2738-Rmiq-15-01-00161, (1998).

[24] A.C.S. Alcântara, P. Aranda, M. Darder, E. Ruiz-Hitzky, Bionanocomposites based on alginate-zein/layered double hydroxide materials as drug delivery systems, J. Mater. Chem. 20 (2010) 9495–9504. https://doi.org/10.1039/c0jm01211d.

[25] Z. Shao, Shuangbao, S. Wu, Y. Gao, X. Liu, Y. Dai, Two-step pyrolytic preparation of biochar for the adsorption study of tetracycline in water, Environ. Res. 242 (2024). https://doi.org/10.1016/j.envres.2023.117566.

[26] X. Hao, H. Liu, G. Zhang, H. Zou, Y. Zhang, M. Zhou, Y. Gu, assisted adsorption of methyl blue onto organo-bentonite, Appl. Clay Sci 55 (2012) 177–180, https://doi.org/10.1016/j.clay.2011.11.019.

[27] H. Yan, H. Li, H. Yang, A. Li, R. Cheng, Removal of various cationic dyes from aqueous solutions using a kind of fully biodegradable magnetic composite microsphere, Chem. Eng. J. 223 (2013) 402–411, https://doi.org/10.1016/j. cej.2013.02.113.

[28] N. Djebri, M. Boutahala, N.E. Chelali, N. Boukhalfa, L. Zeroual, Enhanced removal of cationic dye by calcium alginate/organobentonite beads: modeling, kinetics, equilibriums, thermodynamic and reusability studies, Int. J. Biol. Macromol. 92 (2016) 1277–1287, https://doi.org/10.1016/j. ijbiomac.2016.08.013.

[29] K. Jung, B.H. Choi, M. Hwang, T. Jeong, K. Ahn, Fabrication of granular activated carbons derived from spent coffee grounds by entrapment in calcium alginate beads for adsorption of acid orange 7 and methylene blue, Bioresour. Technol. (2016), https://doi.org/10.1016/j.biortech.2016.07.098.

[30] X. Zou, H. Zhang, T. Chen, H. Li, C. Meng, Y. Xia, J. Guo, Preparation and characterization of polyacrylamide / sodium alginate microspheres and its adsorption of MB dye, Colloids Surf. A Physicochem. Eng. Asp. 567 (2019) 184–192, https://doi.org/10.1016/j.colsurfa.2018.12.019.

[31] T.P. Krishna Murthy, B.S. Gowrishankar, R.H. Krishna, M.N. Chandraprabha, B. B. Mathew, Magnetic modification of coffee husk hydrochar for adsorptive removal of methylene blue: isotherms, kinetics and thermodynamic studies, Environ. Chem. Ecotoxicol. 2 (2020) 205–212, https://doi.org/10.1016/j. enceco.2020.10.002.

[32] H. Rezaei, M. Haghshenasfard, A. Moheb, Optimization of dye adsorption using Fe3O4 nanoparticles encapsulated with alginate beads by Taguchi method, Adsorpt. Sci. Technol. 35 (2017) 55–71, https://doi.org/10.1177/ 0263617416667508.

GENERAL CONCLUSION

General conclusion

The aim of this thesis was to create innovative biomaterials that effectively and efficiently remove organic contaminants from wastewater. The focus is on synthesizing magnetic bentonite, magnetic bentonite beads, organophilic magnetic bentonite, and organophilic magnetic bentonite beads designed for the elimination of a cationic dye (Methylene Blue), while also formulating a synthesis protocol for various composite materials.

In accordance with the principles of green chemistry and sustainable development, the bead matrix is composed of the natural polymer alginate, combined with magnetic bentonite nanoparticles and magnetic organophilic bentonite particles. Alginate is a polysaccharide derived from brown algae, while bentonite originates from natural deposits formed through the chemical weathering of volcanic ash. Primarily composed of montmorillonite clay minerals, bentonite is abundant in various natural deposits. The choice of these renewable and low-cost resources enables the development of a product with a positive environmental impact, contributing to pollution reduction.

Magnetic bentonite and organophilic magnetic bentonite beads are widely used for the adsorption of organic and inorganic pollutants. The magnetization of bentonite facilitates its recovery through magnetic separation, while the organophilic modification enhances its affinity for organic contaminants, thereby improving adsorption efficiency. Encapsulating these materials helps overcome challenges related to their dispersion in wastewater, ensuring better recovery and minimizing secondary waste generation.

The composite beads underwent extensive characterization to assess their physical and structural properties. The wet beads were found to be uniformly spherical, with low polydispersity and an average diameter of approximately 3 mm. This uniformity is crucial for ensuring reliable adsorption performance. Upon drying, the beads shrink, a factor that must be considered for practical applications.

The adsorption properties of the composite beads were evaluated by constructing adsorption isotherms for methylene blue, a cationic dye used as a model organic pollutant. By comparing these isotherms with those obtained for non-encapsulated bioadsorbents, potential adsorption mechanisms were proposed. The cationic dye exhibited higher adsorption on the composite

beads due to its interaction not only with the bioadsorbents but also through ionic exchange with counter-ions from the carboxylate sites in the alginate-based beads. This mechanism was further validated by examining the influence of pH on the adsorption process. At acidic pH levels, ionic exchange became less significant due to the protonation of carboxylate sites, emphasizing the role of pH in adsorption. Overall, the Langmuir model provided a suitable fit for the experimental data.

We also examined the adsorption kinetics of methylene blue on the four types of adsorbents at different initial dye concentrations. The equilibrium time varied depending on the adsorbent type. Non-encapsulated adsorbents exhibited rapid dye adsorption, reaching equilibrium in approximately 1 hour, whereas the composite beads required around 8 hours. In all cases, the adsorption kinetics were primarily described by a pseudo-second-order model.

The results obtained on the adsorption of organic pollutants using our alginate-based bioadsorbent beads are highly promising. We have developed innovative materials with a high adsorption capacity for efficient pollutant removal, while also enabling easy magnetic separation and regeneration at the end of the process. This dual functionality helps reduce both adsorption costs and waste production.

Moreover, employing biopolymers derived from renewable resources and biomass materials is expected to significantly lower production costs, enhancing the attractiveness of this process. By adopting a biobased adsorption approach, we can address various environmental challenges while ensuring:

- The absence of organic solvents, which contrasts with liquid-liquid extraction methods.
- The avoidance of toxic or hazardous reagents, unlike methods involving precipitation or oxidation. These benefits establish our biobeads as a sustainable solution for pollutant removal across different applications.
- Minimal secondary waste generation: The only waste produced consists of the pollutants themselves, which are concentrated within the biobeads, making transportation and recovery through desorption straightforward and enabling bead regeneration.
- Safe handling: Active species (nanomaterials) are encapsulated in a non-toxic biomass-derived matrix, ensuring safe manipulation and the utilization of natural resources.

Furthermore, it is vital to ensure that any modifications to the bead formulation align with eco-design principles followed during the materials' development. For a successful pollution treatment system, regenerating used materials is essential. Developing an efficient and non-destructive regeneration process to desorb or eliminate pollutants will enable the reuse of the same beads across multiple cycles. Our studies indicate that acidification can assist in desorbing pollutants associated with carboxylate functions. However, some pollutants remain strongly bound to the biomaterials' surface, suggesting that the adsorption mechanism may not be pH-sensitive in those cases. Therefore, simple acidification may not suffice for the complete recycling of the beads.

As part of this research, a combined experimental and theoretical approach was employed to gain deeper insight into the adsorption mechanisms of MBent-A beads. DFT calculations, along with FMO, RDG, and QTAIM analyses, revealed that Van der Waals forces and hydrogen bonding play a dominant role in the interaction between methylene blue and the bead surfaces. These non-covalent interactions ensure stable and efficient adsorption, thereby enhancing the material's performance. The integration of theoretical and experimental findings helps optimize adsorbent design and paves the way for the development of more efficient materials for wastewater treatment.

Additional studies on the treatment of natural water containing various micropollutants or pollutants could be considered in a continuous system to optimize results and advance toward industrial-scale processes. Expanding the adsorption capacity of the beads to include other types of pollutants, such as antibiotics and endocrine disruptors, would be relevant to assess the applicability of this adsorbent to a broader range of contaminants.

ABSTRACT

Résumé: L'objectif de cette étude est d'analyser l'élimination du bleu de méthylène par adsorption en mode discontinu, en utilisant des adsorbants magnétiques à base de bentonite et leur encapsulation dans de l'alginate. Ces matériaux ont fait l'objet de plusieurs caractérisations, notamment MEB/EDX, FTIR, DRX et pHpzc. Nous avons également examiné l'influence de divers paramètres sur le processus d'adsorption, tels que le pH, la masse de l'adsorbant et la température. L'étude inclut aussi l'analyse des isothermes et de la cinétique d'adsorption, qui ont été traitées à l'aide de modèles mathématiques. Les résultats indiquent que la cinétique d'adsorption suit un modèle de pseudo-second ordre, tandis que les isothermes sont bien ajustées par le modèle de Langmuir, suggérant une adsorption en monocouche. De plus, les billes démontrent une bonne durabilité, avec une efficacité d'élimination dépassant 90 % après cinq cycles de régénération. Des investigations théoriques approfondies utilisant la DFT, les FMO, le RDG et l'analyse QTAIM ont identifié les forces de van der Waals et les liaisons hydrogène comme les principales interactions régissant l'adsorption. En conclusion, les matériaux développés, en particulier les composites, se révèlent être des adsorbants très efficaces pour éliminer divers polluants et sont respectueux de l'environnement.

Mots clés : Adsorption, Bentonite, adsorbant magnétique, Bleu de Méthylène, Modélisation moléculaire.

Abstract: This study aims to analyze the removal of methylene blue via batch adsorption using magnetic bentonite-based adsorbents and their encapsulation in alginate. These materials underwent various characterizations, including SEM/EDS, IRTIF, XRD, and pHpzc analysis. The influence of different parameters on the adsorption process, such as pH, adsorbent dosage, and temperature, was also examined. The study includes an analysis of adsorption isotherms and kinetics, modeled using mathematical approaches. The results indicate that adsorption kinetics follow a pseudo-second-order model, while the isotherms fit well with the Langmuir model, suggesting monolayer adsorption. Additionally, the beads exhibit good durability, maintaining a removal efficiency exceeding 90 % after five regeneration cycles. In-depth theoretical investigations using DFT, FMO, RDG, and QTAIM analyses identified van der Waals forces and hydrogen bonding as the primary interactions governing adsorption. In conclusion, the developed materials, particularly the composites, prove to be highly effective and environmentally friendly adsorbents for the removal of various pollutants.

Keywords: Adsorption, Bentonite, Magnetic adsorbent, Methylene Blue, Molecular modeling.

الملخص: تهدف هذه الدراسة إلى تحليل إزالة أزرق الميثيلين عن طريق الامتزاز في نظام دفعي، باستخدام مواد ممتزة مغناطيسية قائمة على البنتونيت وتغليفها في الألجينات. خضعت هذه المواد لعدة تقنيات توصيف، بما في ذلك المجهر الإلكتروني الماسح مع التحليل الطيفي بالأشعة السينية المشتتة للطاقة (SEM/EDS) ، مطيافية الأشعة تحت الحمراء (IRTIF)، حيود الأشعة السينية (XRD) ، وتحديد نقطة الشحن الصفري (pHpzc). كما تم دراسة عدة عوامل على عملية الامتزاز، مثل درجة الحموضة، وكمية المادة الممتزة، ودرجة الحرارة. بالإضافة إلى ذلك، تم تحليل المتساويات الامتزازية والحركية باستخدام نماذج رياضية. أظهرت النتائج أن حركية الامتزاز تتبع نموذج الرتبة الثانية الكاذبة، في حين أن المتساويات الامتزازية تتناسب جيدًا مع نموذج لانغموير، مما يشير إلى امتزاز أحادي الطبقة. علاوة على ذلك، أظهرت الكريات استدامة جيدة، مع كفاءة إزالة تتجاوز 90 ٪ بعد خمسة دورات من التجديد. حددت التحقيقات النظرية المتعمقة باستخدام DFT و FMO و RDG وتحليل QTAIM أن قوى فان دير فالس وروابط الهيدروجين هي التفاعلات الأساسية التي تحكم عملية الامتزاز. في الختام، أثبتت المواد المطورة، وخاصة المركبة منها، أنها مواد ممتزة فعالة وصديقة للبيئة لإزالة مختلف الملوثات.

الكلمات المفتاحية: الامتزاز، البنتونيت، المادة الممتزة المغناطيسية، أزرق الميثيلين، النمذجة الجزيئية.